Università degli Studi di Firenze
Dottorato di Ricerca in Scienze Chimiche

Electrodeposition of thin films for energy applications

settore disciplinare: CHIM/03
Ciclo XXIII

Autore
Francesco Carlà

Tutore
Dr. Massimo Innocenti

Cotutore
Dr. Francesco Vizza

Coordinatore del Dottorato
Prof. Andrea Goti

Contents

List of acronyms and abbreviations

1-DDT 1-Dodecanethiol

1,3pn 1,3-diaminopropane

3-MPA 3-Mercaptopropionic Acid

AFM Atomic Force Microscopy

ALE Atomic Layer Epitaxy

CTR Crystal Truncation Rod

DAFC Direct Alcohol Fuel Cell

DEFC Direct Ethanol Fuel Cell

DT Decanethiol

ECALE Electrochemical Atomic Layer Epitaxy

EC-STM Electrochemical Scanning Tunneling Microscopy

FWHM Full Width Halfh Maximum

HER Hydrogen Evolution Reaction

LFM Lateral Force Microscopy

OPD Over Potential Deposition

ORR Oxygen Reduction Reaction

OT Octanethiol

PSPD Photon Sensitive Photodetector

SAM Self Assembled Monolayer

SCE Saturated Calomel Electrode

SHE Standard Hydrogen Electrode

SPM Scanning Probe Microscopy

STM Scanning Tunneling Microscopy

SXRD Surface X-ray Diffraction

TMACl Tetramethylammonium chloride

UHV Ultra High Vacuum

UPD Under Potenzial Deposition

XPS X-ray Photoelectron Spectroscopy

XRD X-ray Diffraction

XRR X-ray Reflectivity

Introduction

Several electrochemical methods for the synthesis of thin films of semiconductors, metal-oxides and a variety of layered metals and compounds have been extensively studied over the last 20 years. There are several advantages connected to electrodeposition. First of all, it is generally performed at room temperature, which means a reduced possibility of interdiffusion. Then, electrodeposition allows the very precise control of the amount of material deposited through, for example, Faraday's law or, as will be shown in the following, through the use of self-limiting phenomena such as underpotential deposition. Moreover, unlike high temperature methods, electrodeposition is not expensive and produces small amount of wastes. Finally, it has a good selectivity. The drawbacks are the necessity of conductive substrates and the use of condensed media that increases the presence of impurities. The crucial point in material electrodeposition is to control the dimensions of the electrodeposited structures. There are many applications for which miniaturization is necessary not only for computer but also in the electronic and optoelectronic industries, and more generally, for the realization of new functional and smart materials. The great interest in nanometer-scale materials stems from the fact that their optical, electrical, magnetic or mechanical properties are often very different from the same materials in the bulk phase, and, more important, they can be tuned by changing the physical dimensions of the material. Of course, compounds electrodeposition also requires composition control, that is the right stoichiometric ratio. Combining dimensional and composition control allows the attainment of compound thin films. In this thesis the work was developed on two principal research lines directed to:

- growth of thin films of compound semiconductors (CdS on Silver) for photovoltaic applications.
- electrodeposition of metal layers for practical use in electrocatalysis (Pd thin films for Ethanol oxidation).

The most important aspect to be considered in semiconductor compound electrodeposition is the structure of the semiconductive layer which must be, as possible, crystalline and, still better, epitaxial. In fact, small amounts of stress can shift the luminescent properties, and small number of defects can provide recombination centers that lower the device's efficiency. In this perspective, the Electrochemical Atomic Layer Epitaxy (ECALE) technique is a valid approach for the attainment of II-VI compound semiconductors on metallic substrates. The method is based on the alternate underpotential deposition of atomic layers of the elements that form the compound, in a cycle that can be repeated as many times as desired, and the thickness of the deposit is determined by the number of deposition cycles. The big advantage of the method is that the individual steps of each cycle can be examined and optimized independently. That means that the conditions for deposition can be adjusted as concerns potentials, pH, reactants, and so on. These conditions are strictly dependent on the compound that is to be obtained, and on the substrate used: we always used single crystals to increase the probability for the epitaxial growth. Effects of substrates structure on the growth of semiconductor thin films of Cadmium Sulfide were studied by in-situ STM investigating the lattice parameters of the S adlayer on different silver single crystal facet (see section 3.1) and by structure analysis of the thin film with Surface X-ray diffraction experiments (see section 3.2). With the aim of further reducing the size of the electrodeposited material, a method to perform the electrodeposition of CdS in a thiol Self Assembled Monolayer template was studied. Basically, electrodeposition was performed in the nanometer sized holes left in a binary SAM of thiols having different lengths after desorption of the shorter chain thiol. This method has been checked by depositing CdS, whose experimental growth conditions are simple and reproducible and make it a good *electrodeposition probe*, with the purpose of using it in the future for the electrodeposition of islands of metals able to exert sinergic electrocalalytic effects. Electrodeposition was used also in the synthesis of catalysts for the next generation fuel cell. Fuel Cell electrocatalysts participate in electrochemical reaction at electrode surfaces assisting the electron transfer between electrode and reactants and/or facilitating an intermediate chemical transformation in a half-reaction. In Fuel Cell the electrode surface itself can be catalytic. Alternatively, other electrocatalytic material, like nanoparticles, are used. Several aspects must be considered in the synthesis of the electrocatalysts: electrochemical surface area (as highest as possible), catalysts stability and poisoning during usage, catalytic effect and cost. Electrodeposited thin films are a possible alternative to the use of

nanoparticles, which may be unstable and not indicated for certain use such electrolysis or application in highly stirred solutions. The topic of chapter 4 is the synthesis and the characterization of palladium thin films and clusters on nickel substrate. Palladium has recently aroused notable interest in electrocatalysis as it is less expensive than platinum and has the capacity to promote oxidation of several alcohols. Pd-Ni based electrocatalysts activity is well known for reactions such as ethanol oxidation in akaline media. The possibility of manufacturing electroactive material by electrodeposition and template electrodeposition allows the attainment of stable catalysts with a reproducible synthetic method. Pd thin films growth has been investigated on nickel flat electrodes and on high surface area nickel-foam electrode with the aim of studying the origin of the catalytic effect. AFM investigation on Pd thin film morphology was conducted in order to understand the effects of surface roughness on catalytic activity of the electrode material. The use of thiol Self Assembled Monolayers for the growth of rough Pd films on polycristalline Ni electrode was also investigated. For this purpose a novel method for thiol electrochemical assisted deposition on Ni surface was studied.

Chapter 1

Surface electrochemistry

1.1 Electrodeposition

Electrodeposition is a technique that is well-suited to the preparation of nanostructures. In electrodeposition processes the amount of deposited material is related to the charge transferred during the process and can be controlled simply through Faraday's law. Nevertheless a better control of the growth can be obtained exploiting chemical interactions between surface and adlayers which leads to the phenomen known as Under Potential Deposition. Different strategies have to be employed to control the electrochemical growth, depending on the substrate chemical/electrochemical reactivity and the kind of deposited material. In this section an introduction to overpotential and underpotential is reported, moreover general features of electrochemical epitaxy will be treated.

1.1.1 Under Potential Deposition

Within a pure metal/metal-ion electrolyte system of a specic metal the onset of deposition (or dissolution) is well defined by the respective Nernst equilibrium potential. However, for metal deposition on a foreign metal substrate, we have to consider the interaction of the substrate atoms S with the deposited adlayer Me_{ad} . When the interaction of S-Me_{ad} is stronger than the Me_{ad}-Me_{ad} interaction the first adlayer (in some cases also a double layer) is already deposited at potentials preceding the Nernst potential. This effect can be used as a single monolayer deposition technique and is called Under Potenzial Deposition (UPD) [1]. UPD provides a unique method of a controlled, often exactly one monolayer, metal deposition on a foreign substrate

in a potential window before the onset of bulk deposition. Such phenomen allows for the precise and reproducible control of the surface coverage and for the study of coverage-dependent properties including the structure of the metallic adlayer and its electronic properties.
In the case of phase formation on foreign substrates the overall reaction between the adlayer Me_{ad} and the element in solution (Me_{sol}) is given by:

$$\mathrm{Me}_{ad} \Leftrightarrow \mathrm{Me}^{z+}_{sol} + ze^{-} \tag{1.1}$$

The thermodynamic equilibrium is given by the Nernst equation:

$$E_{\mathrm{Me}_{ad}/\mathrm{Me}^{z+}_{sol}} = E^{o}_{\mathrm{Me}_{ad}/\mathrm{Me}^{z+}_{sol}} + \frac{RT}{zF} \ln \frac{a_{\mathrm{Me}^{z+}_{sol}}}{a_{\mathrm{Me}_{ad}}} \tag{1.2}$$

Then, the potential of stability of 3D bulk phases is given by $E = E_{\mathrm{Me}_{ad}/\mathrm{Me}^{z+}_{sol}}$. However, for small 3D cluster phases, the potential of stability can be more negative, $E < E_{\mathrm{Me}_{ad}/\mathrm{Me}^{z+}_{sol}}$. As a matter of fact, possible deviations of the atomic arrangement of the initial small clusters from that of a 3D bulk crystal can determine additional energy terms that increase the total Gibbs energy change of the system. On the contrary, for some 2D phases the potential of stability can even be more positive, $E > E_{\mathrm{Me}_{ad}/\mathrm{Me}^{z+}_{sol}}$. This latter case corresponds to the underpotential deposition that occurs in the presence of specific interactions between the depositing metal and the substrate. By convention the potential difference $E - E_{\mathrm{Me}_{ad}/\mathrm{Me}^{z+}_{sol}}$ is defined as ΔE UPD or Over Potential Deposition (OPD). Then, the Nernst equilibrium potential, $E_{Neq} = E = E_{\mathrm{Me}_{ad}/\mathrm{Me}^{z+}_{sol}}$, represents the limit of the stability range of both 2D and 3D Me phases. That means that at E_{Neq} 2D and 3D Me phases coexist and, as a consequence, the underpotential deposition and overpotential deposition of Me on S are connected with the formation of 2D and 3D Me phases, respectively. The process of Me OPD on S becomes identical with that of Me OPD on Me if the deposited Me film on S exceeds a certain thickness (usually from one to twenty monolayers) and behaves like a 3D Me bulk phase. Of course, the kinetics of the deposition process should also be taken into account. The most important parameters determining the mechanism of UPD and OPD of Me on a foreign substrate are the Me_{ad}S binding energy ($\Psi_{\mathrm{Me}_{ad}-S}$) and the crystallographic misfit between S and a 3D Me deposit. Limiting ourselves to the thermodynamic aspects (that is,

considering the deposition process at nearly equilibrium conditions, so as to neglect kinetic effects), two different growth modes can be distinguished:

1. $\Psi_{\mathrm{Me}_{ad}-S} < \Psi_{\mathrm{Me}_{ad}-\mathrm{Me}_{a}d}$
   The surface concentration of Me_{ad} at $E_{\mathrm{Me}_{ad}/\mathrm{Me}^{z+}_{sol}}$ is small, and OPD of a 3D Me bulk phase takes place on an unmodified substrate surface according to the Volmer-Weber or 3D islands growth mode independent of crystallographic Me-S misfit.

2. $\Psi_{\mathrm{Me}_{ad}-S} > \Psi_{\mathrm{Me}_{ad}-\mathrm{Me}_{a}d}$
   Then, 2D phases can be formed in the UPD range and the surface concentration of Me_{ad} at $E_{\mathrm{Me}_{ad}/\mathrm{Me}^{z+}_{sol}}$ can reach one or more Me_{ad} monolayers depending on $\Psi_{\mathrm{Me}_{ad}-S}$. Two different subcases can be distinguished:

   - if the crystallographic Me-S misfit is negligibly small, 2D Me UPD overlayers and 3D Me crystallites are epitaxially oriented following the Frank-van der Merwe mechanism.
   - in the presence of significant crystallographic Me-S misfit, the growth mechanism is the Stranski-Krastanov mode with unstrained 3D Me bulk phase on top of a strained 2D Me_{ad} phase.

1.1.2 ECALE electrodeposition

Thus, UPD is the phenomenon by which an element is deposited at a potential prior to (under) that needed to deposit the element on itself. Deposition is facilitated by the free energy of formation of a surface compound. That is, a solution containing a precursor for a first element is reacted at a controlled potential with a previously deposited atomic layer of a second element, until the surface is covered, forming a compound monolayer. In electrochemical ALE (EC-ALE), the solution is then exchanged for one containing a precursor to the second element, and from which an atomic layer of it is deposited at a controlled potential, completing the deposition of one monolayer of the compound. Thin films are grown by repeating this cycle as many times as desired. Schematically the ECALE cycles requires four steps:

- UPD of the first element
- Rinsing
- UPD of the second element

- Rinsing

In terms of speed and simplicity, ECALE is not competitive with co-deposition, however, the degrees of freedom available in co-deposition are severely limited compared to ECALE. ECALE provides much increased control over deposit structure, morphology, and composition, by having separately optimized solutions and potentials for each element. In addition, as ECALE is based on layer by layer growth, epitaxy can be facilitated, and the thickness of the deposit is determined by the number of deposition cycles. The atomic layer control is a necessary prerequisite in the formation of nanostructured materials. Control of growth at the nanometer scale is a major frontier of Material Science. By constructing superlattices, nanowires and nanoclusters, by forming nanocrystalline materials, the electronic structure (bandgap) of a semiconductor can be engineered. The wavelengths of light emitted or absorbed by a compound can be adjusted over a broad range. By direct analogy with the quantum mechanical model of a particle in a box, it is known that the smaller the box containing an electron, the further apart its energy levels are driven. This translates directly for some semiconductor structures, the smaller the thickness of the layers, or the dimensions of a particle, the larger the resulting bandgap.

1.1.3 Over potential and electrode kinetics

UPD is a process at equilibrium, in many cases electrochemical reactions occur in non-equilibrium conditions. UPD is a very special case, infact in almost all electrochemical reactions an activation barrier E_a has to be passed. This means that the value of the applied external potential must exceed that of the equilibrium potential to force the electrochemical reaction and make the charge transfer happen. The difference η between the applied potential and the equilibrium potential is called *overpotential*. For large values of overpotentials ($\eta \geq 100mV$) the current density i increases exponentially with the overpotential η according to equations (respectively valid for cathodic and anodic reactions):

$$i^{+}(\eta) = +i_0 \cdot \exp \frac{\alpha z F \eta}{RT} \tag{1.3}$$

$$i^{-}(\eta) = -i_0 \cdot \exp \frac{(1-\alpha) z F \eta}{RT} \tag{1.4}$$

where i_0 is the exchange current density, α the transfer coefficient, F the Faraday constant, R the gas constant and T the absolute temperature. Summing the forward current and the backward current we get the total current

passing through the interface. This leads to the expression also known as the Butler-Volmer equation:

$$i = i^+ + i^- = j_0 \cdot [\exp + \frac{\alpha z F \eta}{RT} - exp \frac{(1-\alpha) z F \eta}{RT}] \tag{1.5}$$

The Butler-Volmer equation does not completely describe kinetic processes at the electrochemical interface, but gives a first quantitative approximation. Important additional effects are diffusion of reaction partners or chemical reactions involved. If the electron transfer through the electrode surface is not the rate limiting step, the concept of overpotential gets more complicated. In the current-overpotential curve this is reflected by a deviation from the described Butler-Volmer model. If the electrochemical reaction is limited by diffusion, at higher currents the current-potential curve will deviate from the exponential form and saturate, giving smaller current values.

1.1.4 Pourbaix diagram

Surface processes like absorption, desorption or redox reactions are very sensible to surface composition. While noble metals have great stability in a wide range of potentials, non-noble metals at certain value of pH and potential can form surface oxide or be dissolved in solution. Therefore to control electrodeposition and electrodesorption processes on non-noble metals is necessary to know which is the potential range where corrosion and passivation reactions take place. One way to predict chemical reactions at the surface is to consider the thermodynamical equilibrium relations for the system. Chemical and electrochemical equilibria can be summarised in a *Pourbaix diagram*, which is a potential-pH diagram. The diagram is a map of the multidimensional thermodynamc space and predicts areas of immunity (no corrosion), passivity (a solid reaction product is formed) and corrosion (dissolution).

1.2 Chemically modified electrodes

Chemical modification of electrodes surface is a powerfull route to tuning electrode performance and provides a control on electrode-environment interactions. It has been particularly important to electroanalytical chemistry, improving electrocatalytic properties, energy conversion, corrosion protection, molecular electronics and much more. Chemical modification can be used within electrochemical processes in surface nanostructuring. Coupling of different synthetic strategies provides the opportunity of controlling surface structure, morphology and composition at the nanoscale. Use of organic monolayer coupled with electrodeposition allows to obtain surfaces with a unique range of properties, such as ultrahigh surface areas or bimetallic surface modified with nanoclusters. The most promising strategies in electrode nanostructuring are those employing Self Assembly phenomena in electrode modification. Self-assembly is a nowadays widely extended term that refers to the spontaneous formation of discrete nanometre-sized units, forming a secondary structure from simpler subunits or building blocks [2]. During the self-assembly process, the constituent subunits (atoms, molecules, biomolecules, simple biological structures, etc), combine in such a way that they form more complex structures with fewer degrees of freedom. While biological membranes, cellular structures and even viruses and cells can be regarded as highly sophisticated self-assembled systems [3], the simplest examples are certainly the so-called self-assembled monolayers (SAMs) [4]. These are, in a few words, arrangements of molecules (or atoms) in which intermolecular forces play a key role. In the case of SAMs on solid surfaces, they can be easily formed by spontaneous adsorption from liquid or gas phases. Examples of SAMs on solid surfaces are thiols, silanes and phosphonates [5, 6]. A specific covalent linker is used to guide the self-assembly process on each type of substrate. S or N atoms for clean metals and Si or P for hydroxilated surfaces and oxidized surfaces are some examples of usually employed linkers [5, 6]. Among SAMs, the most popular because of both their promising and current applications in several fields of nanotechnology are alkanethiol (and alkanedithiol) monolayers on metals and metallic nanoparticles (particularly Au and Ag and, to a lesser extent, Cu, Ni, and Pd) [2]. Since alkanethiol SAMs represent an easy path to link inorganic, organic and biological materials, they are essential in many of the so-called *bottom-up* methods proposed to build a wide variety of devices and materials [7, 8]. It is important to note that, in a similar way to protein formation, the bottom-up approach could involve different levels of construction [9–11]. The van der Waals forces between neighbouring molecules stabilize the struc-

ture. Therefore, the interchain van der Waals interactions become effective, which leads to formation of a close-packed *ordered* or *solid-like* state. SAMs are formed by atoms or molecules that constitute the basic units or building blocks of the system. In the case of thiols, and also of silanes and phosphonates, each molecule can be divided in three different parts: the head (linking group), the backbone (main chain), and the terminal specific (active) group. The active group confers the desired functional properties to the layer. A small change in the endgroup can be enough to change the physical and chemical properties of the layer [4, 12, 13]. Thus, -CH3 and -CF3 groups turn the SAM surface hydrophobic, metallophobic and highly anti-adherent, while -COOH, -NH2 or -OH groups yield hydrophilic surfaces with good metal ion and protein binding properties. Also, -SH-terminated thiols (termed dithiols) efficiently bind metallic ions and nanoparticles to the SAMs [2, 14]. Alkanethiol SAMs present applications in several fields of technology, ranging from electronics , to biosensors, bio-recognition devices and drug delivery [2, 3]. SAMs are also of relevance in fields such as lubrication [15], patterning of surfaces [16], corrosion protection [17–19], to name a few.

1.3 Electrocatalysis

An electrocatalyst is a catalyst that participates in electrochemical reaction. The term can be referred to specific forms of catalysts that work at electrode surfaces or to the electrode surface itself. Thus, as catalysts, electrocatalyst can be homogeneous (coordination complex or enzime) or heterogeneous (electrodic material). Several factors can be at the origin of the catalytic activity of a material. In heterogeneous catalysis the electrode material may assists in transferring electrons between the electrode and reactants and/or lowers the activation energy facilitating an intermediate chemical transformation. In this case the catalytic affects is related with the structural, electronic and chemical properties of the surface. Nevertheless the catalytic activity can be simply related to the extension of the surface area of the electrode. Thus, the origin of the catalytic effect is *real* if related with the electrode material or *apparent* if dependent on the surface area [20, 21]. The separation of electronic from geometrics factors and the understanding of the phenomena at the origin of electrocatalytic activity are fundamental for the implementation of catalytic materials and the devolepment of better and cheaper catalysts. Nowday research on electrocatalysis is mostly focused on the synthesis of new electrocatalytic materials for sustainable energy pro-

duction with fuel cell. Hydrogen is considered the most convenient fuel in most applications of fuel cell devices. Unfortunatly difficulties with its storage, distribution and production limitat its use. Other fuels, particularly those like alcohols, which are liquid at ambient temperature and pressure, are more convenient due to ease of handling and distribution.

Chapter 2

Experimental techniques

2.1 Scanning Probe Microscopies

The term Scanning Probe Microscopy (SPM) refers to a branch of microscopy that forms images of surfaces using a physical probe that scans the specimen. An SPM image of the surface is obtained by mechanically moving the probe in a raster scan of the specimen, line by line, and recording the probe-surface interaction as a function of position. The first SPM experiment presented was the STM developed by Gerd Binnig and Heinrich Rohrer in 1981 [22]. It was again the same research group at IBM Research Division in Zurich that was involved in the development of Atomic Force Microscopy (AFM) [23]. After that, several additional SPM techniques have been developed in the last 20 years. They all differ in the way the distance between tip and sample is detected or in the physical origin of the force causing deflection of a probing tip. SPM instruments are used for studying surface properties of materials from the atomic to the micron level. Probe microscopy is a rapidly developing area and its capability of mapping surface with 3-D resolution and measuring physical properties (such as surface conductivity, static charge distribution, localized friction, magnetic fields, and elastic modulus) at nanometer scale made it one of the most used techique in material science and surface analysis.

2.1.1 AFM

The forces involved in tip deflection can be qualitatively explained in term of Van der Waals interaction. A formula for the energy of the tip-sample system can be derived using the Lennard-Jones exponential function (see fig.

2.1). The interaction of a tip with sample has a very complex character, but

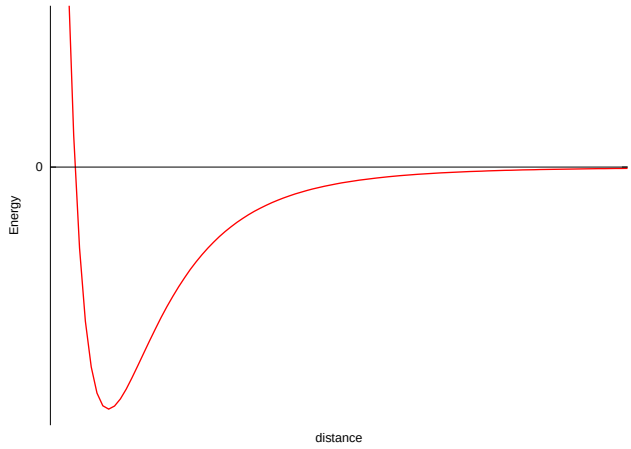

Figure 2.1: Lennard-Jones potential, qualitative form

the basic features are the same as for atoms interaction in vacuum: AFM tip is attracted by the sample at large distances and repelled at small distances. Forces between the tip and the sample surface cause the cantilever to bend, or deflect. A detector measures the cantilever deflection as the tip is scanned over the sample, or the sample is scanned under the tip. The measured cantilever deflections allow a computer to generate a map of the tip-surface interactive force. AFMs can be used to study insulators and semiconductors as well as electrical conductors, which is an advantage compared to the STM, which requires sufficient conductance of the sample. Several forces typically contribute to the deflection of an AFM cantilever. Most AFMs currently on the market detect the position of the cantilever with optical techniques. In the most common scheme, (Fig. 2.2) a laser beam bounces off the back of the cantilever onto a position-sensitive photodetector (PSPD). As the cantilever bends, the position of the laser beam on the detector shifts. A PSPD can measure displacements of light as small as 1 nm. And, because the ratio of the path length between the cantilever and the detector and the length of the cantilever itself produces an amplication of the movements on the detector site, the system can detect sub-nanometer vertical movement of the cantilever tip. Surface sensing in AFM is performed using special probes made of an elastic cantilever (100 to 200 μm long) with a sharp tip on the end (a couple of micrometers long and often less than 10nm in diameter). Depending on the distance the tip experience different kind of interactions

with the surface. Several modes for operating Atomic Force Microscopy exist and are usually classified using the tip-sample distance:

- Contact AFM
  In the static mode operation, the static tip deflection is used as a feedback signal.

- Non-contact AFM
  Cantilever oscillates at a frequency slightly above its resonance frequency. Resonance frequency change because of van der Waals and long range forces . A feedback loop system adjust the average tip-sample distance in order to mantain a constant oscillation amplitude.

- Tapping AFM
  The amplitude of oscillation is greater than in Non-contact mode and the tip is in intermittent contact with the sample surface. Like in Non-contact mode the amplitude oscillation is kept constant adjusting the cantilever height above the sample.

In this work the analysis of the surface morphology was carried out in contact mode with an in-air AFM. This choice was due mainly because the AFM can better cope with a rough surface morphology generated by electrodeposition process compared to STM. Although STM's give better resolution on the atomic scale, they also require clean and flat surfaces on the scale of the image. Further in contact mode the force between the tip and the sample has a component normal to the sample surface (F_z) and a lateral component (F_L) laying in the plane of the sample surface (figure 2.2). F_z component is originated by heigth variations of the surface sample. Lateral deflections of the cantilever instead arise from two sources: changes in surface friction and changes in slope. In the first case, the tip may experience greater friction as it traverses some areas, causing the cantilever to twist more strongly. In the second case, the cantilever may twist when it encounters a steep slope. Lateral Force Microscopy (LFM) studies can be very useful for imaging variations in surface friction that can arise from inhomogeneity in surface material, and also for obtaining edge-enhanced images of any surface. LFM is extremely suitable to identify surface compositional (chemical) differences where the materials have differing frictional characteristics and the topography is relatively flat.

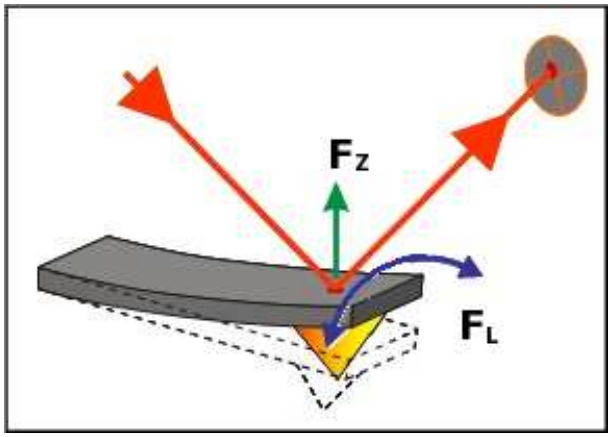

Figure 2.2: Contact-mode AFM, beam deflection and friction force

2.1.2 STM

STM provides real-space atomic-resolution images of the surface topography. The working principle of STM is based on the phenomenon of electrons tunneling trough a narrow potential barrier between an atomically sharp conductive tip and a conductive sample while a voltage between the sample and tip is applied. Depending on the distances between tip and sample and on the applied voltage, electrons might be able to cross the barrier between sample and tip. The tunneling current (I) is described by the formula:

$$I \propto U \exp^{-A\sqrt{\Phi}d} \tag{2.1}$$

Where U is the applied voltage between sample and tip, d their distance, A is a constant and Φ is the barrier height depending on the electronic structures of the tip and the sample. The barrier height can be determined from current-distance measurements. Exponential dacays in tunneling current allow to register images with high resolution along the z-direction and obtain atomically resolved images. Surface analysis are usually performed in constant current mode: once the tip is approached to the surface a constant voltage is applied, the resulting tunneling current is measured and kept constant adjusting the tip-surface distance while scanning the tip over the sample. Tip movements along the three axis are controlled by piezoelements on which the tip is mounted.

2.2 Surface X-ray Diffraction

Structural characterization of surfaces by X-ray diffraction needs sources with a high intensity, which makes it unpractical in laboratory based X-ray generators. Moreover, diffraction experiments for determining the structure of thin films requires X-ray beams of relatively high energy, which can be efficiently provided by third generation high energy synchrotrons. General introduction to X-ray diffraction theory can be found in most textbooks [24, 25], a brief introduction to Surface X-ray Diffraction (SXRD) is given in this section. More complete review on the theory and the experimental setup for determining local atomic arrangements at surfaces can be found elsewhere [26, 27].

2.2.1 X-ray Diffraction

Assuming a block shaped crystal with N_1, N_2 and N_3 unit cells along the three crystal axes defined by the vectors $\boldsymbol{a_1}$, $\boldsymbol{a_2}$, $\boldsymbol{a_3}$ the scattering amplitude of the crystal is given by:

$$\boldsymbol{A_q = A_0 \left(\frac{e^2}{mc^2 R_0} \right) F(q) \sum_{n_1=0}^{N_1-1} \sum_{n_2=0}^{N_2-1} \sum_{n_3=0}^{N_3-1} \exp\left(iq\cdot(n_1 a_1 + n_2 a_2 + n_3 a_3)\right)} \tag{2.2}$$

where $\boldsymbol{e}$ and $\boldsymbol{m}$ are the electron's charge and mass, $\boldsymbol{R_0}$ the distance to the observer, $\boldsymbol{A_0}$ the amplitude of the oncoming wave, $\boldsymbol{q}$ is the *momentum transfer* (vector difference between the incoming and the outgoing vector) and $\boldsymbol{F_q}$ the so called *structure factor*. Using the '$\boldsymbol{N}$-slit interference function', defined as:

$$\boldsymbol{S_N(x) = \sum_{n=0}^{N-1} exp(ixn) = \frac{1 - exp(ixn)}{1 - exp(ix)}} \tag{2.3}$$

Equation 2.2 can be written as:

$$\boldsymbol{A_q = A_0 \left(\frac{e^2}{mc^2 R_0} \right) F(q) S_{N1}(q \cdot a_1) S_{N2}(q \cdot a_2) S_{N3}(q \cdot a_3)} \tag{2.4}$$

In case of large crystals the $\boldsymbol{N}$-slit interference function $\boldsymbol{S_N qa}$ tends in the limit to a periodic array of $\boldsymbol{\delta}$ functions with a spacing of $\boldsymbol{2\pi/a}$. This means that diffracted intensity from a crystal rise to maximum only along well defined directions. Being the product of orthogonal periodic $\boldsymbol{\delta}$-function arrays, the conditions for constructive interference will be reached if three

conditions (Laue equations) are fullfilled simultaneously:

$$\begin{aligned} \boldsymbol{q \cdot a_1} &= \boldsymbol{2\pi h} \\ \boldsymbol{q \cdot a_2} &= \boldsymbol{2\pi k} \\ \boldsymbol{q \cdot a_3} &= \boldsymbol{2\pi l} \end{aligned} \tag{2.5}$$

where $\boldsymbol{h}$,$\boldsymbol{k}$ and $\boldsymbol{l}$ are the Miller indices. Thus diffracted intensity from a crystal will result zero except at discrete points. Equation for the intensity at such h,k,l point in function of the reciprocal lattice vector ($\boldsymbol{b_1}$, $\boldsymbol{b_2}$, $\boldsymbol{b_3}$) can be found by squaring the scattering amplitude given by equation 2.2:

$$\boldsymbol{I_{hkl}} = \left| \boldsymbol{E_e \frac{e^2}{mc^2 R_0} PF(hb_1 + kb_2 + lb_3) N_1 N_2 N_3} \right|^{\boldsymbol{2}} \tag{2.6}$$

where the reciprocal lattice vectors are defined as

$$\begin{aligned} \boldsymbol{b_1} &= \boldsymbol{2\pi \frac{a_2 \times a_3}{a_1 \cdot a_2 \times a_3}} \\ \boldsymbol{b_2} &= \boldsymbol{2\pi \frac{a_3 \times a_1}{a_1 \cdot a_2 \times a_3}} \\ \boldsymbol{b_3} &= \boldsymbol{2\pi \frac{a_1 \times a_2}{a_1 \cdot a_2 \times a_3}} \end{aligned} \tag{2.7}$$

2.2.2 X-ray Diffraction from surfaces

In SXRD experiment the x-ray beam is incident to the surface at glancing angles, in this geometry the beam penetration depth is reduced and the surface sensitivity increased. SXRD can be described as a special case of a three dimensional X-ray Diffraction (XRD) experiment. Surface contribution to the diffracted intesity can be calculated using equation 2.6, taking $\boldsymbol{a_3}$ to be along the surface normal the signal of the top monolayer is calculated setting $\boldsymbol{N_3 = 1}$. The diffraction is then independent of $\boldsymbol{q \cdot a_3}$ and in the 3D reciprocal space, instead of Bragg reflections, can be observed a 2D lattice of rods. Such rods are called Crystal Truncation Rods (CTRs) since they arise from a crystal being truncated. A more realistic model for surface diffraction is obtained considering the diffraction of a truncated 3D crystal. In this case the intensity distribution perpendicular to the surface is given by the sum of the bulk Bragg reflections and the surface crystal truncation rod. The intensity distribution along the rod for the 2D case and

the truncated crystal can be written as:

$$I_{2D} = \left| E_e \frac{e^2}{mc^2 R_0} F(q) N_1 N_2 \right|^2 \tag{2.8}$$

$$I_{CTR} = \left| E_e \frac{e^2}{mc^2 R_0} F(q) N_1 N_2 \right|^2 \frac{1}{2sin^2(q \cdot a_3/2)} \tag{2.9}$$

Since the intensity distribution along the rod depends on the structural parameters of the surface, surface relaxation and reconstruction phenomena can be studied by the CTRs analysis. Hence diffraction experiments on thin films allow to investigate not only the film crystallographyc structure and its relation with the substrate lattice but also the lattice strain at the film/substrate interface.

2.3 Experimental setups

2.3.1 Data acquisition in EC experiments

Data acquisition in elecrochemical experiments was performed by a National Instruments PCI-6052E DAQ board. Cell potential was regulated via analog I/O using an Amel Model 551 potentiostat and digital I/O were used to control solenoid valves of the solution distribution system (see 2.3.5). Data were collected via LabView Virtual Instruments (VI) written by the author for this purpose. A LabView VI allows to record cyclic voltammograms, single sweep voltammograms and, during the rest time between potential scans, to control continuosly the applied potential and record the current value. When the program is launched the VI creates a log file where current, potential, solution in cell and time are recorded. All electrochemical experiments were performed with the previously described set-up except the chronocoulometric measurements, for this purpose an μAutolab potentiostat/galvanostat system was used.

2.3.2 Scanning Probe Microscopy

SPM experiments were conducted on a Molecular Imaging Dimensions 3100 equipped with AFM M 1205 and STM A 1111 AFM/STM scanners.

AFM

The AFM images presented in this work were taken in contact mode in environmental conditions. Nanosensors PPP-LFMR tips were used for Lateral Force Microscopy measurements.

STM

The in situ STM experiments were carried out using an electrochemical cell in Kel-F that was specifically designed to be adapted to the Molecular Imaging STM (PicoSPM). Cell layout in shown in fig. 2.3; it has fairly uncommon features: a Ag/AgCl(KCl sat.) reference electrode, a stable connection through the lower surface of the crystal for the working electrode and a circular Pt counter electrode. STM tips were prepared from 0.25 mm diameter tungsten wire (Aldrich) by electrochemical etching in a 2M NaOH solution, or by cutting a PtIr (80:20) wire. To minimize faradaic current at the tip-electrolyte interface, the tips were covered with Apiezon wax. Topographic images are 512x512 pixels, obtained with constant-current mode

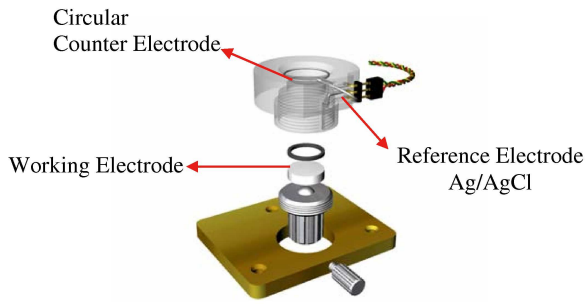

Figure 2.3: STM electrochemical cell

and without further filtration, unless otherwise indicated in the captions. Experimental conditions like tunneling current and bias voltage are given in the figure captions; positive bias voltages indicate that the tip is positive with respect to the sample.

2.3.3 XPS

The X-ray photoelectron spectroscopy (XPS) measurements reported in this work were performed using a non-monochromated Al-Ka X-ray source (1486.6 eV) and a VSW HAC 5000 hemispherical electron energy analyser. Photoelectron spectra were acquired in the constant-pass-energy mode at Epas = 44 eV, and the overall energy resolution was 1.2 eV measured as a full-width at half maximum (FWHM) of the Ag $3d_{5/2}$ line of a pure silver reference. Pressure during the experiment was kept below 2×10^{-9} Torr. Since the sample was conductive no neutralizer was used and the spectra energy scale was corrected using the C 1 s peak of organic atmospheric contaminants. The recorded spectra were fitted using XPSPeak 4.1 software employing GaussLorentz curves to fit the data after subtraction of a Shirley-type background.

2.3.4 Beamline set-up

Surface X-ray diffraction experiments can be realized only with high energy and high brilliance x-ray source. For this reason in this kind of experiments synchrotron radiation is commonly used. SXRD and XRR experiments were carried out at ID03 beamline in the European Synchrotron Radiation Facilities (ESRF) in Grenoble.

x-ray source

The ESRF is a third generation synchrotron light source with a 6 GeV electron storage ring. The ID03 beamline is illuminated by three undulators installed in a low-β section of the ESRF synchrotron ring. The ID03 optics hutch provides monochromatic and focused X-ray beams to the experimental hutches. The monochromator is an ESRF standard design based on the use of a monolithic channel cut Si(111) crystal cooled at liquid nitrogen temperature. Even if the monochromator energy range goes from a minimum of 3 keV up to a maximum of about 50 keV, the beamline design has been optimized for a 5-24 keV energy range. The use of the monolithic channel-cut Si (111), more stable by design, does not allow any focalisation. A Kirkpatrick-Baez mirror for harmonic energy photon rejection and a high resolution post-monochromator is placed at the entrance of experimental hutch.

ID03 diffractometer

ID03 experimental hutch is equipped with a computer controlled HUBER six-circle z-axis vertical diffractometer, suited for samples with a horizontal surface geometry. The two stepmotor of the tower stage, (ϕ and χ circle) were used for sample alignment and frozen afterwards. The incident angle of the beam was adjusted with the diffractometer tilt and then was fixed (value of 0.2° were used). The three motors used for the experiment were the ω motor rotating the sample in the plane about its surface normal and the two detector motors: δ (in-plane rotation) and γ (out-of-plane inclination). Samples were mounted on the diffractometer stage enclosed in a mylar bag filled with nitrogen to prevent surface damage by oxigen and ozone.

2.3.5 Electrochemical set-up

Electrochemical flow-cell

For the cyclic voltammetry experiments on flat electrodes (Silver single crystal, poliscrystalline Nickel and glassy carbon) flow cells made in Kel-f were used (figure 2.4). Counter electrode was a gold disc placed at the bottom end. The inlet and the outlet for the solutions were placed on the side walls of the cell. The inlet was inclined towards the working electrode. The electrical contact with the working electrode was secured with two stainless steel screw terminals. Leakage was avoided by pressing both the working and the counter electrode against a suitable silicone o-ring. The reference electrode,

a miniaturized Ag/AgCl/KClsat electrode, was placed on the outlet tubing. This allocation allows contamination to be avoided and at the same time is sufficiently close to the working electrode to reduce the uncompensated resistance. For experiments on Silver single crystal a cell with 6.7mm inner diameter and a volume of about 1ml was used, for Ni electrode the electrochemical cell had a diameter of 10mm and a volume of about 1ml.

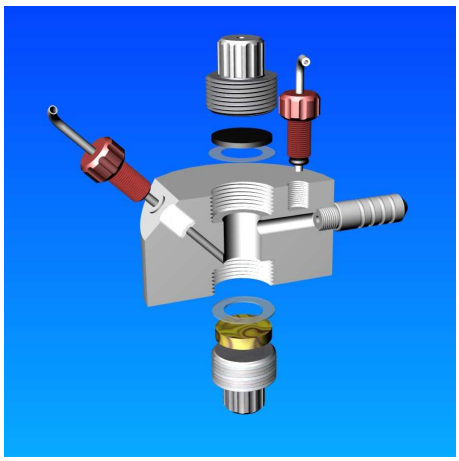

Figure 2.4: Flow cell used for electrochemical experiments.

Electrodeposition system

An automated deposition apparatus consisting of Pyrex solution reservoirs, solenoid valves and a distribution valve was used under the control of a computer. The distribution valve, entirely made of Teflon, was designed and manufactured in the workshop of our department [28]. The solutions contained in the Pyrex reservoirs are previously deaerated, and then constantly kept under an over pressure of about 0.3 atm of nitrogen. Fig. 2.5 shows the distribution valve connected to inlets for six solutions. The flask inner pressure is sufficient to push the solution out to the distribution valve. The piston of the distribution valve is tightly held by a spring to block the inlet of the solution and can be raised opening the solenoid valve and by sending compressed air at 3 atm, that is at a pressure higher than that exerted by the spring. The spring is raised just enough to expose the solution inlet, but not to allow compressed air to reach the solution outlet and go to the cell. By acting on the corresponding solenoid valves, the different solu-

tions are pushed to the electrochemical cell (see previous section) following the desired sequence. The pressure of 0.3 atm exerted on the solutions determines a flow-rate of about 1 mls^{-1}. This system is particularly suitable for the electrodeposition of compounds by electrochemical atomic layer epitaxy method, which is based on the alternate electrodeposition of the elements which form the compound at underpotential.

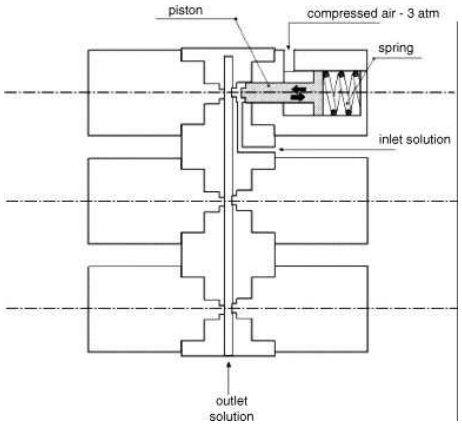

Figure 2.5: Scheme of the distribution valve connected to six solution inlets. The detailed specification of one of the solution inlet explains the system working. A given solution is pushed to the cell when the piston is raised by the pressure exerted by compressed air when the corresponding solenoid valve is acted.

2.3.6 Electrodes

Silver single crystal

Silver single crystal electrodes were obtained from single crystal spheres grown in a graphite crucible according to the Bridgman technique. They have been oriented and cut along the crystallographic direction in order to obtain Ag(111), Ag(110) and Ag(100) oriented electrodes [29]. Electrodes orientation was checked in SXRD experiments, measured miscut angle was less than 1°. The electrodes were polished with emery paper (BuehlerMet SiC P1000, p2500, P4000) and successively finer grades of alumina powder down to 0.05 μm (Buehler Micropolish II). Before each measurements, the electrode was cleaned with water in ultrasonic bath for 15 minutes and chemically polished with CrO_3 according to the procedure described in [29–

31]. To eliminate possible organic contaminants on the surface, the electrode was finally soaked in concentrated sulfuric acid for about 20 minutes and then rinsed thoroughly with double distilled water.

Ni policrystalline electrode

Ni flat electrode Nickel policrystalline electrode were prepared using a Nickel foil (99.5%) from Alfa Aesar. Nickel foil was cut in order to obtain disc electrodes with a diameter of about 15mm and 2mm thick. The electrodes were polished with emery paper (BuehlerMet SiC P1000,p2500, P4000) and successively finer grades of alumina powder down to 0.05μm (Buehler Micropolish II). Before each measurements, the electrode was polished with alumina 0.05μm and then cleaned with water in ultrasonic bath for 15 minutes.

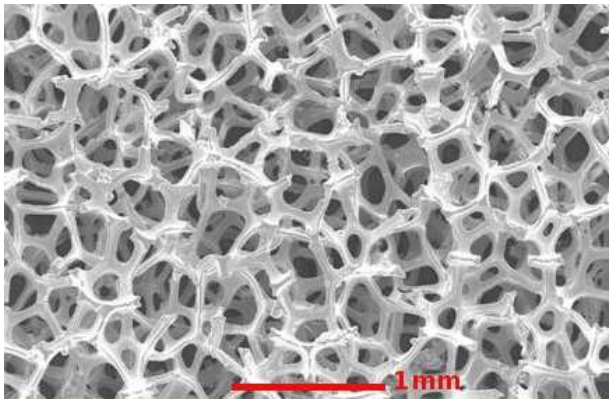

Figure 2.6: Optical microscope image of commercial Ni foam used for the electrode preparation.

Ni foam Ni foam electrodes were obtained from commercial Nickel foam sheets (Hohsen Corp., Japan). Foam characteristics declared by the seller are: cell size 0.45mm, surface area m^2/m^3 8500, thickness 1.2mm. The electrodes were prepared cutting the Ni foam sheet in pieces of about $30\times35mm^2$ size and cleaning them according to the following sequence:

- Ultrasonic bath for 20 minutes in double distilled water.
- Ultrasonic bath for 20 minutes in Acetone.

- wash with water and dip for 10 minutes in a HCl 0.1M solution.
- Ultrasonic bath for 20 minutes in double distilled water.

Before each measurement, the electrode was mounted in the cell and kept at the hydrogen evolution potential in order to remove surface oxides and hydroxide.

Chapter 3

CdS Electrodeposition on Silver

Recently, interest in the underpotential electrodeposition of elements has increased essentially due to potential applications in several fields of technology such as photovoltaics and electrocatalysis. One example is the possibility of depositing alternate UPD layers of metals and non-metals to grow binary and ternary compound semiconductors. This methodology is the basis of the electrochemical atomic layer epitaxy (ECALE) method proposed by Stickney and co-workers. The use of single crystals increases the probability for epitaxial growth, since the high-order structure of the first UPD layer, that is, the layer of the first element deposited on the metal used as a substrate, favors the ordered deposition of the second layer and of the successive ones. In other words, the crystallinity of the substrate is at least partially transferred to the compound during the growth. As a matter of fact, cadmium sulfides obtained on Ag(111) exhibit crystalline structures and have good semiconductor properties [28, 32, 33]. Therefore, the possibility of controlling the deposition of the first layer is of fundamental importance for the quality of the final product. In the first section of this chapter we report results of the in-situ STM analysis on sulphur UPD electrodeposition on Ag(110) and Ag(100). The effects of the different substrate orientation on a CdS film grown on the same substrates by ECALE are discussed in the second section. In the third section the possibility of appling ECALE growth for electrodeposition at nanometer scale by using thiol self assembled monolayer is treated.

3.1 S adlayer on Ag

The STM investigation of S UPD on Ag(111) revealed two main structures depending on the applied potential: a $(\sqrt{3} \times \sqrt{3})$R**30°** at potentials positive to 1.1 V/SCE and a $(\sqrt{7} \times \sqrt{7})$R**19.1°**, marked by a transition peak, at 0.89 V/SCE [34]. The latter structure confirmed previous results obtained by Rovida in UHV [35]. A complete survey of the behavior of molecular S_2 on Ag(111) in UHV was recently proposed by Yu et al. [36] who used different techniques, such as STM, LEED, XPS, and NIXSW, to obtain surface characterization and further structural information. Interestingly, they proposed the same $(\sqrt{7} \times \sqrt{7})$R**19.1°** structure for both sulfur and methanethiolate formed on the surface. And, in fact, the phase formed by sulfur on a silver surface is important as a starting point to determine the structural organization of thiols and, in general, of molecules adsorbed by the thiol group onto a specific surface [37]. Moreover, a sulfur adlayer deposited on silver is an appropriate substrate to investigate adsorbed organic molecules, since the weak van der Waals interactions of the S-molecule drive self-ordering processes better than strong molecule-surface interactions that hinder molecule mobility [38]. In this work, we present electrochemical measurements and electrochemical scanning tunneling microscopy (EC-STM) results obtained for the underpotential deposition of sulfur on Ag(100) and on Ag(110). Apart from the electrochemical measurements reported by White and co-workers [39, 40], there are few papers concerning STM measurements on Ag(100) and on Ag(110) surfaces. It is worthwhile to mention the structures of sulfate and ethanethiol on Ag(111) and Ag(100) [41, 42]. An incommensurate (1.3×3) superstructure of sulfate or bisulfate was observed on Ag(100), whereas, unlike other (111) metal surfaces studied, an unusual c$(\mathbf{3 \times 3\sqrt{3}})$ superstructure with four ions per unit cell was found on Ag(111) and nonordered adlayers were found on Ag(110). Ethanethiol self-assembled monolayers form ordered structures: a square arrangement of an incommensurate structure with a nearest neighbor distance of 0.44 nm was found on Ag(100), whereas a $(\sqrt{7} \times \sqrt{7})$R**19.1°** structure with two different adsorption sites and with three molecules per cell was found on Ag(111). Sulfur adsorption was already the object of STM in situ studies on other metal single crystals, such as Au and Cu. On these metals, the process was studied on faces (111) [43–45] and (100) [46,47]. Sulfide adsorption on single crystals should be treated from a more general point of view together with the adsorption of other anions. To this end, interested readers are referred to the outstanding review of Magnussen on the ordered anion adlayers on metal electrode surfaces [48]. The kinetics and electrosorption

valency of sulfide and halides adsorption on Ag(111) has been studied by our group [49, 50].

3.1.1 Cyclic voltammetry

A voltammetric study was performed with the electrochemical cell and the crystals described above. Cyclic voltammograms were performed in 1 mM Na_2S and 0.1 M NaOH solutions (pH=13) in the sulfur underpotential deposition region. This high pH value was chosen to avoid hydrogen evolution that could mask the negative peaks due to sulfur UPD and to ensure the presence of only one sulfur-containing species in the solution, i.e., HS^-. It

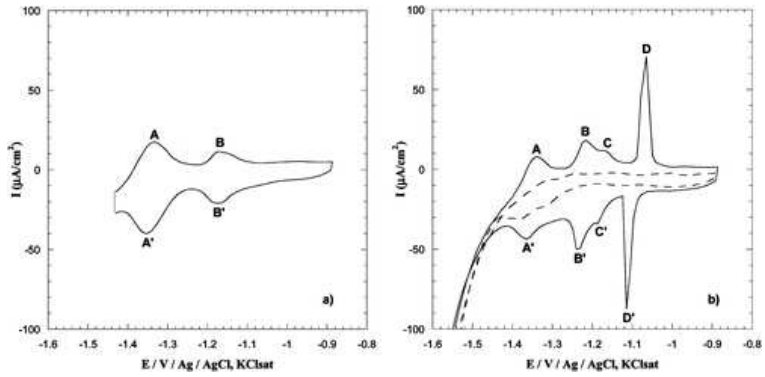

Figure 3.1: Cyclic voltammograms of Ag(100) (a) and Ag(110) (solid line in (b)) in 1 mM Na_2S in 0,1 M NaOH solutions. Scan rate 50 mVs^{-1}. The dashed line in (b) refers to the supporting electrolyte NaOH on Ag(110).

must be noted that the voltammograms obtained in the STM cell are similar to those reported in the literature ([39, 40]) thus suggesting that no leakage of Cl^- occurs during experiments. Cycling the potential between 1.45 and 0.9 V on Ag(100) yields only two broad anodic peaks at 1.32 V (A) and 1.15 V (B) with the corresponding cathodic peaks A' and B' (Figure 3.1a). On the contrary, cycling the potential between 1.55 and 0.9 V on Ag(110) yields three partially overlapping anodic peaks at 1.34 (A), 1.22 (B), and 1.17 (C) and a sharper one at 1.06 V (D) with the corresponding cathodic peaks A', B', C', and D' (solid curve in Figure 3.1b). It is worthwhile to note that on Ag(110) and Ag(100) the underpotential deposition of sulfur occurs at more negative potentials than on Ag(111) ([34, 39, 51]), in agreement with the more negative value of the potential of zero charge (pzc) of these faces. (The potential of zero charge of the faces (111), (100), and (110), as mea-

sured in an aspecifically adsorbed electrolyte such as KPF_6, are 0.695, 0.865, and 0.975 V/SCE respectively ([52]). Apart from the values of the potential, the shape of S UPD on Ag(110) is similar to the one reported for Ag(111). In particular, the very narrow and sharp shape of peak D seems to indicate a two-dimensional phase transition similar to that proposed for Ag(111) on the basis of a chronocoulometric investigation [49]. An analogous chronocoulometric investigation carried out for Ag(110) did not give satisfactory results. However, the presence of two-dimensional phase transitions taking place in electrode processes was determined by cyclic voltammetry, by scanning the potential in the UPD region from low to moderately high scan rates (v) and measuring the current peak, I_p, the peak's half-width, $\Delta E_{p/2}$ (i.e., the width, in millivolts, at the peak's half-height) and the difference, ΔE_p, between the reduction and oxidation peak potentials [53]. In the presence of two-dimensional growth mechanism, plotting log I_p, log $\Delta E_{p/2}$ and log ΔE_p against log v should yield slopes of 0.6, 0.4, and 0.4, respectively. The analysis carried out on the UPD region of S on Ag(110) yielded the expected slope values.

3.1.2 Chronocoulometric Measurements

The charges involved in the UPD region were accurately calculated using potential-step chronocoulometry. To this end, the applied potential was stepped from a variable initial potential to a fixed final potential $E_f = 1.5$ V, at which sulfide desorption is rapid and almost complete, and the resulting current was analogically integrated over time. The initial potential E was progressively varied from 1.5 to 0.9 V in 25 mV increments. The rest time at potential E was made long enough to ensure the attainment of adsorption equilibrium. Plotting the cathodic charge density Q(E,t) vs time t showed an

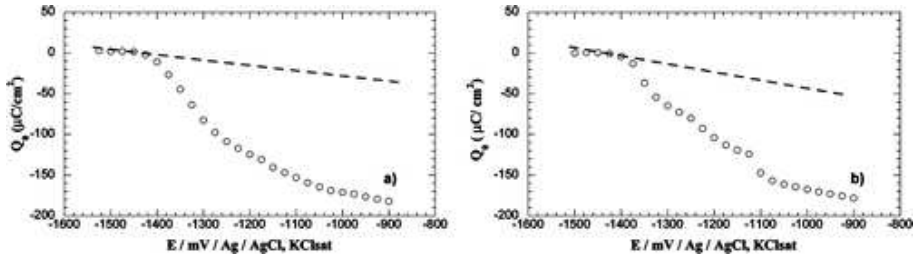

Figure 3.2: Chronocoulometric charge vs potential curves for Ag(100) (a) and Ag(110) (b) 0.1 M NaOH in the absence (dashed lines) and in the presence of 1 mM Na_2S (circles).

abrupt rise followed by a modest linear increase in time due to the current of hydrogen evolution, which is constant at $\boldsymbol{E_f}$. Linear extrapolation of these plots to t=0 yielded the charge density, $\mathbf{Q_0}$, corrected for the faradaic contribution due to hydrogen evolution. The curves indicated by circles in Figure 3.2 show the plotting of $\mathbf{Q_0}$ vs $\boldsymbol{E}$ obtained for Ag(100) (a) and for Ag(110) (b). Note that for Ag(110) the charge plot (Figure 3.2b) shows a slight inflection corresponding to the transition from peak A to peaks (B+C) of Figure 3.1b and two well-defined plateaus corresponding to the potential region between peaks C and D and to the region positive to peak D, respectively. Apart from the potential range, this behavior is identical to the one observed on Ag(111) and reported before [34]. Dashed lines in Figure 3.2 are the $\mathbf{Q_0}$ vs E plots provided by 0.1 M NaOH under otherwise identical conditions. The vertical distances between the plateaus of both the circles curves and their corresponding dashed ones give the charges involved in the sulfur UPD region. These charges are 163 $\boldsymbol{\mu}$Ccm$^{\mathbf{-2}}$ for Ag(100) and 137 $\boldsymbol{\mu}$Ccm$^{\mathbf{-2}}$ for Ag(110). Retaining the results previously obtained on Ag(111) [50], we assumed that at the most positive potentials investigated, an almost complete charge transfer of two electrons per sulfide ions occurred. Thus, considering that the area of the surface unit cell for Ag(100) is 8.35Å$^{\mathbf{2}}$ and that for Ag(110) is 11.81Å$^{\mathbf{2}}$, the respective coverage values are $\boldsymbol{\theta}$=0.42 and $\boldsymbol{\theta}$=0.50. The coverage obtained on Ag(111) with the same procedure was $\boldsymbol{\theta}$=0.43 [34].

3.1.3 STM Investigation of Sulfur on Ag(100)

The silver (100) crystal, prepared as described above, was brought into contact with the electrolyte at a potential of 1.5 V, at which sulfur was not adsorbed, and then the potential was scanned in the positive direction. Because of the closeness of hydrogen evolution to the beginning of sulfur deposition, it was not possible to image the bare silver substrate before deposition to have a direct relationship between structure and substrate. Therefore, all STM images reported hereafter refer to the default instrument calibration. However, the distances reported in the text as well as in the profiles of Figure 3.4 have been calculated on the basis of the calibration determined in a separate experiment on graphite HOPG. The large scale morphology of the surfaces remained nearly unchanged both in the absence or presence of sulfur in solution. In both cases the surface appeared to be composed of atomically smooth terraces separated by atomic steps. The atomically resolved topography of a little silver terrace covered by the sulfur adlayer clearly indicates its square geometry, whose measured lattice constants are

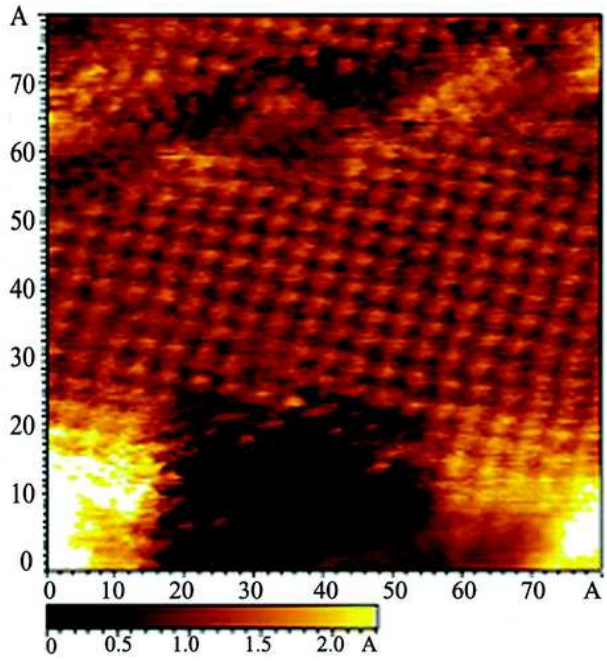

Figure 3.3: 8nm×8nm STM image of Ag(100) in 1 mM Na_2S, 0.1 M NaOH. Electrode potential E =1.25V, IT=1.2nA, UB=0.71V.

0.57±0.01 and 0.58±0.01 nm (Figure 3.3). Such values are close to double the lattice constant of Ag(100), in agreement with a 0.25 coverage p(2×2), in which sulfur atoms are situated in equivalent highly coordinated 4-fold sites. This structure will be referred as phase I, whose schematic representation will be shown later in Figure 3.4. A positive potential scan beyond peak B of Figure 3.1a led to a phase transition that resulted in a more dense structure (referred to as phase II in Figure 3.4) in which atoms are ordered in pairs of spots forming parallel rows. The STM image in Figure 3.4 shows various domains of phase II meeting perpendicularly. Profile a shows that the distance between two S atoms in a row is 0.57±0.01 nm whereas in profile b the distance between aligned pairs is 0.41±0.01nm within a pair and 0.83±0.01nm between two adjoining rows. Thus, single rows are made up of pairs of atoms spaced from each other 2 times the Ag lattice constant ($\boldsymbol{2r_{Ag}}$) and are composed of atoms that are distant $\boldsymbol{\sqrt{2}r_{Ag}}$ from each other. The proposed structure of geometry c(2×6) and coverage 0.33 again considers atoms sitting in alternating 4-fold sites, confirmed by the constant intensity

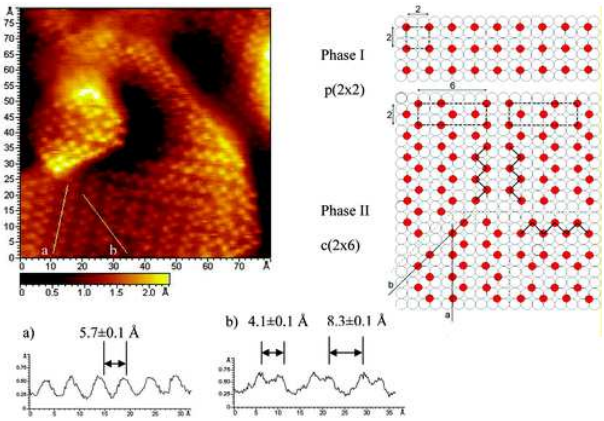

Figure 3.4: Left: 8nm×8nm STM image of Ag(100) in 1 mM Na_2S, 0.1 M NaOH. Electrode potential E=1.0V, IT=4.5nA, UB=0.18V. (a) and (b) are cross-section profiles of the lines in the image. Right: schematic ball-model structures of sulfur phases I and II on Ag(100). In the model for phase II perpendicular rows made up of paired spots are connected and profiles a and b are drawn.

of the brightness of the spots. Imaging of both structures I and II in a single experiment (Figure 3.5) allowed us to compare their lattice directions and dimensions. Figure 3.5 shows the transition phase due to the potential step from 1.0 to 1.25 V. It can be noted that the direction of the main rows in phase II is the same as that in phase I. Both Figures 3.4 and 3.5 show that phase II forms two domains rotated by 90° with respect to each other, as can be expected for a rectangular adlattice on the square substrate. Increasing the potential to 0.9 V reveals large areas of a compact adlayer (Figure 3.6). These areas are rotated 45° compared to the phase II layer and have a shorter SS distance, which would indicate a c(2×2) structure corresponding to 0.5 coverage (see the schematic representation in Figure 3.6). It must be noted that on Cu(100) the sulfur adlayer forms structures analogous to those formed on Ag(100), with the exception that the Cu lattice constant is too small to allow for the formation of the c(2×2) phase [46]. On the contrary, the c(2×2) structure is formed on Au(100) whose lattice constant is equal to that of Ag(100) [47].

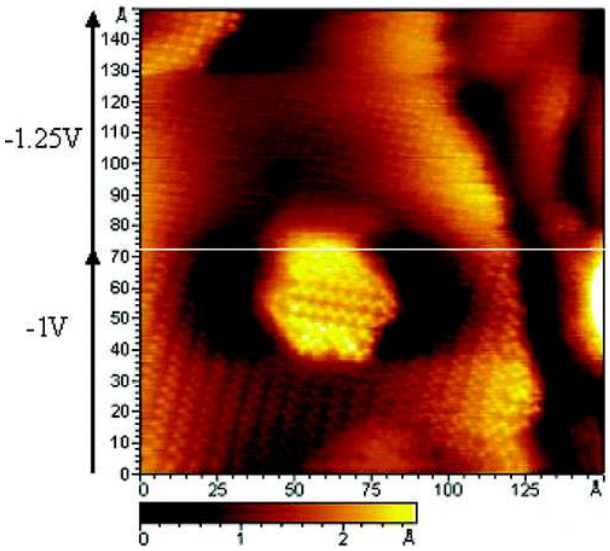

Figure 3.5: 15nm×15nm STM image of Ag(100) in 1 mM Na_2S, 0.1M NaOH. Electrode potential: lower part, E =1.0V, phase II; upper part, E=1.25V, phase I. IT=4.5nA, UB=0.43V.

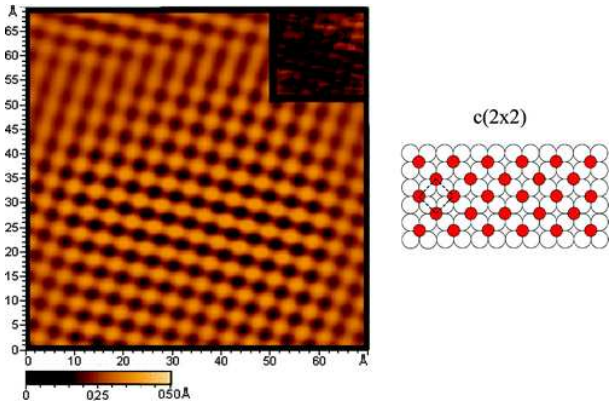

Figure 3.6: On the left: 7nm×7nm STM image of Ag(100) in 1 mM Na_2S, 0.1 M NaOH. E=0.9, IT=1nA, UB=0.20V. The image is band-pass filtered, and an inset of the original image is placed in the upper right corner. Right: schematic ball-model structure of sulfur phase c(2×2) on Ag(100).

3.1.4 STM Investigation of Sulfur on Ag(110)

It is well-known that single crystal surfaces characterized by low density elementary cells result in more stepped surfaces. Among the low Miller index

faces of silver, for example, the achievement of atomically flat terraces decreases with the order of atomic density: Ag(111)>Ag(100)>Ag(110).(25) The problems connected with silver surface preparation explain why STM investigations are more frequently carried out on Ag(111) and Ag(100) than on Ag(110). Furthermore, the study of the early stages of deposition is complicated by the overlapping of hydrogen evolution that is catalyzed by sulfur. Therefore, STM measurements performed at E =1.2V show Ag(110) surfaces

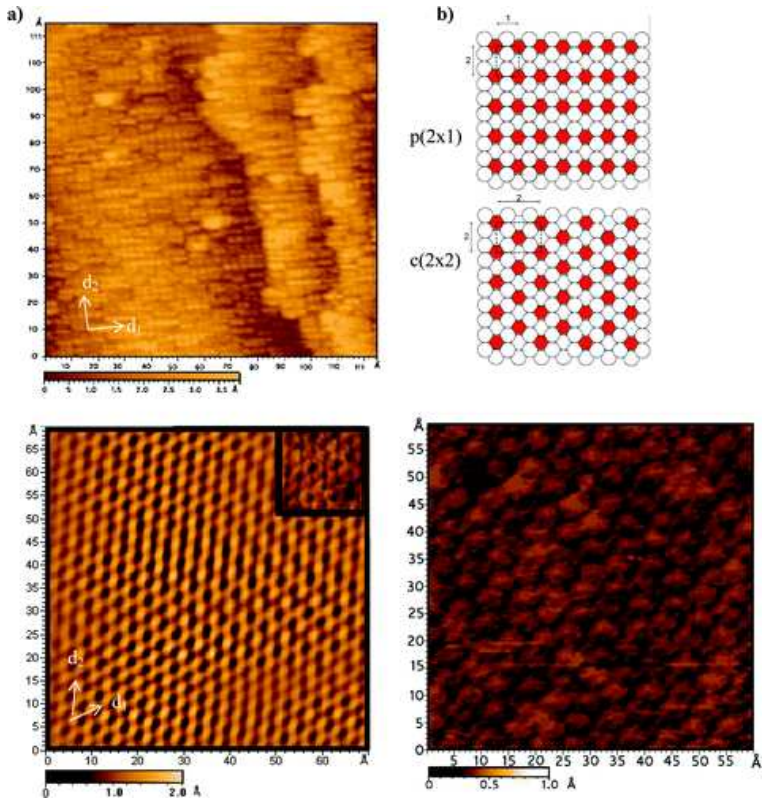

Figure 3.7

already covered by the earliest aligned sulfur deposits. Figure 3.7a shows rows of incomplete sulfur deposits, interrupted by several vacancies. From that image, the measurement of the distances between sulfur atoms within a row and between two adjoining rows yields 0.42±0.01 nm in the direction indicated by arrow d1 and 0.57±0.02nm in the direction indicated by arrow d_2. The position of the crystallographic axes of Ag(110) underneath the sul-

fur layer cannot be unambiguously identified. In fact, the uncovered surface of silver (110) could be imaged only at very negative potentials where hydrogen evolution hinders STM measurements. However, such distances are close to the characteristic lattice constants of Ag(110), respectively twice the AgAg nearest neighbors distance $\mathbf{2}r_{Ag}$ and the distance between two (110) troughs $\sqrt{\mathbf{2}}r_{Ag}$). For this reason, we can reasonably suppose the formation of an incomplete structure of geometry p(2×1), as depicted in Figure 3.7b.

Before peak D of Figure 3.1b, the adlayer still appears formed by parallel lines conserving the same direction even at more positive potentials. A compact and uniform structure was observed only after the sharp peak D at E=1.0V (Figure 3.7c). Such a structure does not keep the rectangular geometry of p(2×1); conversely, it is a pseudohexagonal one. Parts a and c of Figure 3.7 refer to the same sample at E=1.2 and E=1.0V, respectively. We can observe a slight rotation of about 8° of $\mathbf{d_2}$ direction and a larger rotation of about 30° for $\mathbf{d_1}$ from Figure 3.7a to 3.7c. Distances between atoms from Figure 3.7c are 0.57±0.02nm along the $\mathbf{d_1}$ direction and 0.51±0.02nm along the $\mathbf{d_2}$ direction. The more defined structure formed after peak D of Figure 3.1b can also be observed in the image taken at 0.9V (Figure 3.7d). It should be noted that the impossibility of unambiguously determining the relationship of the sulfur adlayer with the crystallographic directions of the substrate makes us not completely sure of the structure hypothesized for the compact layer. However, the above findings are consistent with a c(2×2) structure with a coverage $\boldsymbol{\theta}$=0.5 (Figure 3.7b). Considering a two electron exchange per sulfide ion, the calculated value of transferred charge is 136 $\boldsymbol{\mu}$Ccm$^{\mathbf{-2}}$, in excellent agreement with the experimental value of 137 $\boldsymbol{\mu}$Ccm$^{\mathbf{-2}}$ obtained by the charge versus time plot within the potential range 1.5 V/0.9 V (Figure 3.2), which covers nearly the whole adsorption process.

3.2 CdS ECALE deposition on Ag(100) and Ag(110)

3.2.1 Cd UPD on Ag and Ag-S

The formation of the first layer of S on Ag(111), Ag(100) and Ag(110) has been already extensively discussed previously (section 3.1.1, page 29). Electrochemical measurements show that sulphur UPD deposition processes differ significantly on the three silver facets and, accordingly, in-situ STM experiments evidenced the presence of different ordered sulfur structures depending on the substrate orientation. Moreover, on Ag(110) and Ag(100) the UPD processes occur at more negative potentials than on Ag(111). In order to establish the ECALE electrodeposition conditions Cd behavior was investigated by cyclic voltammetry both on the bare Ag substrate and on silver covered by a Sulfur UPD layer (Fig. 3.8). In the latter case, after sulfur UPD deposition, the cell was washed with ammonia buffer to eliminate HS^- while keeping the potential at the value of potential of sulfur deposition. Then, the potential was shifted to 0.1V and the ammonia buffer was replaced by a 5mM $CdSO_4$ in pH 9.6 buffer solution. Figure 3.8 shows the UPD process of Cd on the three low-index faces of silver and on the same faces covered by a SUPD layer. It must be underlined that the figure only reports a single reduction/oxidation peak for each system examined, whereas on S-covered silver Cd underpotential deposition yields two consecutive UPD peaks. However, on Ag(100) the second UPD peak could be well observed only during the anodic scan, whereas the second reduction peaks partly merges with the first one and partly is masked by Cd bulk deposition. For this reason we limited the potential range of Fig. 3.8 to the one corresponding to the first UPD peak. Comparison between the different faces allows to verify that the potential of the reduction/oxidation peaks of Cd UPD process on the bare silver follows the trend of atomic density of the different faces. More precisely, the UPD process occurs at more positive potentials on the most compact (111) facet and then it follows the order (111)>(100)>(110). This is not surprising since this is also the trend of chemisorption processes on the same faces to which a UPD process could be assimilated. On S-covered silver substrates all underpotential deposition/reoxidation processes are expected to follow the same trend and to occur at still more positive potentials due to the more attractive interaction of Cd with S than with Ag. Indeed, this is generally verified with the exception of Cd deposition on S-covered Ag(100) that is practically coincident with the deposition of Cd on the bare Ag(100). This occurrence is an intriguing exception that deserves a deeper investigation, better by means of surface

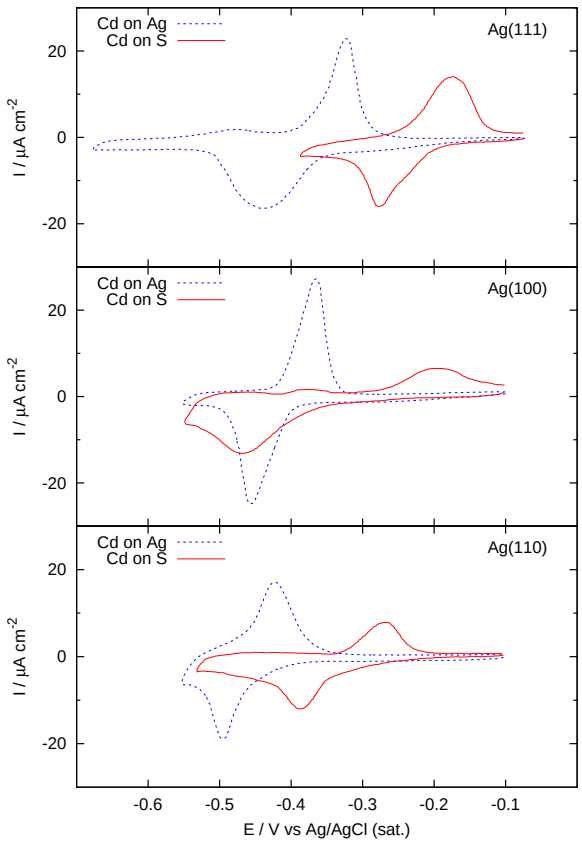

Figure 3.8: Cyclic voltammograms of Cd on S-covered and bare Ag(111) Ag(100) and Ag(110) from 5mM $CdSO_4$ in ammonia buffer pH=9.6 solutions. Scan rate 10mVs^{-1}.

technique such as STM. Tentatively, on the basis of the structural STM investigation that revealed the presence of only one structure of S on Ag(111) and on Ag(110) [54,55], but a mixture of two different structures on Ag(100), we can assume that a certain degree of "disorder" on Ag(100) could be responsible of a negative shift of potential for the deposition process. However, once the Cd monolayer is formed, its re-dissolution process is in range again with the other faces.

3.2.2 ECALE deposition and electrochemical characterization

The experimental sequence of the ECALE cycle necessary to obtain CdS on Ag(110) and Ag(100) was:

- Deposition of sulfur at -0.68V
- Washing of the cell with supporting electrolyte
- Deposition of cadmium at -0.6V
- Washing of the cell with supporting electrolyte

This basic sequence is repeated as many times as necessary to obtain thicker deposits. As usual the amount of the Cd and S deposited in a given number of cycles was estimated from the charge involved in the anodic stripping of Cd followed by the cathodic stripping of S. As already observed for CdS deposition on Ag(111) the stripping potential of Cadmium from CdS shifts as the number of deposition cycles increases, thus indicating that the compound is becoming more stable as the deposits thickness increases. The S layers remaining after Cd stripping, except for the first layer, behave like bulk sulfur: hence, during the subsequent reductive stripping, they are reduced at more positive potentials than the first S layer. The average charge deposited in each cycle is approximately $85\boldsymbol{\mu}\mathrm{Ccm}^{\mathbf{-2}}$. This value is calculated by plotting the charges obtained in the stripping of Cd and S as a function of the number of ECALE cycle.

3.2.3 Structural analysis

Two stable allotropic structure of CdS are known: wurtzite and zincblende. Structure of CdS thin films grown by ECALE on Ag(111) has been already investigated, and only the Wurtzite structure was reported [28, 32]. Since the film structure can be strongly influenced by the substrate lattice, the crystallographic structures of CdS films grown on Ag(100) and Ag(110) are expected to be different respect to the previous findings on Ag(111). X-ray diffraction experiments were carried out on samples prepared with 30 ECALE cycles deposition on Ag(100) and Ag(110) substrates as described above. Diffraction patterns of wurtzite and zincblende are quite similar and have many peaks in the same position. However, the two structures can be discriminated using different peaks, such as the (200) reflection for zincblende and the (101) and (103), which are the most intense and not

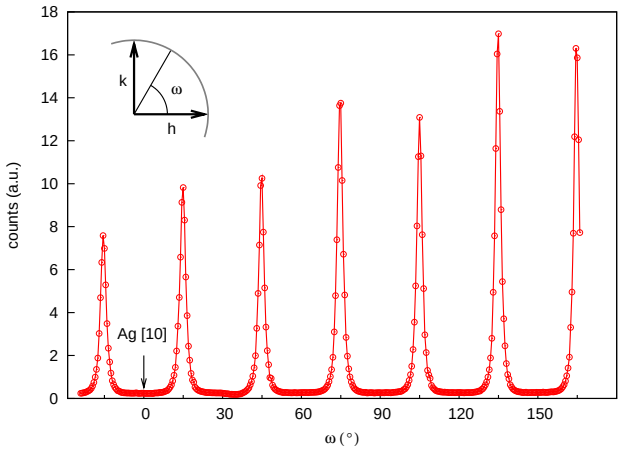

Figure 3.9: Azimuthal scan showing the (101) reflections of the wurtzite CdS lms on Ag(100). Two domains rotated by $\pm$**15°** with respect to the main axis are clearly visible.

overlapping peaks, for wurtzite. CdS zincblende and wurtzite structure are epitaxial with the directions perpendicular to the substrate surface, the [111] direction for the cubic structure and the [001] for the hexagonal one respectively. Characteristic diffraction peaks of the wurtzite structure were found in both kind of samples and the (200) reflection of zincblende was observed only in samples grown on Ag(110). Azimuthal scans in figure 3.9, 3.10 and 3.11 show the in plane orientation of CdS domains on Ag(100) and Ag(110). Wurtzite structure on Ag(100) (fig. 3.10) has two privileged direction of growth with the a-axis rotated respect to the main axes of the substrate of $\pm$**15°**. On Ag(110) there are two wurtzite domains aligned along the main axis of the silver substrates (fig. 3.10). Comparing diffracted intensity by the two domains it is evident that the growth of CdS is preferentially oriented along the longest axis in the direct space. CdS in Zincblende structure on Ag(110) substrates is rotated of $\pm$**45°** respect to the silver main axis (fig. 3.11). Comparing the normalized value of the diffracted intensity of the zincblende (200) and wurtzite (100) reflections shows that on Ag(110) CdS mainly grows with zincblende structure. Diffracted intensity maps in the reciprocal space shown in fig. 3.12 confirm the azimuthal scans results. Figure 3.13 shows the (00l) CTRs for Ag(100). The sample was aligned on the (002) Ag(111) reflection and the data were collected with a single scan. Data simulation is obtained by the sum of calculated structure factors of

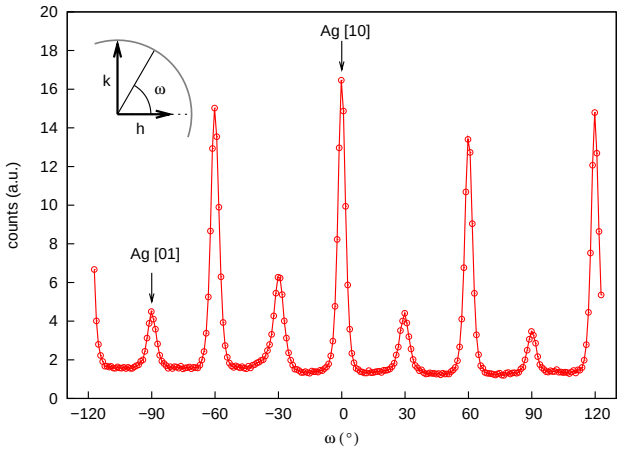

Figure 3.10: In plane orientation of CdS wurtzite film on Ag(110), (101) reflections. Azimuthal scan shows two CdS domains aligned along the substrate main axes. Intesities of the peaks suggest a preferential direction of growth along the h lattice vector.

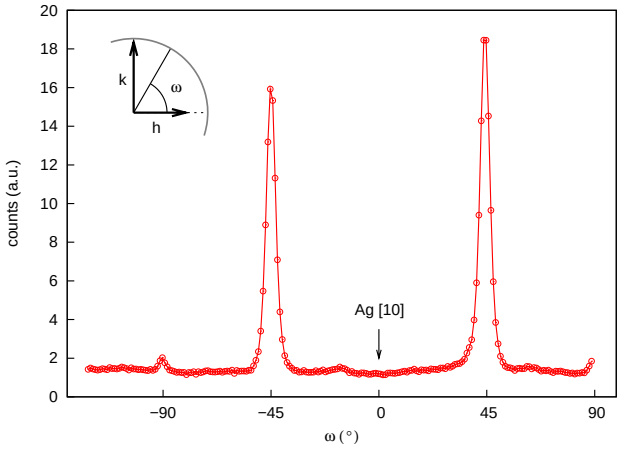

Figure 3.11: Azimuthal scan showing the in plane orientation of the Zincblende CdS structures on Ag(110). The position of the (200) reflections indicates a rotation of the structure of **45°** with respect to the silver main axis.

Ag and CdS. Diffracted intensity and fringes periodicity of the CdS films depends critically on the number of times the CdS unit cell is repeated along the $\boldsymbol{l}$ direction. CdS contribution to the diffracted intensity was calculated

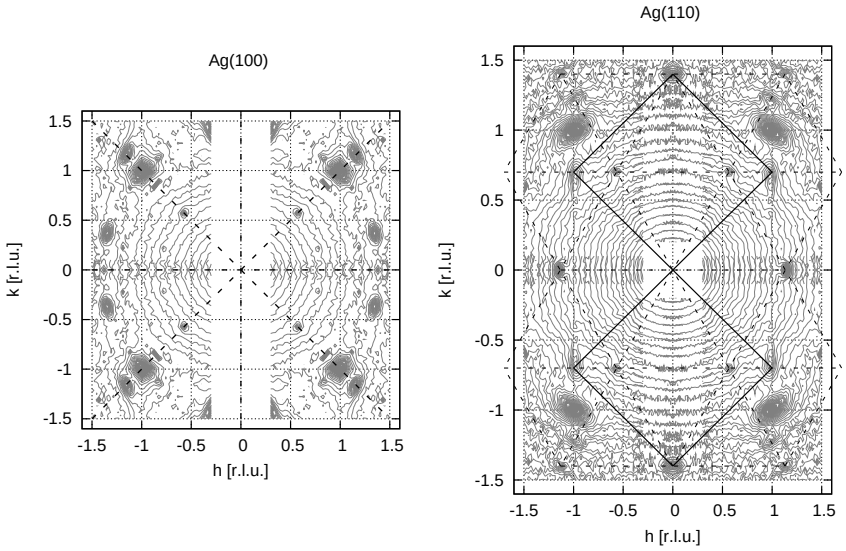

Figure 3.12: Mesh scans in the ***hk*** reciprocal space plane for ***l***=0. Diffraction pattern show the in plane orientations of CdS domains on Ag(100) and Ag(110).

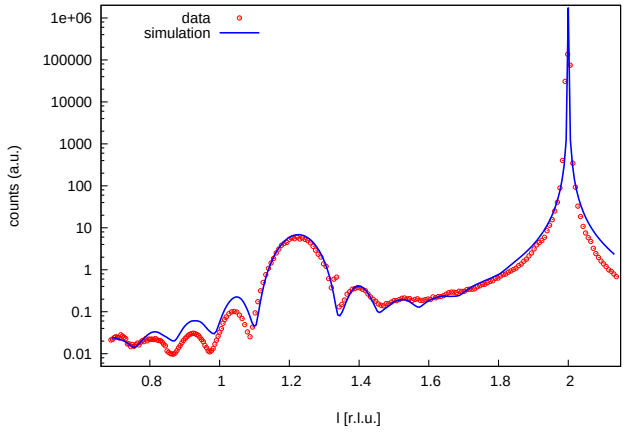

Figure 3.13: Specular Rod scan on CdS films on Ag(100).

using a model which assumes the presence of several CdS domains with different thickness stick side by side on the surface. Therefore CdS structure factor are calculated using a model of "extended" unit cell where the CdS unit cell is repeated several times along $\boldsymbol{l}$. Square structure factors of different "extended" unit cell are multiplied for a weighing factor and then summed together in order to simulate diffracted intensity. In our model we assume the existence of a most probable 'extended' unit cell that contributes mostly to the diffracted intensity. Weighing factor is assumed to be one for the most probable unit cell and a value from zero to one, calculated assuming a gaussian distribution, for the other contributions. Simulation can reproduce quite well fringes periodicity and the relations between intensity maxima, as shown in figure 3.13. Parameters used in the simulation establish that the most probable 'extended' unit cell is given by the repetition of 4.5 CdS unit cell, which corresponds to about 30Å.

3.2.4 film thickness

X-ray reflectivity data are reported in figure 3.14. Plots do not include data for values of the momentum transfer ($Q_{\boldsymbol{z}}$) below $0.15Å^{-1}$. This is because at low incidence angles the illuminated surface was larger than the surface spot covered by the CdS film, and, therefore, the reflected intensity also includes the contribution of the Ag surface. Since the CdS film is a circle spot of 6.5mm in diameter and the incident beam is about $200\boldsymbol{\mu}$m, reflectivity fit only for $Q_{\boldsymbol{z}}$ greater than $0.2Å^{-1}$. At any rate, fitting parameters match with the data reported for analogue CdS film on Ag(111) [28]. Calculated Scattering length density is $(3.60.2)\cdot 10\text{-}5Å^{-2}$ in agreement with the expected value of $3.63\cdot 10\text{-}5Å^{-2}$. Film thickness is 52.5 ± 0.5Å for CdS on Ag(110) and 46.5 ± 0.5Å for Ag(100). Film thickness calculated by XRR and (00l) Rod Simulation for Ag(100) samples differs of about 15Å. Difference is due to the presence of distorted CdS unit cells in contact with the silver surface lattice, which do not contribute to the diffracted intensity.

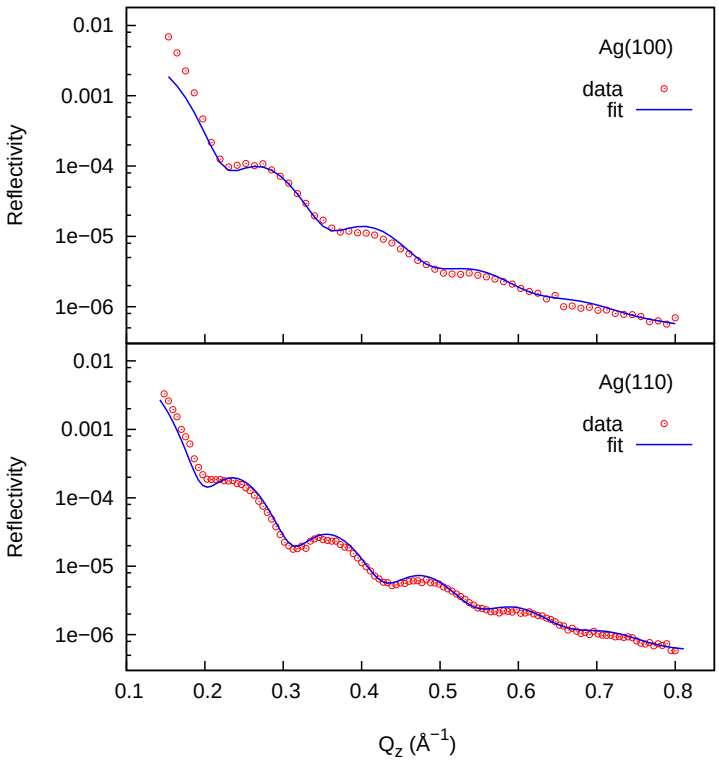

Figure 3.14: X-ray reflectivity measured from CdS films on Ag(100) and Ag(110). Fit of the data has been obtained using the same scattering density value of CdS canonical value, confirming the exact stoichiometry of the grown compound.

3.3 Confined electrodeposition on Ag(111)

The spontaneous coadsorption of two thiols from a binary mixed solution give a composite SAM [56]. This technique is useful for creating a continuous variation of functionalities by varying the molar fractions of the adsorbates. A binary composite SAM generally occurs either as a microscopically mixed phase or as two separate phases. Some binary SAMs [57–61] have shown homogeneous phases that have no detectable domains. In contrast, some authors [62–65] have suggested the presence of phase separation on a nanometer scale. The homogeneous mixture seems to be associated with a good affinity between two kinds of adsorbates. The affinity may generate a new redox state [60], which gives a new voltammetric wave at a potential between two potentials of the two reductive desorption waves [62]. When phase separation occurs binary selective desorption of a thiol can be electrochemically induced, leaving on an exposed electrochemically active surface. The resulting exposed area might be useful as an electrochemically active surface [66]. It has been well recognized that phase separation is caused on a molecular scale by the interaction energy between neighboring molecules, as is known from the van der Waals equation. When the interaction energy between hetero-species is predominant to that between homo-species, a phase separation is likely to occur. The spatial distribution of long and short thiols in binary SAMs is found to be influenced not only by their mole fractions but also by the degree of difference in the lengths between the two thiols or the presence of specific terminal groups. A quantitative relation between the interaction energy and the formation of domains for binary SAMs can be derived from a modification of the Ising model and Monte Carlo simulation provides thermodynamic quantities, distributions and domain sizes of the separated phases [67].

3.3.1 SAMs deposition on Ag(111)

An exhaustive discussion on the criteria used for assessment of the defects level in the monolayer is given by Miller et al. in ref 30. Here, electron tunneling through the full thickness of self-assembled organic monolayers of ω-hydroxy thiols is demonstrated. Briefly, the possibility of either small pinholes exposing the electrode surface, or collapse sites(31) causing the monolayer to be significantly thinner than the bulk monolayer film are taken into account. Because of the strong dependence of the electron-transfer kinetic on the thickness of the insulating film, even a small area containing such defects could be entirely responsible for the current measured. In order to

assess the effect of such defects, Miller et al. used the theoretical model of Amatore et al. for the redox kinetics at partially blocked electrodes.(32) According to this model, the presence of pinholes or collapse sites separated by distances greater than the characteristic diffusion length of the experiment (which, in our experiments, is of the order of tens of micrometers) should give rise to sigmoidal voltammetric waves. On the other hand, no blocking effect should be seen in the presence of defects separated by distances smaller than the characteristic diffusion length. Therefore, the use of suitable electrochemical redox probes such as $Ru(NH_3)_6^{2+/3+}$ allows us to evaluate the film quality. Figure 3.15 shows the cyclic voltammograms of 1 mM $Ru(NH_3)_6^{3+}$ as performed on bare Ag(111) (curve a) and on fully covered by OT Ag(111) substrates (curve b). On the basis of the above considerations, the monolayer of OT produces only a limited effect on the voltammetric peak, indicating either the presence of pinholes which act as an array of microelectrodes or an insufficient blocking effect of $Ru(NH_3)_6^{2+/3+}$ as observed in some cases with respect to other electrochemical redox probes such as $[Fe(CN)_6]^{3-/4-}$.(33) However, the limited double layer region of silver does not allow us to reach the positive potential values of ferro/ferricyanide redox couple or observe the oxidation wave of $Ru(NH_3)_6^{3+}$. On the other hand, the presence of defects is consistent with the possibility of depositing a small fraction of Cd_{UPD} on a single OT SAM. It must also be noted that the underpotential deposition is a surface sensitive phenomenon and, therefore, requires that free areas of Ag(111) are exposed to the solution. However, it is important to stress that the defects in the OT SAM are not caused by Electrochemical Atomic Layer Epitaxy (ECALE) electrodeposition, since they are already highlighted by the electrochemical probe. As reported in the literature, the compactness of a self-assembled monolayer can be estimated on the basis of the electron transfer kinetic [68–70]. Cyclic voltammograms of $[Ru(NH_3)_6]^{2+/3+}$ performed on Ag(111) fully covered by OT, Decanethiol (DT) or 1-DDT show an increasing compactness of the SAM 3.15. At the same time, 3.16 shows that the amount of defects decreases, as shown by the decreasing stripping peaks of Cd deposited at underpotential on OT, DT and 1-DDT, respectively. In fact, the stripping peak of Cd from OT/Ag(111) is about 16% of that on the bare Ag(111) and that of Cd from DT/Ag(111) is only 5%, whereas no deposits are formed on 1-DDT/Ag(111). Also note the negative potential shift of the peaks in 3.16 may be explained by the fact that diminished lateral interactions between the deposited CdS clusters make the re-dissolution process easier.The above analysis supports well the use of 1-DDT as a "long chain" thiol to combine

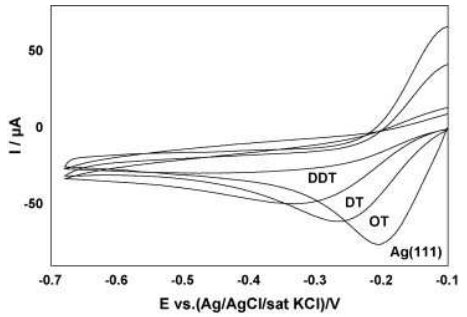

Figure 3.15: Cyclic voltammograms obtained from 1mM $Ru(NH_3)_6^{3+}$ in 0.1 M KCl on the bare Ag(111) and on Ag(111) fully covered by OT, DT, 1-DDT. The scan rate was 50 mV/s.

with 3-MPA.

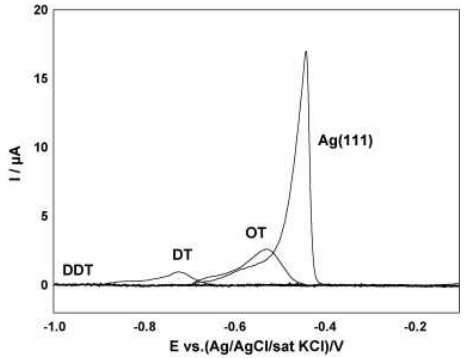

Figure 3.16: Stripping peaks of Cd deposited at underpotential on the bare Ag(111) and on Ag(111) fully covered by OT, DT, 1-DDT. The scan rate was 50 mV/s.

3.3.2 1-DDT-3-MPA binary SAMs

Electrochemical characterization

The surface molar ratio of the single thiols in a multicomponent SAM can be estimated by the charge involved in the desorption of each single component [66]. As already reported in the literature, the composition of the monolayers never equals the solution composition, since longer thiols tend to

occupy larger areas; yet, less pronounced differences are observed between composition in solution and on the surface on silver [71]. Fig. 3.17 shows the systematic voltammetric analysis performed by stripping binary SAMs obtained on Ag(111) by keeping the 1-DDT bulk concentration equal to 0.3 mM (Fig. 3.17 a) and varying that of 3-MPA from 0.3 to 0.9 mM (Fig. 3.17 b). More precisely, curves 1 are given by a solution 0.3 mM 1-DDT + 0.3 mM 3-MPA, curves 2 by 0.3 mM 1-DDT + 0.6 mM 3-MPA, and curves 3 by 0.3 mM 1-DDT + 0.9 mM 3-MPA. The corresponding surface molar

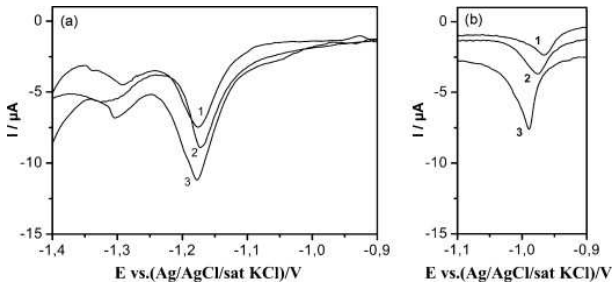

Figure 3.17: Stripping curves of 1-DDT in 0.5 M KOH in ethanol 90% (a) and of 3-MPA in 0.5 M KOH (b) from the binary SAMs obtained on Ag(1 1 1) in solutions: 0.3 mM 1-DDT + 0.3 mM 3-MPA (curves 1); 0.3 mM 1-DDT + 0.6 mM 3-MPA (curves 2); 0.3 mM 1-DDT + 0.9 mM 3-MPA (curves 3). The scan rate was 10 mV/s.

	c/mM	% in solution	% on silver surface
3-MPA	0.3	50	12
1-DDT	0.3	50	88
3-MPA	0.6	67	22
1-DDT	0.3	33	78
3-MPA	0.9	75	30
1-DDT	0.3	25	70

Table 3.1: Bulk and surface compositions of 3-MPA and 1-DDT.

ratios are reported in Table 3.3.2. As expected, the surface molar ratio of 3-MPA increases while increasing its bulk concentration. Note that while 3-

MPA stripping is performed in an aqueous KOH solution, 1-DDT stripping is performed in an alcoholic KOH solution where it is shifted towards less negative potential (Fig. 3.18b). In fact, in aqueous KOH solutions the 1-DDT stripping peak is hidden by hydrogen evolution even working at KOH concentrations as high as 0.5 M (Fig. 3.18a).

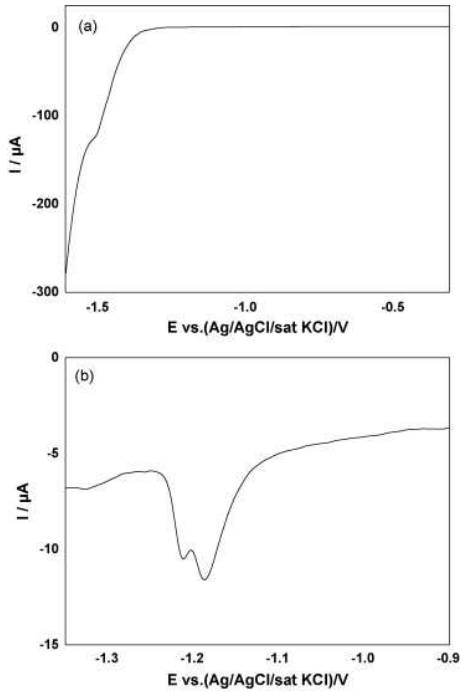

Figure 3.18: Stripping curves of the 1-DDT SAM formed on Ag(1 1 1) in 0.5 M KOH (a) and in 0.5 M KOH in ethanol 90% (b). The scan rate was 10 mV/s.

Confined CdS ECALE growth

Fig.3.17 suggests that suitable templates can be obtained by applying a potential equal to -1.1 V to the substrate covered by the binary SAM. It must be noted that in KOH this potential is not able to cause 1-DDT stripping since, as shown in Fig. 3.17a, its stripping peak is negatively shifted. Two different templates were obtained: template A corresponding to a SAM 22% in 3-MPA was obtained from a solution of 0.6 mM 3-MPA + 0.3 mM 1-DDT, and template B corresponding to a SAM 30% in 3-MPA was obtained

from a solution of 0.9 mM 3-MPA + 0.3 mM 1-DDT. The deposition of CdS and the electrochemical characterization of the compound obtained was performed according to the procedure as already described [33, 51, 54, 72, 73]. Accordingly, deposits obtained with an increasing number of cycles are electrochemically redissolved by measuring the charge involved in the stripping of Cd followed by the stripping of S. This procedure is usually employed to determine the amount of elements deposited in a given number of ECALE cycles. Fig. 3.19a shows the stripping peaks of Cd while increasing the num-

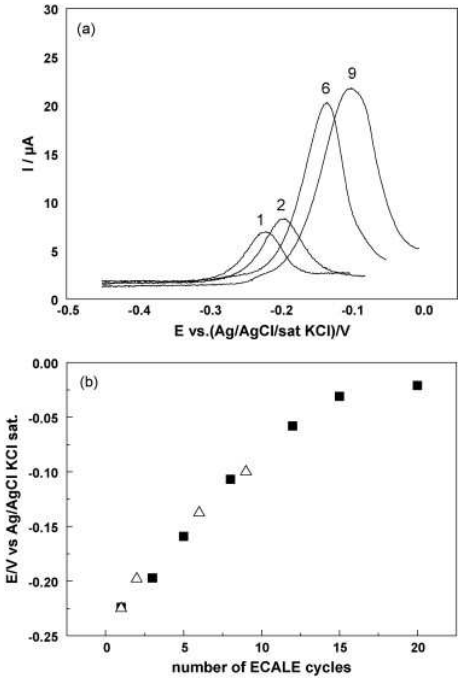

Figure 3.19: (a) Linear-sweep voltammograms for the Cd oxidative stripping from patterned CdS films deposited with 1,2,6 and 9 ECALE cycles (scan rate equal to 10 mV/s); (b) potentials of the stripping peaks as a function of the number of ECALE cycles for patterned CdS (square) and for CdS grown on bare Ag(111) (triangle).

ber of ECALE cycles. Apart from the current values, these curves exactly reproduce the stripping curves of CdS deposits grown on bare Ag(111) substrates [51]. As usual, the stripping process of the first element (in our case Cd) becomes progressively more difficult as the number of deposition cycles increases. As it has been shown previously [51] the observed potential shift

is much greater than that ascribable to the slow kinetics of the dissolution process and it is mostly due to an increasing stability of the compound up to the attainment of a limiting value. Fig. 3.19b shows that the potentials of the stripping peaks of Fig. 3.19a are in excellent agreement with those previously reported for CdS grown on bare Ag(111). It must also be noted that the well-defined shape of the stripping peaks of Fig. 3.19a suggests that all Cd is present as CdS. Another important conclusion suggested by Fig. 3.19 is that in both cases the thickness of the CdS film was proportional to the number of ECALE cycles used. Fig. 3.20 shows plots of the charges per

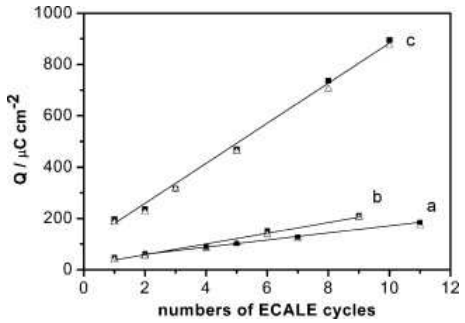

Figure 3.20: Plots of the charge involved in the oxidative stripping of Cd (square) and the reductive stripping of S (triangle) as a function of the number of ECALE cycles as obtained on template A (curve a), on template B (curve b) and that previously obtained on a bare Ag(111) substrate (curve c).

cm^2 for Cd and S strippings obtained from CdS deposited on template A (curve a), on template B (curve b) and that previously obtained [51] on a bare Ag(111) substrate (curve c). Fig. 3.20 and Fig. 3.20 show that the deposition process performed on the patterned Ag(111) is similar to the one performed on the bare Ag(111), with the obvious decrease in the amount of material, due to the reduced electrode surface. In particular, the coincidence of the charges associated with Cd and S strippings gives a 1:1 stoichiometric ratio between the elements as expected for the compound, and the linear increase of the deposit with the number of deposition cycles suggests the layer-by-layer growth mechanism that is the aim of ECALE method [51]. The slope of each plot gives the charge per cycle. The slope of 13 $\mu C/cm^2$ obtained on the template A and that, $21\mu C/cm^2$, obtained on the template B amount to 19% and 30% respectively of the slope, 70 $\mu C\ cm^{-2}$ [51], observed on the bare Ag(111). This result allows us to hypothesize that the silver area at disposal for the electrodeposition coincides with that of

desorbed 3-MPA.

Morphological characterization

The electrochemical characterization was completed with a morphological analysis performed on samples formed with 20 ECALE cycles on template A. According to the estimate of our CdS sample thickness made previously [51], this number of cycles should result in a CdS film thickness of about 4nm. The AFM topographic image shows that CdS clusters are distributed over

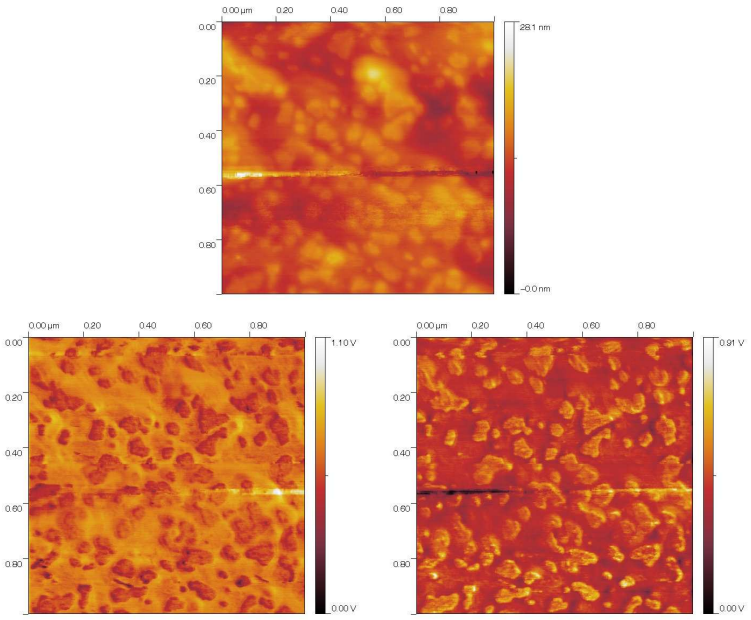

Figure 3.21: CdS deposited on template A: AFM topographic image (top), left-scanned LFM image (bottom left), and right-scanned LFM image (bottom right).

the whole surface (Fig. 3.21a). These clusters are better evidenced by the bright areas in the left-scanned LFM image (Fig. 3.21b) and by the dark areas in the right-scanned LFM image (Fig. 3.21c). The clusters have an average equivalent radius lower than 60nm. More precisely, the distribution analysis performed on different regions of the samples shows that most of them (95-98%) occupy an area lower than 5000nm^2 corresponding to an equivalent radius of about 40nm. The total area occupied by CdS, i.e. the

sum of the single clusters, always yields the value of 20±2% of the whole surface.

3.3.3 OT-3-MPA binaty SAMs

Electrochemical characterization

The first SAM investigated was obtained from mixtures of 0.3 mM OT and 1 mM 3-MPA in 99.8% ethanol. On gold, this solution composition gives rise to a homogeneous distribution that, after desorption of the shorter thiol, forms round holes. The stripping voltammetry of this binary SAM is that reported in Figure 1. The figure shows well-defined and distinct peaks with

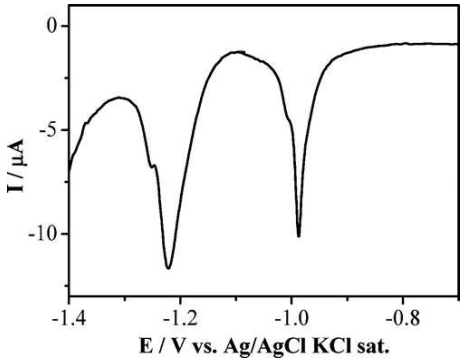

Figure 3.22: Stripping curves of the binary SAM obtained on Ag(111) from a solution of 0.3 mM OT and 1 mM 3-MPA. The scan rate was 10 mV/s.

only a slight positive shift (10mV) in the potential value of 3-MPA with respect to the single 3-MPA deposited on Ag(111). Integration of the area under the peaks yields the molar ratio of 40% in 3-MPA and 60% in OT. These values are different from those reported for the binary SAM formed on gold from the same solution composition [66]. In fact, as already reported in the literature, the composition of the monolayers rarely equals the solution composition, since longer thiols tend to occupy larger areas; yet, less pronounced differences are observed between composition in solution and on the surface on silver [57]. More particularly, Table 3.3.3 reports the direct comparison between our results on silver and those reported in reference [66] for gold. It must be noted that on Ag(111) equimolar solutions (either 0.3 mM 3-MPA + 0.3 mM OT or 1 mM 3-MPA + 1 mM OT) give the same surface molar ratios of 26% in 3-MPA and 74% in OT. Then to perform a systematic investigation, we kept constant the solution concentration of one

	3-MPA	OT
c/mM	1	0.3
% in solution	77	23
% on silver surface	40	60
% on gold surface	25	75

Table 3.2: Comparison between Our Results on Silver and Those Reported in Reference [57] for Gold

	c/mM	% in solution	% on silver surface
3-MPA	1	50	26
OT	1	50	74
3-MPA	0.3	50	26
OT	0.3	50	74
3-MPA	0.3	33	18
OT	0.6	67	82
3-MPA	0.3	25	8
OT	0.9	75	92

Table 3.3: bulk and surface compositions of 3-MPA and OT

alkanethiol, that is, 3-MPA, while varying the concentration of the other, that is, OT. As reported in Table 3.3.3, the surface molar ratio of OT increases with the increase in the bulk concentration of OT.
Selective desorption has been performed from SAM 26% in 3-MPA obtained from a solution 0.3 mM 3-MPA + 0.3 mM OT applying a potential equal to -1.05 V for 10 s in 0.5 M KOH. Figure 3.23 shows thath the stripping peak of the SAM remained after desorption. Both the potential and the area of the peak in Figure 3.23 coincide with those of the OT before desorption, with only a slight difference in the shape, probably due to a loss in the structure definition. This finding allows us to hypothesize that the silver area at disposal for the electrodeposition coincides with that of desorbed 3-MPA. Figure 3.24 shows the stripping curve of sulfur deposited at underpotential on bare Ag(111) (dashed curve) and on patterned Ag(111) (solid curve). From the figure, it is evident that even if the free area of silver is that which remains after selective desorption, the presence of the remaining OT SAM does not change the potential range of S UPD, whereas the decrease of the

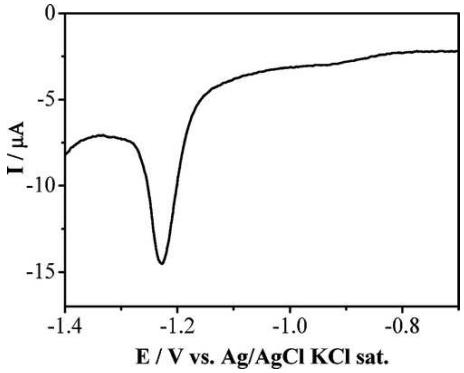

Figure 3.23: Stripping curves of OT remaining after desorption of 3-MPA at -1.05 V from the binary SAM obtained by a solution 0.3 mM in 3-MPA and 0.3 mM in OT. The scan rate was 10 mV/s.

stripping peak indicates a reduction of the silver surface. Similar behavior is observed for Cd UPD. However, the charge associated with the UPD peaks in the presence of OT is about 40% and, therefore, higher than the 25% left by 3-MPA. The discrepancy can be explained by the presence of defects in the OT SAM as shown by the stripping voltammetry of Cd deposited at underpotential on Ag(111) fully covered by OT (solid curve in Figure 3.25). The area of the small peak is about 16% of that obtained on the bare Ag(111) (dashed curve in Figure 3.25).

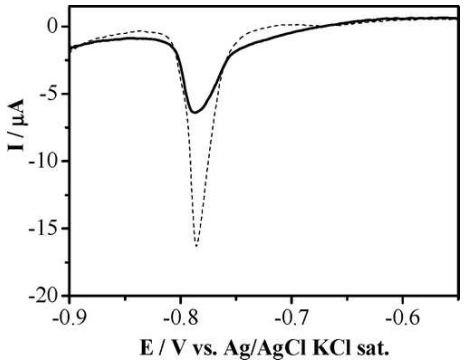

Figure 3.24: Stripping curves of S UPD deposited on bare (dashed curve) and patterned (solid curve) Ag(111). The scan rate was 10 mV/s.

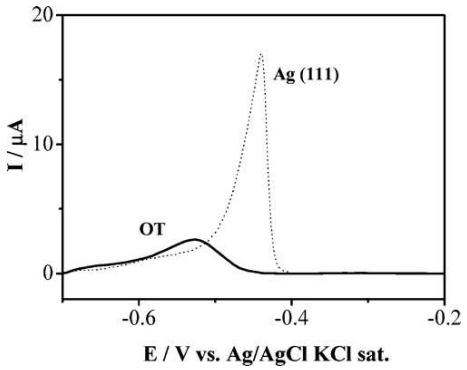

Figure 3.25: Stripping peaks of Cd deposited at underpotential on Ag(111) fully covered by OT (solid curve) and on bare Ag(111) (dashed curve). The scan rate was 10 mV/s.

Confined CdS ECALE growth

The template deposition of CdS was performed according to the procedure described in the Experimental subsection. Deposits obtained by progressively increasing the number of cycles were electrochemically redissolved to measure the charge, stripping first the Cd and then the S. Figure 3.26a shows the stripping peaks of Cd while increasing the number of ECALE cycles. Apart from the current values, these curves exactly reproduce the stripping curves of CdS deposits grown on bare Ag(111) substrates [51]. As usual, the stripping process of the first element (in our case Cd) becomes progressively more difficult as the number of deposition cycles increases. As it has been shown previously, [51] the observed potential shift is much greater than that ascribable to the slow kinetics of the dissolution process and it is mostly due to an increasing stability of the compound up to the attainment of a limiting value. Figure 6b shows that the potentials of the stripping peaks of Figure 3.26a are in excellent agreement with those previously reported for CdS grown on bare Ag(111) [51]. It must also be noted that the well-defined shape of the stripping peaks of Figure 3.26 suggests that all Cd is present as CdS. Another important conclusion suggested by Figure 3.26 is that in both cases the thickness of the CdS film was proportional to the number of ECALE cycles used. Integration of the stripping curves gives the amount of the elements deposited in a given number of ECALE cycles. Line a in Figure 3.27 shows plots of the charges per cm^2 for Cd and S strippings obtained from CdS deposited on a bare Ag(111)

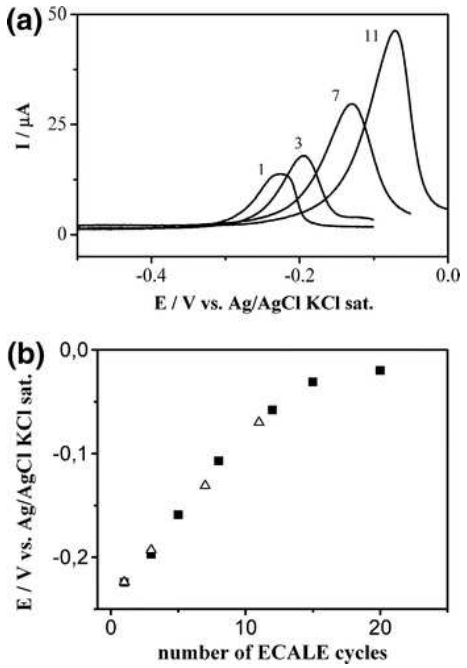

Figure 3.26: (a) Linear-sweep voltammograms for the Cd oxidative stripping from patterned CdS films deposited with 1, 3, 7, and 11 ECALE cycles (scan rate equal to 10 mV/s); (b) potentials of the stripping peaks as a function of the number of ECALE cycles for patterned CdS (triangle) and for CdS grown on bare Ag(111) (square).

substrate, [51] whereas line b shows the plots obtained from CdS deposited on our template substrates. Of course, in the latter case, this quantity is not to be considered as a true charge density, since the area is the geometrical area of the electrode and not the electrochemically active area. As showed above, the electrochemical characterization of the deposits of CdS on the patterned Ag(111) showed that the deposition process is similar to the one performed on the bare Ag(111), apart from a decrease in the amount of material, due to the reduced electrode surface. In particular, the coinciding charges associated with Cd and S strippings gives a 1:1 stoichiometric ratio between the elements as expected for the compound, and the linear increase of the deposit with the number of deposition cycles suggests a layer-by-layer growth mechanism that is the aim of ECALE method [51]. The slope of each line gives the charge per cycle. The slope of 28 $\boldsymbol{\mu}$Ccm$^{\mathbf{-2}}$ relative to the patterned Ag(111) amounts to 40% of the slope, 70 $\boldsymbol{\mu}$C/cm$^{\mathbf{2}}$ [51], relative

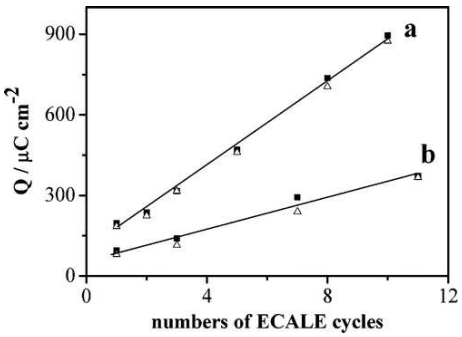

Figure 3.27: Plots of the charge per geometrical area involved in the oxidative stripping of Cd (square) and the reductive stripping of S (triangle) as a function of the number of ECALE cycles as obtained on bare (line a) and patterned (curve b) Ag(111).

to the bare Ag(111). It must be noted that this value confirms the previous observations.

Morphological characterization

The electrochemical characterization was completed with a morphological analysis performed on a CdS sample formed by 20 ECALE cycles. According to the estimate of our CdS sample thickness made previously [51], this number of cycles should result in a CdS film thickness of about 4nm. Figure 3.28 reports LFM images of samples obtained from solution with different concentrations of OT and 3-MPA (see table 3.3.3). The LFM images show that well-defined areas are of a different nature with respect to the homogeneous background, thus suggesting that they can be identified as clusters of CdS. An approximate evaluation obtained by summing the areas occupied by the clusters yields a CdS coverage in good agreement with the electrochemical results.

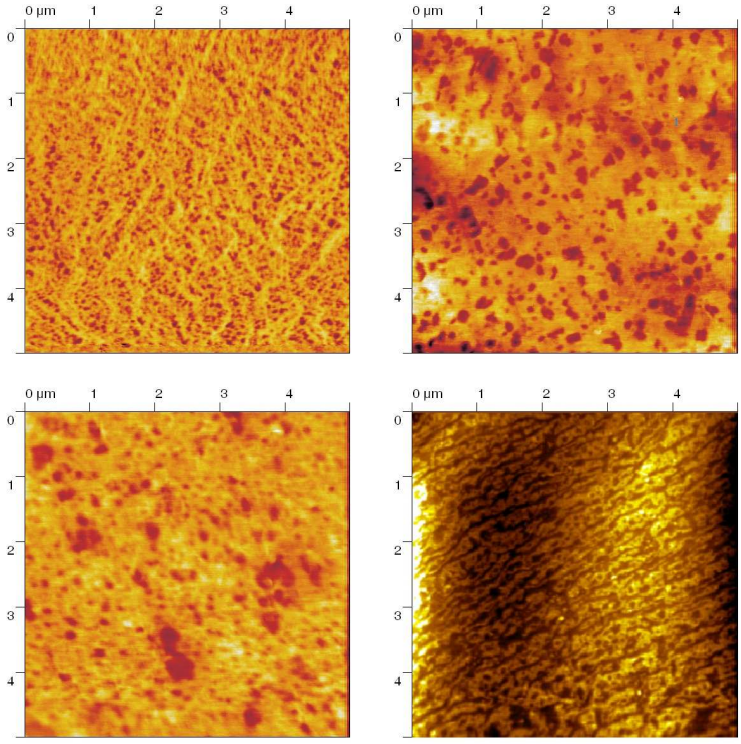

Figure 3.28: LFM images of patterned Ag(111) surface. Composition of the surface (measured by electrochemistry): top left 3-MPA 12%, top right 3-MPA 22%, bottom left 3-MPA 30%, bottom right 3-MPA 40%.

Chapter 4

Pd Electrodeposition on Nickel

Nickel represents an unique electrode metal of outstanding importance for practical industrial applications. Ni is located above palladium and platinum in the tenth group of the periodic table and although it is a non-noble metal it shares a lot of properties of noble metals. Due to its availability, low cost, corrosion resistance and its catalytic properties nickel is often employed for anodic and cathodic processes in industrial electrochemical production.

4.1 Ni electrochemical reactivity

4.1.1 Ni Pourbaix diagram

Two forms of Ni(II) can exist in aqueous solutions [74]: the hydrated $\boldsymbol{\alpha}$-$Ni(OH)_{\mathbf{2}}$ phase and the unhydrated $\boldsymbol{\beta}$-$Ni(OH)_{\mathbf{2}}$ which is the stable form of the hydroxide. The real composition of the $\boldsymbol{\alpha}$-hydroxide may be represented as $Ni(OH)_{\mathbf{2}} \cdot \boldsymbol{x}H_{\mathbf{2}}O$, where $0.5 < \boldsymbol{x} < 0.7$ [75]. Dehydration of the $\boldsymbol{\alpha}$-phase can occur either by ageing $\boldsymbol{\alpha}$-$Ni(OH)_{\mathbf{2}}$ or by electrochemical treatment [75]. The oxidation of nickel hydroxide in highly alkaline media produces solid oxides with semiconductor properties. In general, the oxidation product of $\boldsymbol{\beta}$-$Ni(OH)_{\mathbf{2}}$ is denoted as the $\boldsymbol{\beta}$-phase ($\boldsymbol{\beta}$-NiOOH), while oxidation of $\boldsymbol{\alpha}$-$Ni(OH)_{\mathbf{2}}$ is considered to give a $\boldsymbol{\gamma}$-phase. These processes are often described with the reaction $Ni(OH)_{\mathbf{2}} \rightleftharpoons NiOOH + H^{+} + e^{-}$, which is obviously an oversimplification [74–76]. A detailed Pourbaix diagram in aqueous solution was proposed by Beverskog and cooworkers [77] and it's reported in figure 4.1.

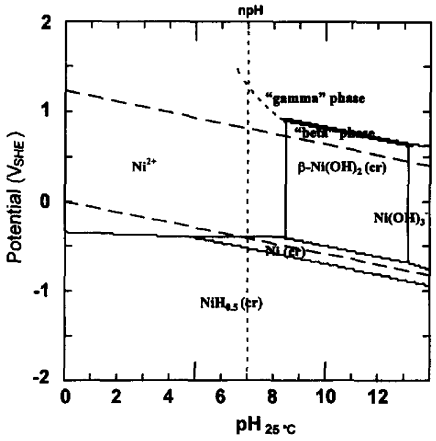

Figure 4.1: Pourbaix diagram for Ni at 25˚ [77].

4.1.2 Ni electrochemistry

In recent years detailed studies on Ni electrochemical oxidation have been reported. Ex-situ and in-situ experiments conducted mainly by XPS, surface X-ray scattering and STM on nickel single crystal electrode have investigated the composition and the structural properties of Ni-oxides and hydroxide thin films.

Acidic media

In acidic electrolytes Ni surface is passivated at positive potential. Passive film is a duplex structure consisting of a NiO layer with an overlaying layer of $Ni(OH)_2$ [78–80]. Cyclic voltammetry at pH=0 is reported in figure 4.2, the anodic peak is due to nickel dissolution reaction before the formation of the Ni oxide passivation layer.

Alkaline media

Nickel electrochemical behaviour in alkaline electrolytes is more complex than in acidic media and the exact nature of oxide/hydroxide species formed on the Ni surface is still discussed. The cyclic voltammetry for Ni policrystalline electrode in phosphate buffer pH 12.5 is shown in figure 4.3. According to the Pourbaix diagram and the literature [81] the following reactions can be associated with the voltammetric peaks in figure 4.3:

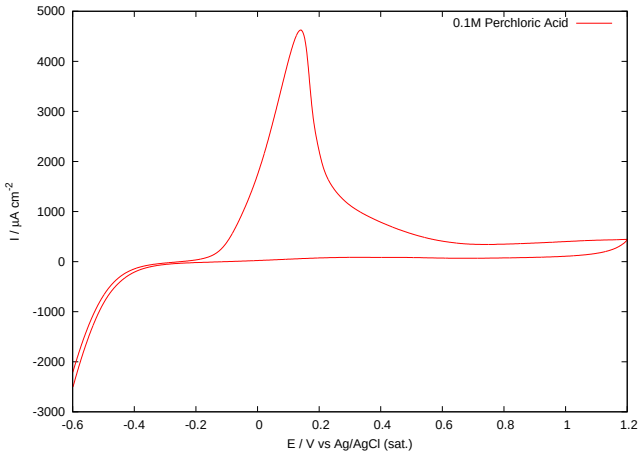

Figure 4.2: Cyclic Voltammetry for Ni in 0.1M $HClO_4$, scan rate 50mVs^{-1}.

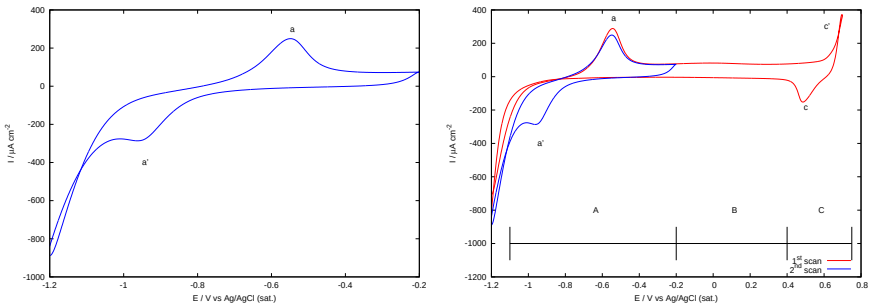

Figure 4.3: Cyclic Voltammetry for Ni in phosphate buffer pH 12.5, scan rate 50mVs^{-1}.

a $\quad H_{\boldsymbol{ads+abs}} \rightarrow H^+ + e^-$
$\quad Ni + 2OH^- \rightarrow \boldsymbol{\alpha}Ni(OH)_{\mathbf{2}} + 2e^-$
c' $\quad \boldsymbol{\beta}Ni(OH)_{\mathbf{2}} + OH^- \rightarrow (\boldsymbol{\beta\gamma})NiOOH + H_{\mathbf{2}}O + e^-$
c $\quad (\boldsymbol{\beta\gamma})NiOOH + H_{\mathbf{2}}O + e^- \rightarrow \boldsymbol{\beta}Ni(OH)_{\mathbf{2}} + OH^-$
a' $\quad$ partially $(\boldsymbol{\alpha,\beta})Ni(OH)_{\mathbf{2}} + 2e^- \rightarrow Ni + 2OH^-$
$\quad H_{\mathbf{2}}O + e^- \rightarrow OH^- + 1/2H_{\mathbf{2}}$

Related to the cyclic voltammetry features three regions can be individuated on the voltammograms: the *hydroxide* or Ni(II) region (A), the transition region (B) and *oxyhydroxide* or the Ni(III) region (C). Since irreversible transition in Ni oxide/hydroxide species takes place at higher potentials,

electrochemical features of nickel electrodes may vary because of previous potential treatments. In the A region the anodic peak a is associated with the formation of $\boldsymbol{\alpha}$-Ni(OH)$_{\mathbf{2}}$ along with the oxidation and expulsion of the absorbed hydrogen in the bulk Ni lattice [81–83]. Peak a' has been assigned to the reduction of $\boldsymbol{\alpha}$-Ni(OH)$_{\mathbf{2}}$ to metallic Ni [84]. This latter peak diminish or disappear [75] after a potential excursion in the B region. It has been proposed that this is due to the dehydration of nickel hydroxyde through the irreversible transformation of $\boldsymbol{\alpha}$-Ni(OH)$_{\mathbf{2}}$ into $\boldsymbol{\beta}$-Ni(OH)$_{\mathbf{2}}$ [75, 85–87]. At more positive potential (region C) the anodic current is related to the further oxide growth and the oxidation of hydroxide phase associated with the formation of Ni(III) species via the reaction indicated previuosly with c'.
In figure 4.4 cyclic voltammograms of Ni in buffers with differents pH are reported. As expected oxidation/reduction peaks of Ni(OH)$_{\mathbf{2}}$ are negatively shifted as the pH of the solution increases and buffers composition does not influence the voltammetric features.

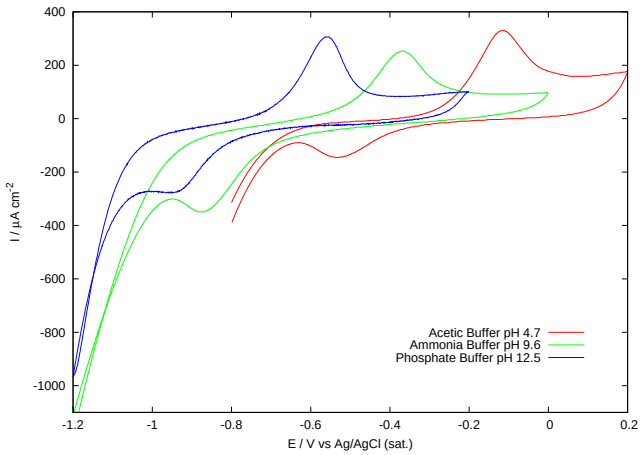

Figure 4.4: Cyclic Voltammetry for Ni in Acetic buffer pH 4.7, Ammonia buffer pH 9.6, Phosphate buffer pH 12.5, NaOH 1M. Scan rate 50mVs^{-1}.

4.1.3 Ni foam electrode

Nickel foam is a metal foam with an open cell structure. Ni foam can be industrially produced by deposition of Ni on a reticulated polymer substrate (usually polyurethane) by electroplating or by Chemical Vapor Deposition.

After metal deposition polymeric matrix is burnt at high temperature and consequently an open-cell skeletal structure of hollow metal limbs is obtained. Several type of Ni-foam are commercially available and they can be classified on density and cell dimension. During the past decades Ni foams have been employed in battery, accumulator electrodes and electrolytic cells. Ni-foams has also been used in alkaline fuel cell as a substrate for pasted nickel electrodes [88–91] or as substrate for metal coated electrode [92–94].

Ni foam electrochemical cell

Experiments on Ni-foam electrodes have been performed using the cell showed in figure 4.5. The cell is a teflon cell specifically designed and manufactured for this purpose. Cell is designed to work in static condition with porous or sheet electrodes with dimension of 30x35mm. Working electrode lay in the middle of the cell between two platinum counter electrodes and is kept in position by two track cut into the cell wall. The top of the working electrode is clamped between two titanium bars. The counter electrodes are at 10mm from the working electrode and are fixed to the cell with two titanium screws. Reference electrode is an Ag/AgCl (sat) electrode placed close to the working electrode to minimize the ohmic drop. The optimal location for the reference electrode was estimated to be in correspondence of the geometrical center of the working electrode; this sandwich-like geometry is employed to maximize the simmetry of the electric field and current distribution in order to obtain an homogeneous deposit on the porous electrode substate. Two teflon gas inlet are fixed on the cell cap. One is long enough to reach the bottom of the cell and can be used for the solution deaeration the other one is kept on the top of the solution in order to prevent oxygen contamination. In fact the cell is not hermetically sealed and its environment can be controlled only mantaining an inside overpressure. Electrochemical characterization of Ni-foam substrates has been conducted in several buffers as shown in figure 4.6. Cyclic voltammetry features do not differs significantly from those observed on Ni flat surfaces.

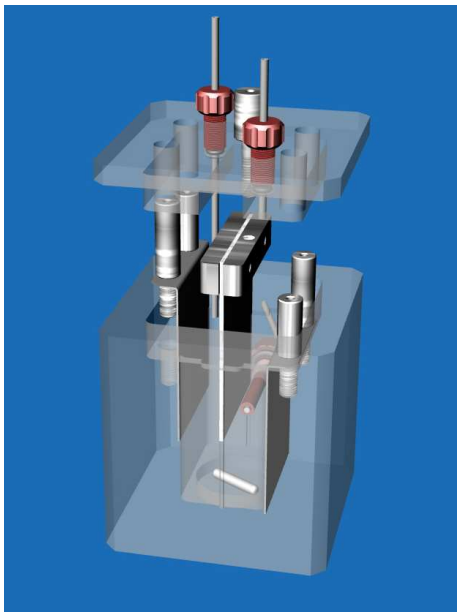

Figure 4.5: Electrocemical Cell designed for the Ni foam electrode characterization

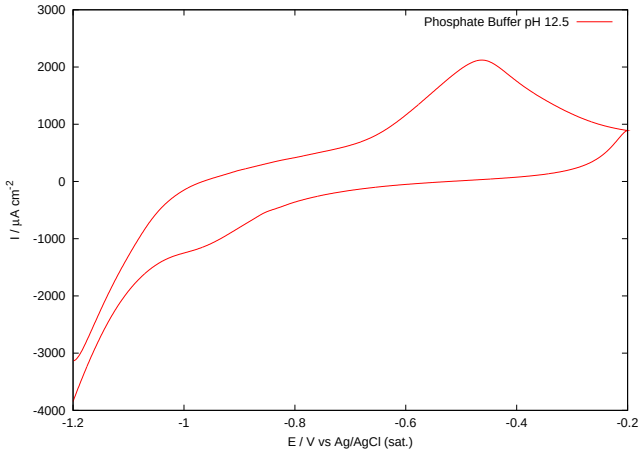

Figure 4.6: Cyclic Voltammetry for Ni-foam substrate in Phosphate buffer pH 12.5. Scan rate 50mVs^{-1}.

4.2 SAM on Nickel electrodes

As described in previous chapter SAMs of noble metals can be easily obtained by liquid-phase self-assembly by simple immersion of the metal substrate in an alkanethiol solution. Most of the papers published on this topic regard Au, Ag, Pt and Cu substrates. Studies on SAM formation on higly reactive metals are rather limited. Stable surface oxide layer prevents the reaction between the S headgroup of the organic molecule with the metal surface. In case of liquid-phase thiol deposition on Ag and Cu substrates exposed to the atmosphere the formation of an oxide layer do not hinder the SAM formation. This is because the alkanethiols molecules can be oxidizied by the metal oxide layer producing a fresh metallic surface which reacts with further alkanethiols molecules present in the solution. On non-noble metals reduction of oxide layer is not possible because of its thickness and stability. Beyond liquid-phase deposition, SAMs can be prepared by vapour-phase self-assembly performed in ultrahigh vacuum (UHV). UHV techniques allow to work on perfectly clean surface in stricly controlled environment but they are usually expensive and time consuming. Morover during the absorption of thiol molecules on Ni surface in UHV conditions the break of C-S bond is observed [95–98], in contrast for SAMs prepared in solution the S-C bond remain intact at room temperature [99–103].
Liquid-phase deposition process on Ni is subject to the possibility of obtaining and handling clean surface in atmosphere and solution. Mekhalif et al. proposed a two step procedure for alkanethiols self-assembly on Ni based on a first electroreduction process followed by immediate substrate immersion in alkanethiols ethanolic solutions [99–103]. In this procedure the metal substrate is briefly exposed to the atmosphere during the transfer from the electrochemical cell to the thiol solution. As fast as the transfer a small amount of oxide may form on the surface preventing a complete deposition of the SAM and affecting the procedure reproducibility. An alternative method based on electrochemical reduction is reported in [104] where SAMs formation is performed under electrochemical control in NaOH 1M aqueous solution of alkanethiols. Electrochemical self-assembly appears as a straightforward route to building stable SAMs on Ni, nevertheless long chain thiols have a low solubility in aqueous media. Solubility of long-chain alkanethios in water depends on solution pH and it is strongly increased at high pH value. Unfortunatly in basic solutions the stability of Ni is limited by hydroxide formation.
Problems related with long-chain alkanethiols solubility and Ni surface oxidation were solved using a non-aqueous media for the SAMs electrode-

position process. Solutions for liquid deposition of alkanethiols SAMs on noble-metal surface are usually prepared with solvents such toluene, hexane, benzene and ethanol. Ethyl alcohol is a suitable choice for the deposition of most thiol molecules and for electrochemical measurements; it is a good compromise between water and non-polar organic solvents. Ethanol it is cheap and non toxic and allows the use of several kind of electrolytes because of its high dipole moment.
Commercial ethanol contains small amounts of water ($<$0.5%) that can be eliminated only after azeotropic distillation and filtration with molecular sieves [105]. Unfortunately ethanol tends to absorb water from the air and the use of water-free solutions in electrochemical experiments it is hard to perform. Formation of hydroxide compunds can be limitated increasing the solution acidity, for this purpose acetic acid was added to the solution to control the pH. Electrochemical deposition was perfomed in Ethanol (99.5%, Fluka), 0.1M Tetramethylammonium chloride (TMACl) as support electrolyte and 1M Acetic Acid. SAM-covered samples were prepared using an electrochemical flow-cell specially designed and manufactured for this purpose (section 4.2.1). Ni electrodes were characterized by cyclic voltammetry in the buffer solution and kept at negative potential to remove surface oxide. After treatment, the deposition potential was applied and a small amount of pure thiol introduced in the electrochemical cell (see section 4.2.2).

4.2.1 Electrochemical Cell for Ni-SAM preparation

In figure 4.7 a scheme of the electrochemical cell used in thiols electrodeposition and electrochemical characterization is reported. Cell is made from a PMMA cylinder, the cylinder was drilled in order to obtain a cylindric cavity for containing the electrolyte. On the cell wall there are seven port for 1/4"-28 flanged tube end fittings which are used for housing gas inlet/outlet tubes, solution inlet/outlet tubes (PTFE, $\varnothing$1/8"), reference and counter electrodes. Working electrode is mounted using a silicon washer on a larger lateral opening (fig. 4.7, A) and hold in position by a M16 titanium screw used also for electrical contact. Solution inlet is located in front of the working electrode, on its left and its right (at 90°) are placed counter and reference electrode (fig. 4.7, B and C). Solution outlet is on the bottom of the cell. Reference electrode is analogue to that described in section 2.3.5, counter electrode is made of a platinum wire. Gas inlet for deaeration is placed on the bottom of the cell and on the top, outlet is placed on the top too (fig. 4.7, G,H and I). An M16 teflon screw close the top opening of the cell. Small amounts of liquid can be added in the cell through the top

cap, removing an 1/4"-28 Peek screw housed in the teflon screw. A manual

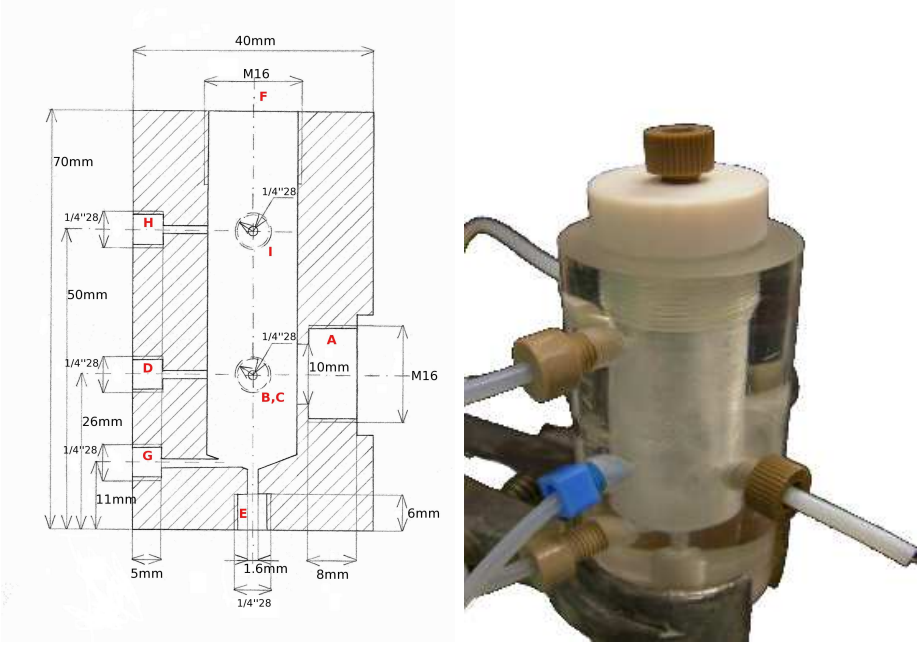

Figure 4.7: Scheme and picture of the electrochemical cell used for SAMs deposition on Ni. A working electrode. B,C reference and counter electrodes. D,E solution inlet and outlet. F top opening. G,H deaeration inlet. I gas outlet.

six-port switching valves system is used to control the solution flow in the electrochemical cell. Solutions are contained in pyrex bottles kept under an overpressure of Nitrogen. Cell solution outlet is controlled by a manual valve connected to a bottle. Gas flows and gas pressure are controlled by pressure regulator and several valves on the gas tubing.

4.2.2 Electrochemical assisted SAM formation

A tipical voltamogram for Ni polycristalline elecrode in 0.1M TMACl, 1M Acetic Acid in Ethanol is shown in figure 4.8. Cathodic current related to hydrogen discharge reaction is visible at negative potentials and at potential closer to 0V a change in the curve slope indicates the onset of Ni oxidation reaction. In the potential range between -0.5V and -1V (or lower) the electrode surface is clean and thiol molecules can react with metal Ni. Monolayers were formed introducing into the electrochemical cell pure thiol

while appling a potential of -0.75V. Thiols were added from the top opening of the cell using a micropipette, the added volume was choosen in order to obtain a 5mM solution. Thiol deposition process was monitored recording a current-time curve.

Electrochemical behaviour of the Ni-thiol system depends on the character-

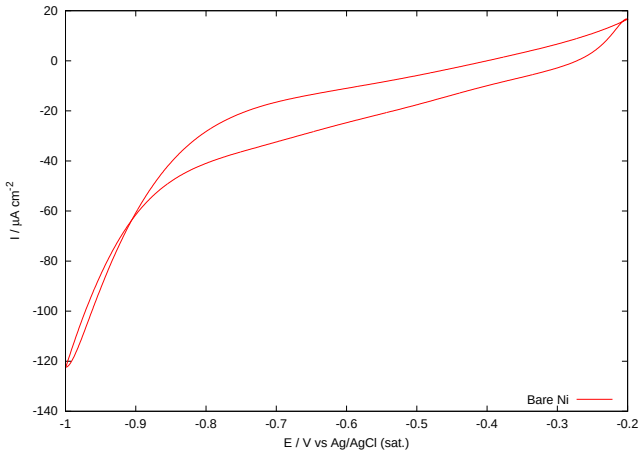

Figure 4.8: Cyclic voltammogram for Ni polycristalline electrode in 0.1M TMACl, 1M Acetic Acid in Ethanol. Scan rate 50mVs^{-1}.

istics of the molecules forming the SAM. Differences of polarity, chain-lenght and acidity in thiol molecules influence the surface oxidation reaction of Ni and its catalytic activity in Hydrogen Evolution Reaction (HER). Three kind of thiol monolayers were studied in this thesis: pure 1-dodecanethiol, pure 3-Mercaptopronic Acid and SAMs obtained from mixed solution of both.

4.2.3 1-DDT SAM on Ni

Current-time curve for 1-DDT deposition process is reported in figure 4.9. At -0.75V a current of about 40μA due to hydrogen discharge is measured. Formation of 1-DDT SAM produces an insulating monolayer hindering the HER. Current starts decreasing immediatly after the addition and in a few minutes is reduced to a value of about 1-5μA. When the current value is stabilized the SAM formation is completed, usually the deposition process is not longer than 20-30 minutes. SAM formation seems to be not affected by HER as current-time curve indicates, which confirms the results obtained

in aqueous solution reported in [104]. Cyclic voltammograms of Ni and Ni modified with 1-DDT in figure 4.10 show a reduced cathodic current for the hydrogen evolution confirming the presence of an insulating monolayer on the electrode surface.

No UPD reaction is known for Ni polycristalline substrate, therefore pres-

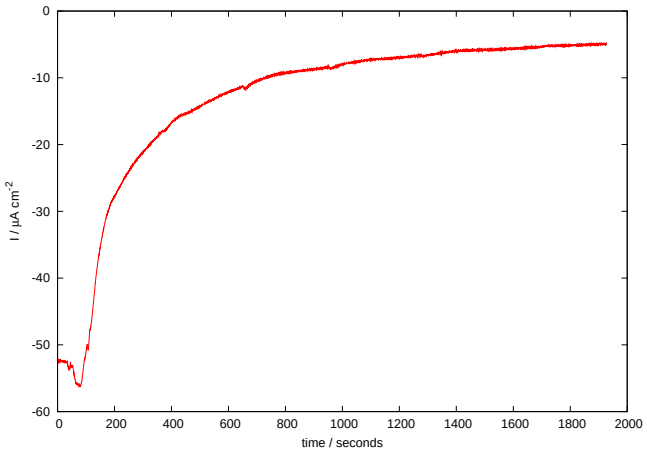

Figure 4.9: Current-time curve for 1-DDT SAM formation in 0.1M TMACl, 1M Acetic Acid in ethanol. Applied potential -0.75V.

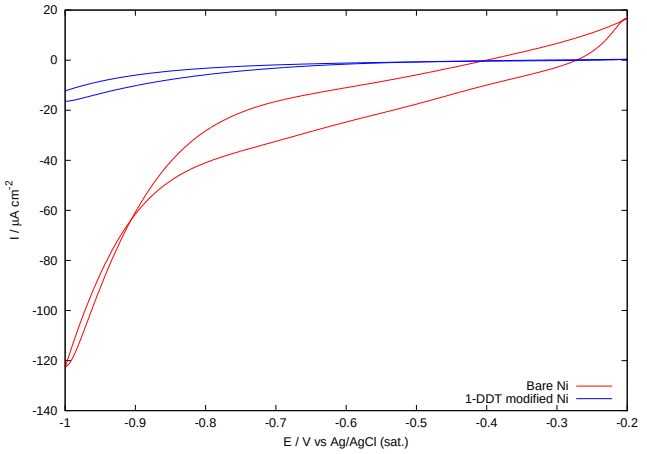

Figure 4.10: Cyclic voltammograms of Ni and Ni modified with 1-DDT in 0.1M TMACl, 1M Acetic Acid in ethanol. Scan rate 50mVs^{-1}.

ence of defects can not be evaluated by UPD adlayer deposition and stripping as done for SAM on Ag(111) (see section 3.3). Nevertheless, as already shown, the compactness of a self-assembled monolayer can be estimated, on the basis of the electron transfer kinetic [68–70], using an electrochemical redox probe. For this purpose the $Ru(NH_3)_6^{2+/3+}$ couple was used. The presence of a compact 1-DDT SAM on the Ni surface was again confirmed as shown by results in figure 4.11.

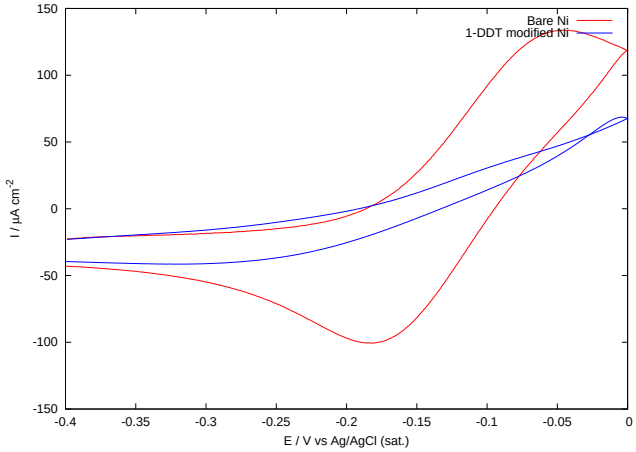

Figure 4.11: Cyclic voltammograms of Ni and Ni modified with 1-DDT obtained from 1mM $Ru(NH_3)_6^{3+}$ in Ammonia buffer pH 9.6. Scan rate $50mVs^{-1}$.

Firmly and densely chemisorbed layer of long chain thiol behave like a protective layer against surface oxidation influencing the Ni oxidation reactions potential in aqueous media. In figure 4.12 cyclic voltammograms for pure and modified Ni electrode in ammonia buffer on an extended range of potential are compare. Ni hydroxide peak at -0.4V is completly missing on SAM covered electrode. In fact the anodic reaction seems to be shifted by almost 900mV at positive potential, however is not clear what reaction is taking place at +0.6V. Ni oxidation potential are strongly related with number of defects in the film. Tests made on SAM formed at different deposition time showed that for fast deposition process the oxidation peak is shifted at less positive potentials. It is worth noting that Ni oxidation can be catalyzed by the presence of sulphur [106] on the electrode surface. In the Ni-SAM system the oxidation process probably starts with thiol desorption and/or oxidation followed by solvent penetration in the film defects. Once the sol-

vent reaches the metal surface the oxidation of the electrode take place. The peak in 4.12 might be analogous to the anodic dissolution peak observed in aqueous acidic solution. XPS was used to eveluate the film quality

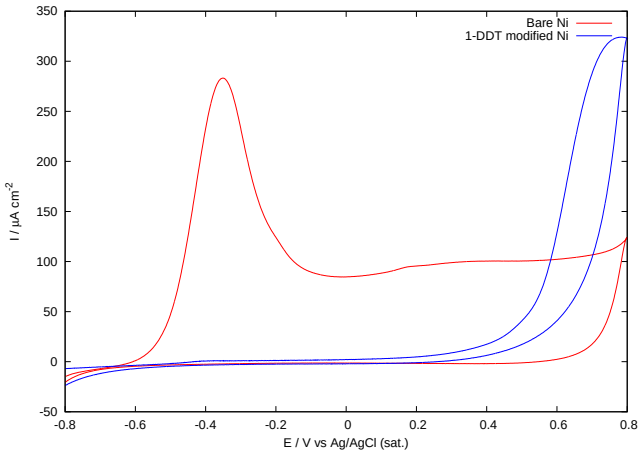

Figure 4.12: Ni electrochemical oxidation. Cyclic voltammograms of Ni and Ni modified with 1-DDT obtained from Ammonia buffer pH 9.6. Scan rate 50mVs^{-1}.

and the efficiency of the procedure developed for SAM formation. Presence of nickel-oxygen compounds and sulphur-oxygen compounds on the surface indicate the presence of defects in the film resulting from an uncomplete surface coverage. XPS allows to characterize the monolayer composition and differentiate between the oxidation states of nickel and sulphur atoms at the interface. The S 2p line is doublet structure composed by S $2p_{3/2}$ and S $2p_{1/2}$ separated by 1.18eV, with intensity ratio S $2p_{3/2}$/S $2p_{1/2}$ of 2. According to literature data to S $2p_{3/2}$ in thiolates (Ni-S-) is assigned a binding energy of 162eV. In non-perfectly formed SAM sulphur compounds contaminants such as thiols (S-H), sulfinates (-SO_2) and sulfonates (-SO_3^-) may be found, binding energies assigned to the S $2p_{3/2}$ peak maximum are respectively 164,167 and 169 eV. Presence of nickel-oxygen compounds is pointed out by shifts in binding energy of the Ni $2p_{3/2}$ peak, which arise at 852.7, 853.8 and 856.6 eV respectively for Ni,NiO and $Ni(OH)_2$ A detailed XPS analysis of 1-DDT electrochemically modified nickel electrode testify the absence of Ni-Oxygen and S-Oxygen species. Ni-thiol bond is a very strong one [104], for this reason any attempt to remove 1-DDT from Ni surface by electrochemical desorption at potential anticipating HER is futile.

Morover hydrogen evolution on surface, which most of the time induces molecules desorption on substrates such as Ag or Au, does not influence SAM formation and stability. XPS analysis on a 1-DDT covered electrode treated at -1.6V (Ag/AgCl sat) in a 0.1M Acetic Acid, 0.1M TMACl in ethanol does not show significant differences from a freshly prepared sample 4.2.3. Electrochemical analysis confirm the same results (figure 4.13)

	Sample 1		Sample 2	
Element	atomic %	Binding Energy (eV)	atomic %	Binding Energy (eV)
Ni	12.89	852.0	10.9	851.9
S	0.66	162.0	1.9	161.7
O	19.33	531.7	28.3	531.3
C	67.12	284.8	58.9	284.8

Table 4.1: Results from XPS analysis on Ni 1-DDT covered electrode. Both samples were prepared with the procedure described above. Sample 1 was analyzed immediatly after surface modification, sample 2 was treated in a 0.1M Acetic Acid, 0.1M TMACl in Ethanol at -1.6V (Ag/AgCl sat) in order to desorb 1-DDT molecules.

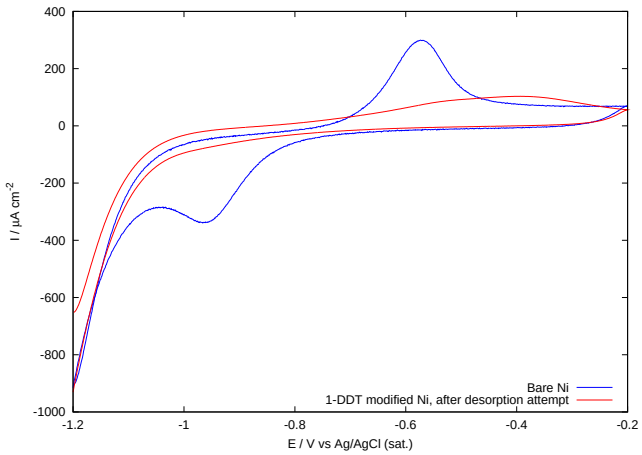

Figure 4.13: Cyclic voltammograms in Phosphate Buffer pH 12.5 of bare Ni and Ni 1-DDT modified electrode after electrochemical treatment at-1.6V (Ag/AgCl sat) in 0.1M Acetic Acid, 0.1M TMACl in Ethanol. Scan rate 50mVs^{-1}.

4.2.4 3-MPA SAM on Ni

Same procedure used for 1-DDT SAM deposition was employed for 3-MPA. Current-time curve recorded after the thiol addition in the electrcochemical cell is reported in figure 4.14, in this case the current due to HER increases before diminishing and stabilizes at a value of about 60μA. This behaviour can be explained considering two aspects of the 3-MPA molecule: the chain lenght and the role of the functional group in promoting hydrogen reduction. 3-MPA chains are not long enough to act as an insulating monolayer: charge

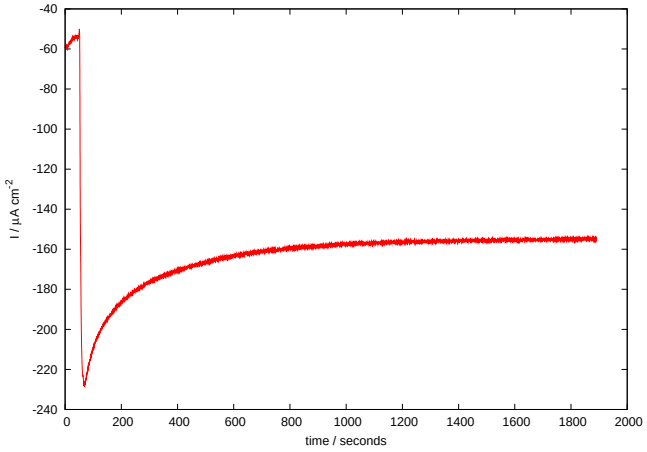

Figure 4.14: Current-time curve for 3-MPA SAM formation in 0.1M TMACl, 1M Acetic Acid in ethanol. Applied potential -0.75V.

transfer may occur by electron tunneling or simply because water molecules penetrate between thiol chains getting enough close to metal surface to oxidize it. It is important to note that the presence of the carboxyl group in the 3-MPA thiol reduce the compactness of the monolayer [4]. Considerations on chain lenght and SAM density can explain why charge transfer is not inhibited but does not justify the increasing of the current. It is well known that HER is promoted in acidic media. 3-MPA is itself acid and its carboxyl group can act as H^+ source shifting the pH to a lower value in the proximity of the electrode surface. 3-MPA catalytic effect on hydrogen reduction may not only be to the increasing of surface acidity but also to the presence of the S-Ni bonding. Several papers [107, 108] report the electrocatalytic activity of Ni-sulphur compounds for HER, the Ni-thiol bonding could facilitate the hydrogen discharge causing an increasing of the current

during the formation of the SAM. The current reaches its maximum when the SAM is not completely formed and than decreases. This could happen because once all the sites on Ni surface are occupied by 3-MPA molecules the penetration of water molecules and ions between the SAM chain is more difficult, consequently the maximum catalytic activity will be observed for electrodes with an incomplete monolayer. Presence of defects in the SAM can't be verified using electrochemical probes as already done for 1-DDT on Ni, in fact the chain lenght of the 3-MPA is too short to hinder charge transfer. Consequently the comparison between cyclic voltammograms of clean and covered Ni in presence of a redox probe such $Ru(NH_3)_6^{2+/3+}$ does not give any information about the monolayer compactness.
The presence of 3-MPA influences the electrode reactivity at negative potential in an opposite way respect to 1-DDT. In correspondance of the Ni hydroxide formation peak a large anodic peak is observed as shown in figure 4.15. The area of the anodic peak for a Ni-modified electrode is almost ten times bigger than for clean Ni substrate, the electrochemical process involved in the charge transfer can not be associated with hydroxide formation (which should be limited to one or few monolayers). Two different phenomena can

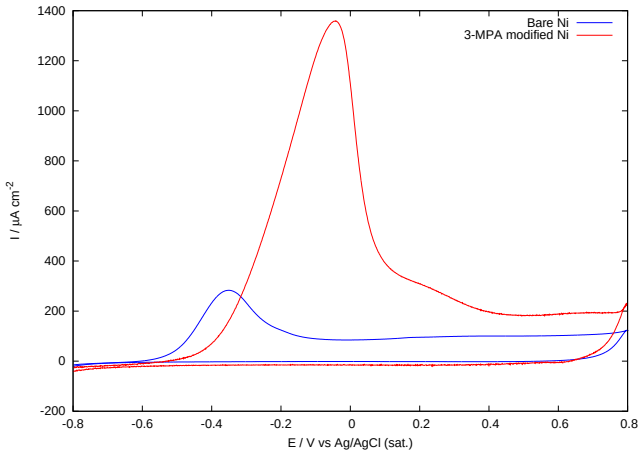

Figure 4.15: Cyclic voltammograms for clean and 3-MPA modified Ni electrodes in ammonia buffer pH 9.6. Scan rate $50 mVs^{-1}$

explain this behaviour: hydrogen desorption and Ni oxidation.

- Hydrogen absorption in bulk Ni is widely documented; besides, several studies on hydrogen storage report that Ni-Sulphur compounds

have a great capacity of absorbing electrochemically generated hydrogen [109]. This interpretation is supported by data reported in figure 4.16 where cyclic voltammograms for Ni modified electrodes collected after appling HER potential for different times are shown. The relation between the increasing of peak area and the treatment time could indicate that the anodic peak is due to desorption of hydrogen absorbed at HER potential.

- Ni oxidation is catalyzed by the presence of sulphur at the surface [106], for this reason thiols bound to the surface could somehow facilitate the Ni dissolution preventing the hydroxide formation. Nevertheless the carboxyl group must play a role in the Ni oxidation reaction because the same experiment conduced on a Ni electrode modified with ethanthiol does not show any increase in peak area after a negative potential treatment (fig. 4.17).

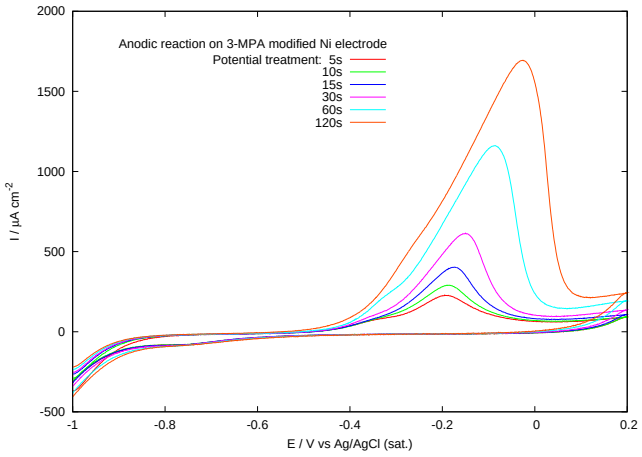

Figure 4.16: Cyclic voltammograms for 3-MPA modified Ni electrodes in ammonia buffer pH 9.6, after electrode treatment at -1.0V for different times. Scan rate $50 mVs^{-1}$

XPS experiments conducted on freshly prepared sample state the absence of thiols, sulfinates, sulfonates, Ni-Oxygen compounds, confirming the reproducibility of the preparation method using different thiol molecules. Samples after treatment at positive potential (+0.2V Ag/AgCl sat) in ammonia buffer were also analyzed. No traces of Ni-oxygen compounds were found on Ni surface, which confirms that the anodic process could be originated by

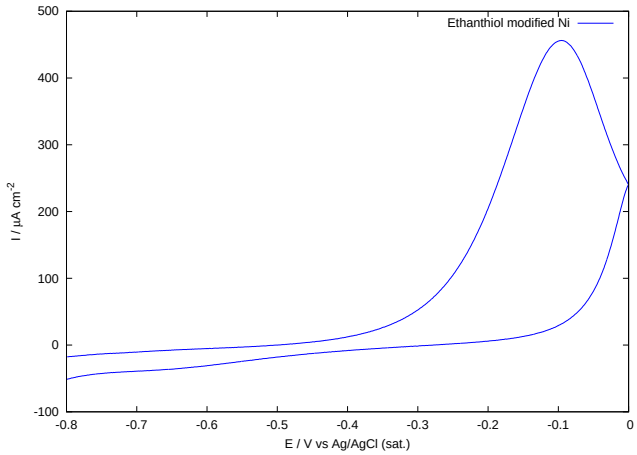

Figure 4.17: Cyclic voltammograms for Ethanthiol modified Ni electrodes in ammonia buffer pH 9.6. Scan rate 50mVs^{-1}

hydrogen desorption or Ni dissolution. Comparing to data obtained from an 1-DDT covered electrode no relevant differences could be found in Ni and S species 4.2.4.

	1-DDT		3-MPA	
Element	atomic %	Binding Energy (eV)	atomic %	Binding Energy (eV)
Ni	11.8	852.0	64.8	852.0
S	0.80	161.9	0.6	161.7
O (oxides)	1.2	529.1	1.7	531.3
O (CO_3^{2-}, -COO^-)	16.6	531.5	4.5	531.6
C (alyphatic)	65.9	284.8	21.8	285.0
C (carboxyl)	-	-	3.4	288.6

Table 4.2: Results from XPS analysis on Ni 1-DDT and 3-MPA covered electrode. Both samples were prepared treating the electrode at 0.2V (Ag/AgCl sat) in Ammonia Buffer for 10 minutes.

4.2.5 Binary SAM on Ni

Binary SAM of 3-MPA and 1-DDT were deposited using the same electrochemical assisted procedure, in this case a solution of the two thiols was

added in the cell in order to reach the concetration of 0.3mM of 1-DDT and 0.3mM of 3-MPA. Current-time curve has a shape similar to the 3-MPA curve but a lower current involved in the process. Comparison of cyclic voltammograms is reported in figure 4.18, as expected voltametric features differ from what observed previously for fully 1-DDT and 3-MPA covered electrodes.

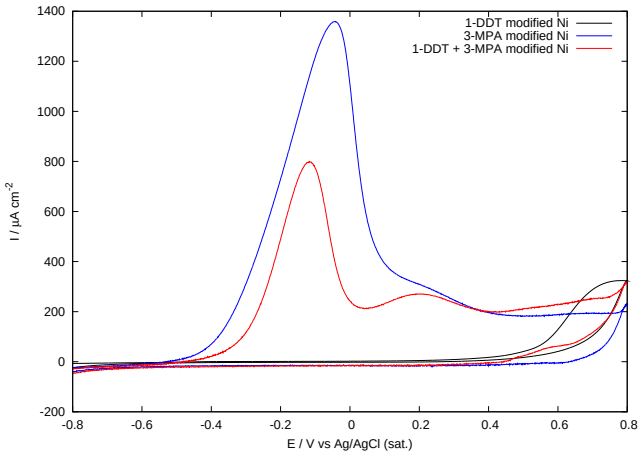

Figure 4.18: Comparison of cyclic voltammograms for various Ni modified electrodes. Media: ammonia buffer pH 9.6, scan rate 50mVs^{-1}

4.3 Pd thin films

Pd exhibits high electrocatalytic activity in alkaline electrolyte to the ethanol oxidation reaction. Recently the possibility of replacing Pt in Direct Ethanol Fuel Cells (DEFCs) with cheaper metals, such as palladium, has attracted interest of numerous research groups [110–114]. Electrocatalytic materials for Direct Alcohol Fuel Cells (DAFCs) can be prepared in several ways. In order to maximize the *apparent* electrocatalytic effect, Pd-based catalysts are often prepared in form of nanoparticles [110, 112, 115] by synthetic methods or by electrodeposition in form of nanostructured thin films [113]. Electrodeposition is a powerful technique for the deposition of many metals since it is rapid, cheap and facile, allowing easy control of the nucleation and growth of metal nanoparticles and nanowire. Moreover nanoparticles have to be deposited on conductive substrates to be used as electrodic material while electrodeposited thin films are ready for use. Electrodeposition allows to solve problems related to the nanoparticles dispersion stability and to reduce reactants waste. Palladium is a noble metal belonging to Platinum group metal. Like other noble metal Pd is relatively inert to chemical attack by oxygen and many acids. The principal oxidation state of Pd is +2, altough exist a number of complexes of Pd^{4+}. Pd^{2+} has a d^8 electronic structure and tends to form stable square planar complexes. Standard potentials for Pd^{2+} electroreduction occurs at 0.915V(SHE), which means that if Pd^{2+} solutions are brought in contact with metallic Ni the spontaneous deposition of Pd and the consequent oxidation of Ni are observed. In electroplating industry bath containing Pd complexes are usually employed to prevent uncontrolled deposition. Pd chemical reactivity is not the only problem in Pd electrodeposition. As matter of facts Pd has the capacity to absorb hydrogen much as 900 times its volume. The ability of Pd to absorb hydrogen poses a significant problem for the electrodeposition of this metal from aqueous solution. Hydrogen absorption during the electrodeposition process is the cause of a variety of fracture in the Pd film. This phenomen, known as hydrogen embrittlement problem, is widely investigated because of its importance in industrial electroplating and hydrogen storage [116, 117]. Best conditions for Pd growth are obtained when the electrodeposition take place at potentials between the HER and Ni oxidation. Pd forms very stable complexes with ammonia and amines; for this reason and beause of the Ni electrochemistry, the choice of using alkaline electrolytes for the electrodeposition process was the more promising. Two methodology were employed for Pd electrodeposition. The first one employs 1,3-diaminopropane (1,3pn) and operates in potentiodinamic conditions at potentials anticipating the

hydrogen discharge but more negative than Ni hydroxide formation. In the second one Pd is electrodeposited from ammonia complexes in potentiastatic conditions at more positive potentials.

4.3.1 Potentiodynamic electrodeposition

1,3pn is a bidentate ligand, whose formula is $NH_2C_3H_6NH_2$, that forms a square planar coordination complex with Pd, $[Pd(1,3pn)_2]^{2+}$. Stability of the complex is very high and a shift of about 1.7V respect to the standard conditions is observed for the Pd^{2+} reduction potential. In figure 4.19 cyclic voltammograms relative to $Pd(1,3pn)_2^{2+}$ electrodeposition in alkaline media are shown. The choice of basic electrolyte allows to shift the HER at more negative potential, thus performing electrodeposition without hydrogen interferences in a potential range where Ni surface is unoxidized. Pd films

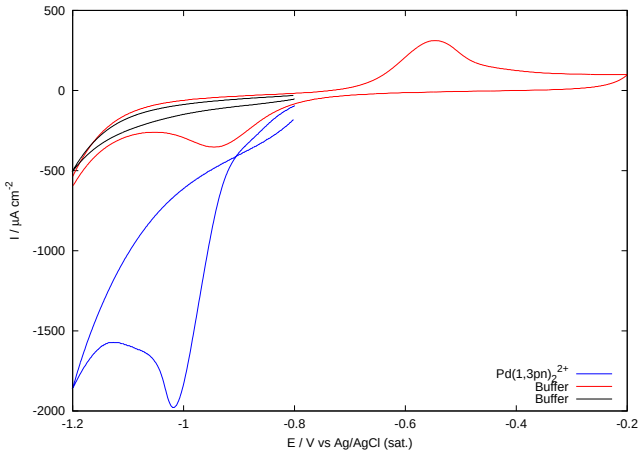

Figure 4.19: Cyclic voltammograms for Ni in 1mM $Pd(1,3pn)_2^{2+}$ in phosphate buffer pH 12.5. Pd electrodeposition occurs between HER and Ni hydroxide formation. Scan rate $50mVs^{-1}$

were electrodeposited on Ni surface at constant current using a potentiodynamic method developed for this purpose. The electrodeposition process is controlled by a LabView program which, adjusting the applied potential (trough a potentiostat), keeps the deposition current at constant value. A flow chart of the algorithm is shown in figure 4.3.1. The amount of deposited Pd is controlled integrating the current. Once the charge transferred during the process reaches the set value the deposition is stopped. This is done

removing the Pd solution from the flow cell by washing with buffer solution and applying a rest potential. The process was used for current up to 100μA starting at potential of -0.75V. Morphological analysis conducted by AFM

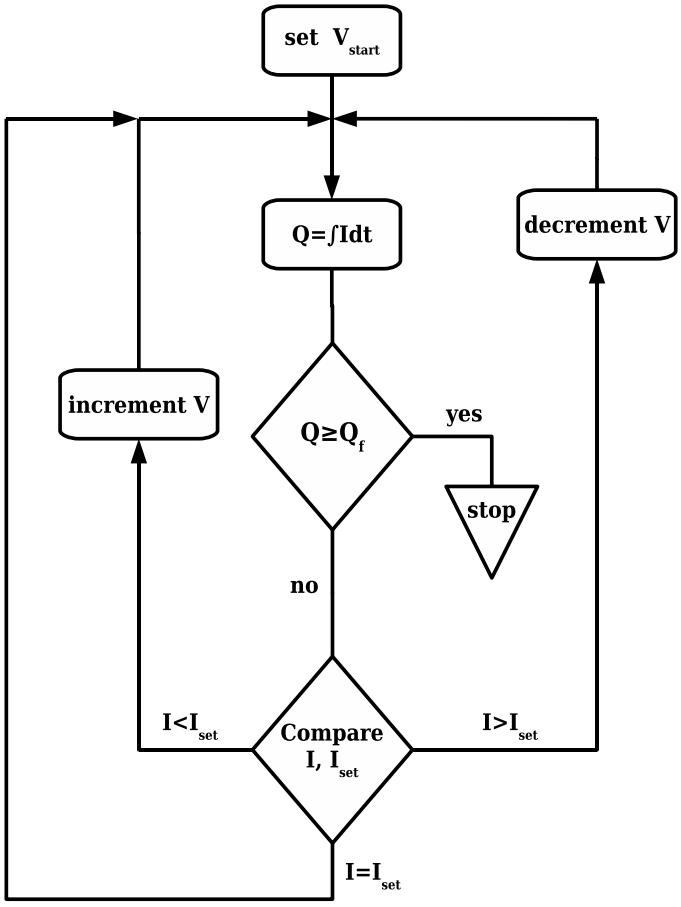

Figure 4.20: Flow chart of the LabView program used in potentiodinamic electrodeposition.

reveals the presence of Pd clusters with size of about 100nm or less. As result of electrodeposition process the RMS surface roughness increase from 1.6 to 5.8nm (figure 4.21). Presence of Pd on nickel surface is confirmed by electrochemical measures. In figure 4.22 the cyclic voltammograms in phos-

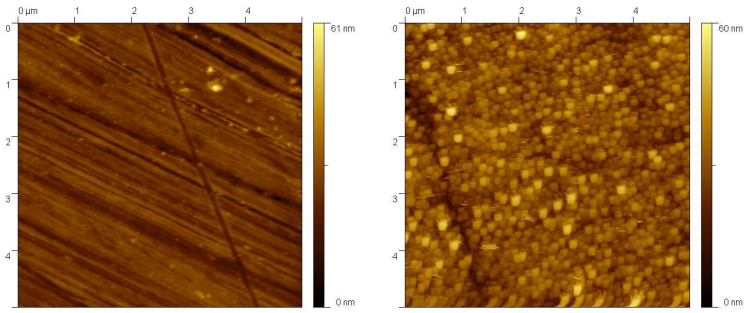

Figure 4.21: AFM images of polished Ni surface (left) and Pd covered Ni surface. Electrodeposition was performed at a constant current of 100μA for 240s on a Ni polished surface of 0.41cm$^{\mathbf{2}}$

phate buffer shows the characteristic features of Pd in alkaline media. The anodic peak at -0.8V is due to hydrogen desorption from Pd bulk. Height, shape and size of this peak change with amount of absorbed and adsorbed hydrogen which depend on the time the electrode is kept at HER potential. Cathodic peak at -0.2V is the reduction of Pd oxide formed at 0.4V [118]. Catalytic activity for ethanol oxidation was investigated by cyclic voltammetry in a 2M KOH 10wt% ethanol. A comparison between Pd-Ni film and Pd bulk electrode is reported in figure 4.23.

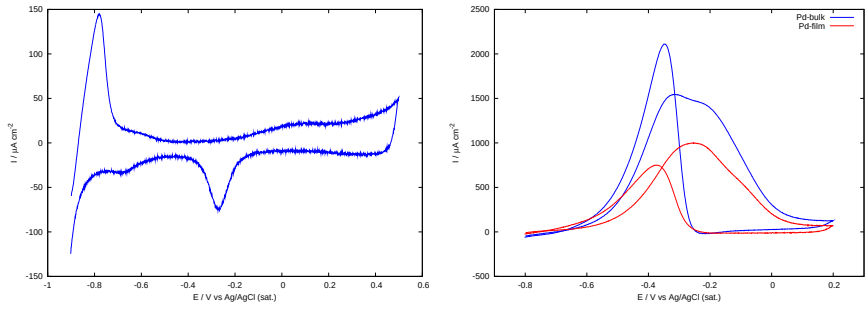

Figure 4.22: Left: Cyclic voltammogram for Pd thin film on Ni in phosphate buffer pH 12.5. Scan rate 50mVs$^{-\mathbf{1}}$

Figure 4.23: Right: Cyclic voltammogram for Pd thin film on Ni in 2M KOH 10wt% ethanol and Pd bulk electrode. Scan rate 50mVs$^{-\mathbf{1}}$

4.3.2 Potentiostatic electrodeposition

Electrodeposition can be simply controlled applying a potential exceeding the redox potential of the species and waiting for an amount of time necessary to deposit the desired amount of material. Assuming a flat deposit the film thickness is calculated by the charge transferred integrating the current-time curve of the electrodeposition process. This methodology allows the deposition of very small amount of material when a slow electrodeposition process occurs. Deposition rate is usually strongly reduced if using stable Pd complexes. In case of $Pd(1,3pn)_{\mathbf{2}}^{\mathbf{2+}}$ the complex can be used as a source of $Pd^{\mathbf{2+}}$ in solution; in fact, even if with a large stability constant, the complex tend to dissociate and if a potential close to the redox potential is applied this happens faster. Applying a potential of -0.75V (Ag/AgCl sat), which nominally preceeds the reduction potential of $Pd(1,3pn)_{\mathbf{2}}^{\mathbf{2+}}$, and keeping it constant for several minutes, a current due to Pd reduction is measured. This method was used for Pd electrodeposition on Ni electrodes covered with binary SAM and is discussed in section 4.3.3.
Using less stable complexes (such $Pd(NH_{\mathbf{3}})_{\mathbf{4}}^{\mathbf{2+}}$) electrodeposition was also performed at potentials where the Ni surface is covered with oxide and hydroxide compounds. In this conditions the Pd adlayers do not adhere strongly to the substrate (lattice mismatch is too large) and grows in nano or micro clusters leading to an increase of surface roughness. Cyclic voltammograms for $Pd(NH_{\mathbf{3}})_{\mathbf{4}}^{\mathbf{2+}}$ are reported in figure 4.24; the differences between the first and the second scan are due to the different kind of interactions between Pd adlayers with Ni and Pd substrates. Pd and Ni have a certain affinity as demonstrated by the capability to form alloys, anyway voltammograms prove that Pd-Pd interactions are significantly stronger than Pd-Ni interactions. During the electrodeposition process in potentiostatic conditions the effects of Pd-Pd and Pd-Ni interactions will cause a shift of the deposition potential as the Pd surface coverage increases, leading to the increase of the current and the deposition rate. Electrodeposition is performed switching the potential from potentials where the electrodeposition do not occur (-0.2V) to deposition potential. Current is integrated in time and when the charge reach the desired value the potential is again switched to the initial rest potential. The current-time curve for Pd $Pd(NH_{\mathbf{3}})_{\mathbf{4}}^{\mathbf{2+}}$ growth at -0.45V (Ag/AgCl sat) is reported in figure 4.25, its shape is coherent with a nucleation and growth mechanism for the Pd film. The electrodeposition experiment was repeated several time increasing the deposited charge. AFM analysis of the surface showed palladium deposits near scratchs and steps of the electrode surface forming, for higher amount of deposited material, a

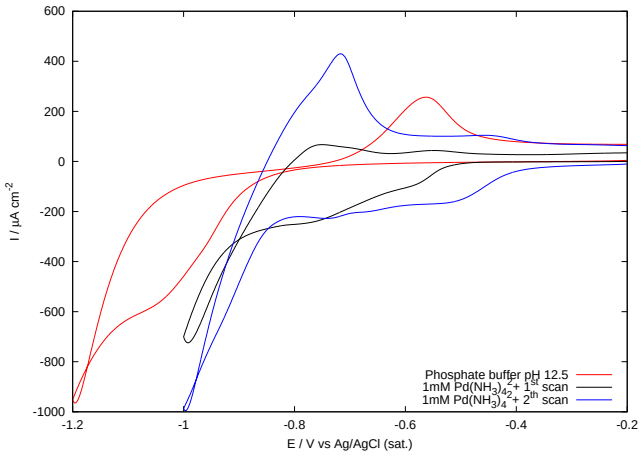

Figure 4.24: Pd-Pd interactions are stronger than Pd-Ni interactions. Electrodeposition on Ni take place at more negative potentials than on Ni/Pd surface as shown in cyclic voltammograms for Ni in 1mM $Pd(NH_3)_4^{2+}$ in phosphate buffer pH 12.5. Scan rate $50mVs^{-1}$.

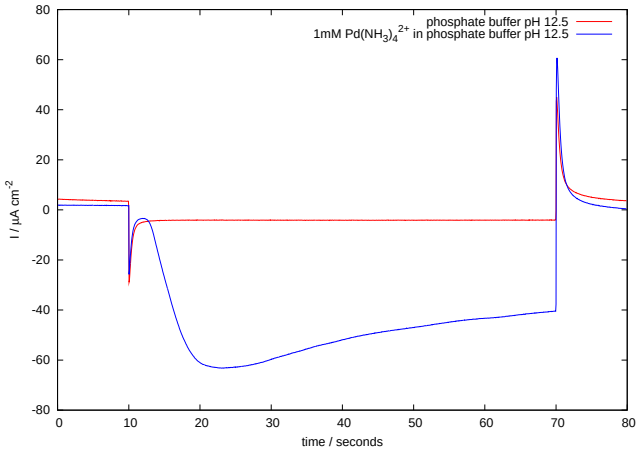

Figure 4.25: Pd electrodeposition on Ni polished electrode. Current-time curves in buffer and 1mM $[Pd(NH_3)_4]Cl_2$. Electrodeposition potential: -0.45V (Ag/AgCl sat), electrolyte: phosphate buffer pH 12.5.

rough surface covered with small size clusters (fig. 4.26). If small amounts of Pd are deposited (the charge equivalent to ten monolayers or less) the presence of Ni on the surface can be still detected by cyclic voltammograms

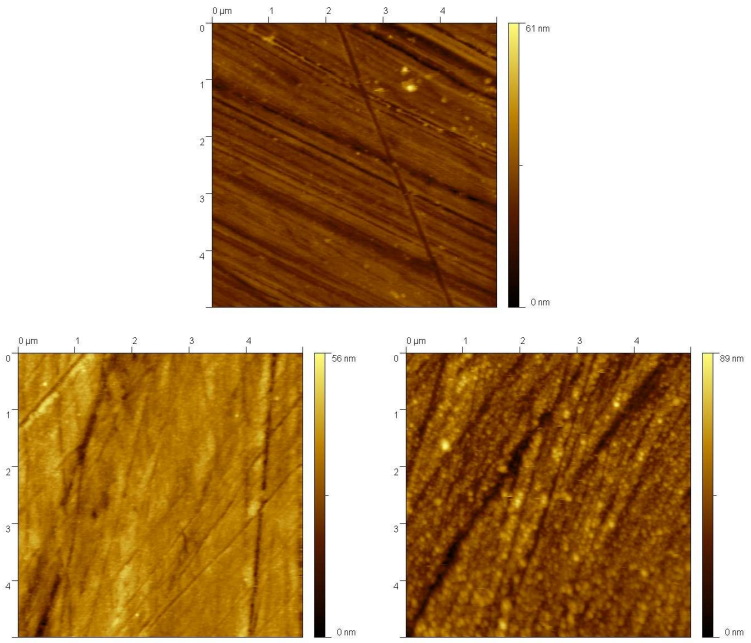

Figure 4.26: AFM images of polished Ni surface (top) and Pd covered Ni surface. Electrodeposition was performed at -0.75V (Ag/AgCl sat.) from 1mM $Pd(1,3pn)_{\mathbf{2}}^{\mathbf{2+}}$ in phosphate buffer pH 12.5 for 20s (left) and 180s (right).

(figure 4.27) meaning that a non-uniform film is formed. The result is in agreement with the hypothesis made on the basis of morphological data. Electrocatalytic activity of Pd-Ni surface was tested for various degree of coverage in order to verify the possible sinergetic activity of Pd and Ni hydroxide/oxide compounds in ethanol oxidation. By data presented in figure we may safely conclude that the Ni substrate is not directly involved in ethanol oxidation in alkaline media. Referring to the forward scan in figure 4.29 the electrocatalytic activity seems to be straightly dependent upon the amount of deposited Pd, nevertheless the oxidation peaks in the reverse scans show an unexpected behaviour. Catalytic activity seems to be increased in electrodes with a lower Pd coverage, no exaustive explanations could be found to elucidate this phenomen which is probably related with the surface oxidation/reduction process occuring at positive potentials.

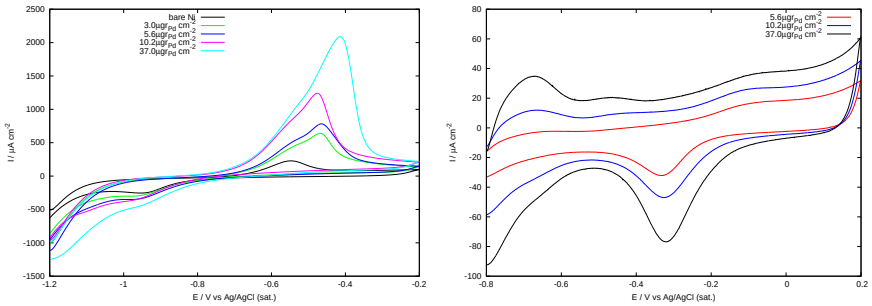

Figure 4.27: Left: Ni hydroxide reduction peak is still visible for low coverage of Pd. For higher Pd coverage the Ni reduction peak disappear and the amount of desorbed hydrogen increases (anodic peak)

Figure 4.28: Right: Cyclc voltammetry for different Pd-Ni syistems in 2M KOH. Electrochemical active area and amount of Pd are proportional with the Pd oxide reduction peak. Scan rate 50mVs^{-1}.

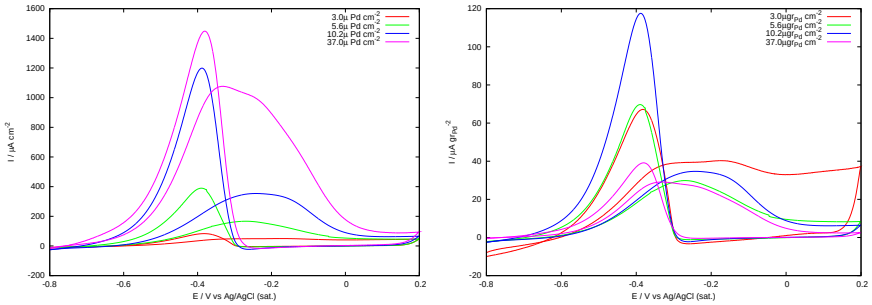

Figure 4.29: Pd film electrocatalytic activity, electrode are prepared by potentiostatic deposition on Ni at -0.45V(Ag/AgCl sat). In the right plot current is normalized for the Pd loading as used [110], experiments have been performed on electrode with the same surface areas. Cyclic voltammograms are obtained in 2M KOH and 10wt% Ethanol. Scan rate 50mVs^{-1}

Electrodeposition on Ni foam

The potentiostatic deposition technique described above for Ni flat electrodes was used for electrodeposition on Ni-foam. In figure 4.30 the current-time electrodeposition curve is reported. Cyclic voltammograms in phosphate buffer pH 12.5 (fig. 4.31) indicate the presence of a uniform Pd film covering completly the Ni surface, no oxidation/reduction peaks of the Ni substrate are visible. Curves reported in figure 4.32 evidence the role of the

electrochemical active area in the electrocatalysis of ethanol oxidation. Data have been collected for a Pd thin film deposited on Ni foam and on a Ni flat sheet using the same electrochemical cell. The current density for ethanol oxidation on Ni foam at lower potentials (operating conditions in DEFCs) reaches values three times higher than on Ni sheet. The behaviour can be explained considering that the ratio between the electrochemical active area and the geometrical area is higher for Ni foam.

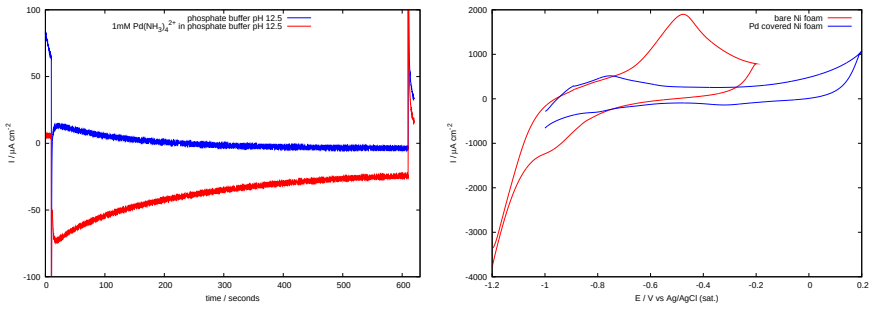

Figure 4.30: Left: Pd electrodeposition on Ni foam. Current-time curves in buffer and 1mM $[Pd(NH_3)_4]Cl_2$. Electrodeposition potential: -0.45V (Ag/AgCl sat), electrolyte: phosphate buffer pH 12.5.

Figure 4.31: Right: Cyclic voltammograms of bare Ni foam and Pd covered Ni foam electrodes in phosphate buffer pH 12.5. Scan for Ni-Pd electrode starts at potential higher than -1V to avoid hydrogen absorption/desorption phenomena. Scan rate $50mVs^{-1}$

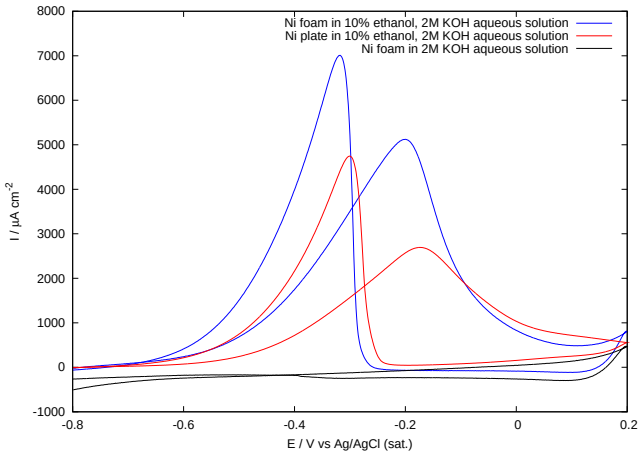

Figure 4.32: Pd-Ni foam electrocatalytic activity. Cyclic voltammograms of Ni-Pd foam electrode in 2M KOH and in 2M KOH 10wt% Ethanol. Scan rate 50mVs^{-1}

4.3.3 Electrodeposition on SAM modified Ni electrode

Phase segregation in binary SAMs has been already extensively discussed in previuos chapter. While for SAMs on Au [119] and Ag [120] thiol molecules can be selectively removed by electrodesorption at negative potential, this procedure is not applicable on Ni [104]. For this reasons the use of 1-DDT/3-MPA SAMs as template for metal/compound electrodeposition as already done on Ag substrates can not be employed for electrodeposition process on Ni. Moreover the ratio of thiols absorbed can not be determined by electrochemical desorption and in LFM images there are not enough evidences to establish if phase segregation phenomena occur on Ni surface. Altough it is reasonable to think that some kind of segregation phenomen occurs on the Ni surface. Differences in the electrochemical reactivity between SAM of 1-DDT and 3-MPA were pointed out in section 4.2.5, where it was observed that short-chain thiols are less protective againts Ni electrochemical oxidation than long-chain thiols. For the same reasons SAMs can act as a protective layer agaist electrodeposition reaction. Hence in presence of segregated SAM nucleation and growth will be strongly affected upon modification of the electrode. Phenomenologically, deposition of a metal on a SAM modified surface is described to occur in three different ways [121]:

- intercalation at the SAM/substrate interface

- deposition originating at the substrate with subsequent mushroom-like growth
- deposition on top of the SAM resulting in a metal-SAM-metal sandwich structure

In any case the electrodeposition process starts with Pd reduction on the 3-MPA covered zone and proceedes covering the whole electrode surface. This growth mechanism leads to the deposition of Pd film with an increased surface roughness. Reduction of $Pd(1,3pn)_2^{2+}$ on Ni modified elecrode was investigated by voltammetric methods. The presence of thiols bound on Ni surface induces a negative shift in Pd reduction peak. More precisely, the Pd electrodeposition process on Ni occurs at more negative potentials on electrodes modified with more insulating molecules, following the trend (Ni)>(1-MPA/Ni)>(1-DDT/Ni), as shown in figure 4.33. Long-chain thiols

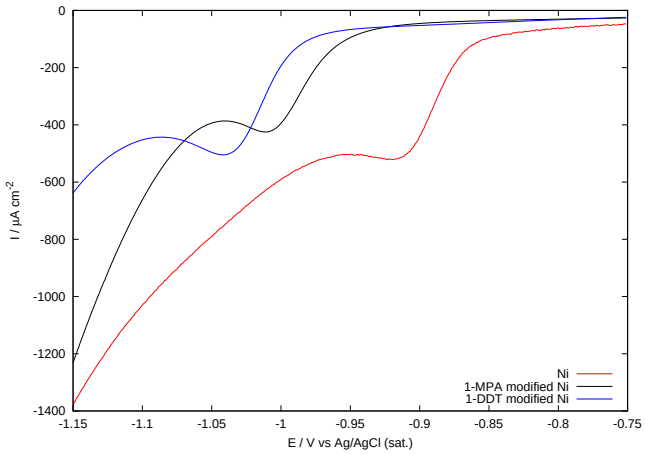

Figure 4.33: Linear sweep voltammetry in 1mM $Pd(1,3pn)_2^{2+}$, phosphate buffer pH 12.5 for Ni and Ni modified electrodes.

SAMs are not enough insulating to prevent Pd electrodeposition at all, nevertheless SAM presence shift significantly the reduction potential. Attempts of Pd potentiostatic electrodeposition (see 4.3.2) on Ni modified surface are reported in figure 4.34. In these conditions 1-DDT SAMs on Ni are completly insulating while a cathodic current is measured on 3-MPA covered Ni electrodes despite voltammetry does not indicate any reduction reaction in that potential range. Presence of Pd on Ni/3-MPA electrodes is easily detected by cyclic volatmmetry (fig. 4.36). A lack of stability in 3-MPA SAMs

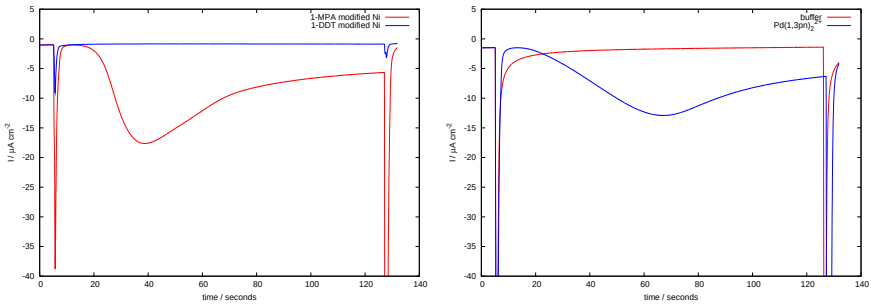

Figure 4.34: Left: Pd electrodeposition on Ni modified electrodes. 1-DDT acts as an insulator on Ni preventing Pd deposition while on 3-MPA modified electrode Pd reduction occurs. Current-time curves in 1mM $[Pd(1,3pn)_2^{2+}]$. Electrodeposition potential -0.75V (Ag/AgCl sat), electrolyte: phosphate buffer pH 12.5.

Figure 4.35: Right: Pd electrodeposition on binary SAM modified Ni electrode. Current-time curves in buffer and 1mM $[Pd(1,3pn)_2^{2+}]$. Electrodeposition potential -0.75V (Ag/AgCl sat), electrolyte: phosphate buffer pH 12.5.

was already pointed out in previous voltammetric experiments, therefore the Pd deposition does not surprise. Tentatively, we can assume that Pd starts nucleating on SAM defects and than continue intercalating between SAM and Ni or with a mushroom like growth. The formation of a sandwich-like structure might be possible but is usually considered less probable. It is worth noting that the formation of thiols film on Pd is impossible at the deposition potential, hence in case of intercalating growth the thiols will be quickly desorbed from the electrode surface. In case of deposition on binary SAM the current-time curve (figure 4.35) shows that the deposition process has a lower growth rate respect to deposition on Ni/3-MPA electrode, which is compatible with the presence of areas covered with an insulating SAM of 1-DDT. As a consequence of an increase of the surface area a moderate increase in the electrocatalytic activity of the Pd thin film is observed. Better results might be obtained if porous or high surface area substrates, such as Ni foam, were used.AFM analysis reveals significant differences in size and distribution of Pd clusters on Ni and Ni/SAM electrode surfaces. AFM images of polished Ni electrodes (fig. 4.38), Pd thin films on Ni (fig. 4.39) and on SAM modified Ni (fig. 4.40) evidence against that Pd electrodeposition process leads to an increase of the surface roughness of polished Ni electrodes. This phenomen is remarkably increased when electrodeposition

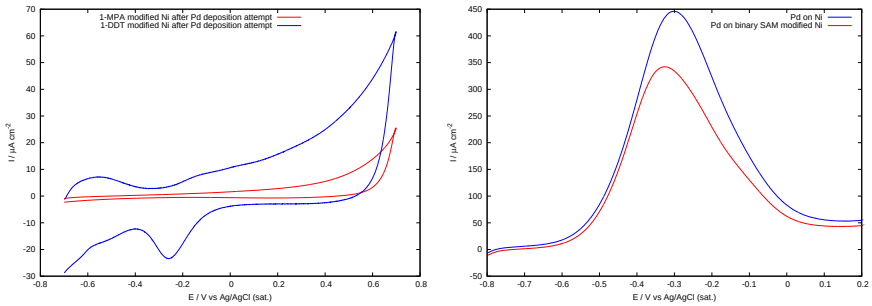

Figure 4.36: SAM modified Ni electrode after Pd electrodeposition, presence of Pd is evaluated by cyclic voltammetry verifying the presence of Pd oxide reduction peak. On Ni electrode modified with 3-MPA Pd features are clearly visible while on 1-DDT modified electrode only Ni oxidation peak is visible. Electrolyte: phosphate buffer pH 12.5, scan rate 50mVs^{-1}

Figure 4.37: Electrocatalytic activity of Pd films deposited on bare Ni and binary SAM modified Ni electrode. Linear sweep voltammetry in 2M KOH 10wt% Ethanol, scan rate 50mVs^{-1}

is performed on Ni electrodes modified with binary SAMs, in this conditions Pd clusters on Ni/SAM surface are four times higher than on clean Ni surface. This effect leads to an increase of the RMS roughness values which are: RMS$_{\boldsymbol{Ni}}$=2.1nm, RMS$_{\boldsymbol{Ni/Pd}}$=3.8nm and RMS$_{\boldsymbol{Ni/SAM/Pd}}$=18.3nm. Results of the morphological analysis are coherent with the hypotesis on Pd growth mechanism described above. In fact if Pd deposition starts first in areas covered by short-chain thiols, the Pd clusters nucleated in these areas will be higher than on the remaining surface. The direct consequence of this nucleation and growth mechanism is an increase of the surface roughness.

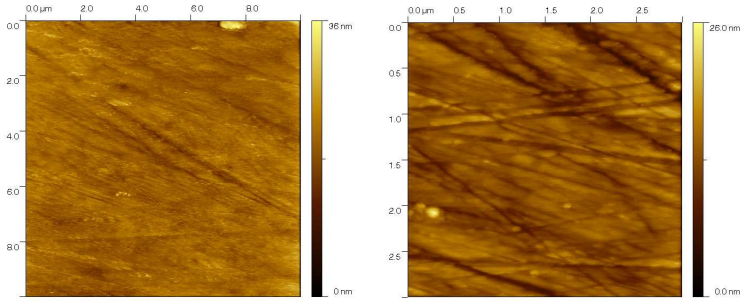

Figure 4.38: Polished Ni surface. AFM images.

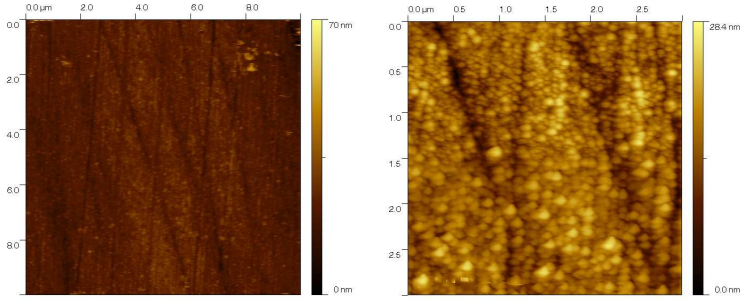

Figure 4.39: AFM images of Pd covered Ni elecrode. Pd electrodeposited at -0.75V (Ag/AgCl sat.) for 120s from 1mM $Pd(1,3pn)_2^{2+}$ in phosphate buffer pH 12.5.

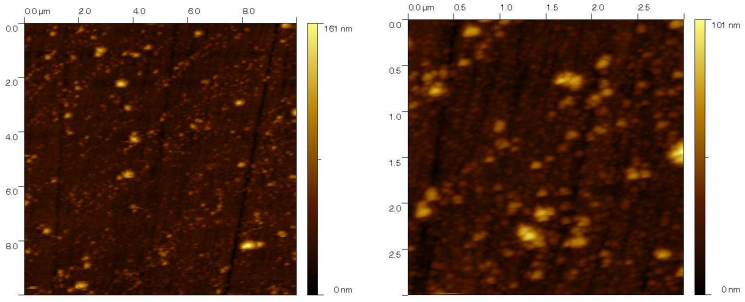

Figure 4.40: AFM images of Pd covered Ni elecrode modified with a binary SAM of 3-MPA and 1-DDT. Pd electrodeposited at -0.75V (Ag/AgCl sat.) for 120s from 1mM $Pd(1,3pn)_2^{2+}$ in phosphate buffer pH 12.5.

Conclusion

The aim of this work was to investigate a novel methodology in electrodeposition at nanometor scale.

The first part of the work was dedicated to the growth of CdS thin films on silver single crystals by the Electrochemical Atomic Layer Epitaxy methodology, which is based on the alternate electrodeposition of monoatomic layers. The method exploits underpotential deposition phenomena to limitate the electrodeposition to a single monolayer of an element at a potential anticipating the Nernst potential. Alternating underpotential deposition cycles of different elements a thin films of controlled thickness and composition is grown. The use of single crystals as substrate for electrodeposition increases the probability for epitaxial growth, since the ordered electrodeposition of an atomic layer depends on the order of the substrate surface. Thus, the crystallinity of the substrate is at least partially transferred to the compound during the growth. The effects of the substrate lattice on the structure of the thin film were investigated for the first stages of the growth by in-situ STM and electrochemical techniques. In-situ STM experiments allowed to measure the lattice parameter of the sulphur adlayer on Ag(110) and Ag(100) at various potential and to correlate voltammetric features with the sulphur adlayer structures. Structural characterization of the CdS thin films was carried out by Surface X-ray Diffraction at the European Synchroton Radiation Facility of Grenoble. Diffraction experiments revealed a strong influence of the substrate structure on film order. Indeed, the wurtzite structure was found on Ag(100), while on Ag(110) the contemporary presence of two CdS allotropic structure (wurtzite and zincblende) was observed. Comparing diffraction data with the results of the x-ray reflectivity analysis it is clear that at least on Ag(100) the thin film is crystalline along the direction perpendicular to the surface.

The second part of the work was directed to the realization of templates for the electrodeposition at a nanometric or submicrometric scale on Ag(111) electrodes. Templates were obtained exploiting the phase segregation phenomena occuring in binary self assembled monolayers. Since long-chain SAM act as insulators on the electrode surface, confined electrodeposition can be achieved through the use of a surface properly patterned by Self Assembled Monolayer. Self-assembled monolayers composed of two different alkanethiols having different chain lengths exhibit phase separation at the nanometer scale; this phenomen lead to the auto-organization of pattern of different molecules on the surface. Since the desorption potential is progressively more negative the longer the alkanethiol chain, the application of a suitable potential allows the selective desorption of the short-chain thiol. Formation of binary self assembled monolayers of alkanethiols with different chain lenght in different conditions was studied by electrochemical techniques and AFM, in order to find a relation between the domain distribution and the depostion conditions. Cadmium sulfide was succesfully electrodeposited on SAM patterned silver surface after the electrochemical desorption of a component of a binary SAM. This method was developed with the purpose of using it in the future for the electrodeposition of islands of metals able to exert synergetic electrocalalytic effects.

The last part of the work was focused on the study of model Ni-Pd electrocatalysts. Pd is well known for its capacity to promote the electrochemical oxidation of several alcohols in alkaline media. Its catalytic activity and its reduced cost with respect to the most commonly used catalysts, such Pt, make Pd a suitable material for the preparation of electrocatalysts for Direct Ethanol Fuel Cell anodes. The possibility of controlling electrodeposition of Pd thin films on Ni polycristalline substrates was investigated. Since self-limited electrochemical reactions, such as underpotential deposition, for the deposition of noble metals on Ni are not known, different methods were developed for the electrodeposition of controlled amount of Pd. Pd-Ni electrodes with different morphology and roughness were obtained. Since the electrocatalytic activity of a material is strongly related with its surface area (the so called *apparent electrocatalytic effect*) a complete morphological characterization of the Pd thin films was conducted by AFM. AFM analysis was followed by electrochemical characterization of the catalytic activity of the material for the oxidation of ethanol in alkaline media. The realization of thiol templates on Ni electrode for the electrodeposition of Pd was also studied. Preparation of Self Assembled Monolayer of thiols on Ni surface is a

poorly investigated topic, for this reason a novel method for electrochemical assisted SAM formation was developed and succesfully tested for the realization of Pd catalysts for ethanol oxidation. Beyond the applications of thiol template for Pd electrodeposition the thiol-Ni system was studied by X-ray photoelectron spectroscopy and electrochemical techniques. Even if further investigations are needed for the complete understanding of the role of thiol molecules on Ni electrochemistry, interesting effects on Ni surface oxidation and on the possible presence of hydrogen absorption/desorption phenomena at Ni surface are reported.

Appendix A

Experimental details chapter 3

section 3.1

Materials

Merck Suprapure NaOH and Aldrich analytical reagent grade Na_2S were used without further purification. The water used was obtained from spring water by distilling it once and then distilling it again using alkaline permanganate while constantly discarding the heads. The solution was freshly prepared because aged sulfide solutions yielded in situ STM images of polysulfide chains on Ag that were not observed when using freshly prepared solutions. Ag single crystals were prepared according to the procedure described in page 24, terraces of sufficiently large size were obtained by annealing the crystals in an inert gas atmosphere at 500°C.

STM experiments

Topograpic images 512x512 pixels are obtained with constant-current mode and without further filtration, unless otherwise indicated in the caption. Experimental conditions like tunneling current and bias voltage are given in the captions; positive bias voltages indicate that the tip is positive with respect to the sample. Tips preparation and experimental setup are described in section 2.3.2.

section 3.2

Materials

For the electrochemical growth we used, without any further purification, Merck analytical reagent grade $3CdSO_4 \cdot 8H_2O$, Fluka analytical reagent grade Na_2S and Merck analytical reagent grade KClO4. Moreover, double distilled water, Merck analytical reagent grade HClO4 (65%) and NH4OH (33%) were used to prepare solutions of $3CdSO_4 \cdot 8H_2O$ 5mM and Na_2S 0.5mM in pH 9.6 ammonia buffer. The solutions were freshly prepared just before the beginning of each series of measurements. Silver single crystals were prepared as described previously (section 2.3.6, page 24).

Surface X-ray diffraction and X-ray reflectivity

The experiments were carried out at the ID03 beamline of the European Synchrotron Radiation Facility (ESRF) in Grenoble (see section 2.3.4). SXRD and XRR measurements were performed on a six circle diffractometer in vertical geometry. Samples were mounted on the diffractometer stage enclosed in a mylar bag filled with nitrogen to prevent surface damage by oxygen and ozone. X-ray energy was chosen to be 12.4keV corresponding to a wavelength 1.00Å. Intesities of the CdS (00$\boldsymbol{l}$) specular rod were corrected considering the illuminated surface area, the polarization of the incident beam and the Lorentz factor. Modeling and simulation of the CdS (00$\boldsymbol{l}$) CTRs are described in the next section. Reflectivity curves were fitted using the software PARRAT32 [122], a general purpose program developed at the HMI Institute of Berlin. The code is based on the Parrat formalism [123] and includes a roughness factor in the fitting parameter calculated according to Nevot and Croce [124].

section 3.3

Materials

Merck analytical reagent grade $3CdSO_4 8H_2O$ and absolute ethanol, Aldrich analytical reagent grade Na_2S, KCl, NaOH, $Ru(NH_3)_6Cl_3$ and purity grade Fluka 90% 3-MPA, OT, DT, and 1-DDT, were used without further purification. Merck analytical reagent grade $HClO_4$ (65%) and NH_4OH (33%) were used to prepare the pH 9.2 ammonia buffer.

Self-Assembly of Alkanethiols on Ag(111)

The silver single crystals were prepared and cleaned according to the procedure described in section 2.3.6 (page 24). For the attainment of a full layer formation, the substrate was immersed in solutions of alkanethiol in pure ethanol for at least 2 h. The single SAMs were obtained from 0.3 mM alkanethiol solutions, whereas the mixed SAMs were prepared from solutions of different compositions to realize different monolayer compositions. Simultaneous adsorption of the mixed SAM was performed by immersing the silver substrate in a 99.8% ethanol solution containing the thiols. The systematic investigation was carried out using solutions containing different thiol concentrations.

ECALE electrodeposition

CdS growth was obtained by alternating the underpotential deposition of sulfur with that of Cd and repeating this basic cycle as many times as desired to attain the wanted thickness. The details for CdS ECALE deposition as well as the substrate conditioning have already been reported [33, 51, 54, 72, 73].

Appendix B

Experimental details chapter 4

sections 4.1, 4.2 and 4.3

Materials

Merck analytical reagent grade absolute ethanol, Aldrich analytical reagent grade TMACl, NaOH, $Ru(NH_3)_6Cl_3$ and purity grade Fluka 90% 3-MPA, Ethanthiol and 1-DDT, were used without further purification. Merck analytical reagent grade $HClO_4$ (65%) and NH_4OH (33%) were used to prepare the pH 9.2 ammonia buffer. Aldrich analytical reagent K_2HPO_4 and NaOH grade were used for phosphate buffer at pH 12.5. Fluka analytical reagent grade Acetic Acid and Aldrich NaOH were used for Acetic buffer pH 4.7 preparation.

Self-Assembly of Alkanethiols on Ni

Electrochemical assisted SAM formation was performed in the cell described in section 4.2.1. Measured volumes of pure thiols were introduced through the upper cap using a micropipette. Volume of the solution inside the cell was controlled and kept constant using volume marks on the cell wall. Oxygen contamination was prevented increasing the nitrogen overpressure in cell during the add.

Pd electrodeposition

For Pd electrodeposition $Pd(NH_3)_4Cl_2$ 99.9% from Alfa Aesar was used. Complexes with 1,3pn were prepared adding Fluka 1,3-diaminopropane 95% to $Pd(NH_3)_4Cl_2$ solutions in order to obtain a concentration of 1,3pn ten times higher than Pd concentration.

Ni foam electrochemical cell

Ni foam electrodes were cleaned as described in section 2.3.6. Before each measurement the Ni foam electrochemical cell was deaerated for ten minutes with nitrogen. During the experiment the cell is constantly kept under an over pressure of nitrogen to avoid oxygen contamination.

Bibliography

[1] D. M. Kolb, "Physical and electrochemical properties of metal monolayers on metallic substrates," in *Advances in Electrochemistry and Electrochemical Engineering* (H. Gerischer and C. W. Tobias, eds.), vol. 11, pp. 125–271, New York: Wiley, 1978.

[2] J. C. Love, L. A. Estroff, J. K. Kriebel, R. G. Nuzzo, and G. M. Whitesides, "Self-assembled monolayers of thiolates on metals as a form of nanotechnology," *Chemical Reviews*, vol. 105, no. 4, pp. 1103–1170, 2005.

[3] D. G. Castner and B. D. Ratner, "Biomedical surface science: Foundations to frontiers," *Surface Science*, vol. 500, no. 1-3, pp. 28 – 60, 2002.

[4] A. Ulman, *An Introduction to Ultrathin Organic Films*. ACADEMIC PRESS, 1991.

[5] F. Schreiber, "Structure and growth of self-assembling monolayers," *Progress in Surface Science*, vol. 65, no. 5-8, pp. 151 – 257, 2000.

[6] F. Schreiber, "Self-assembled monolayers: from 'simple' model systems to biofunctionalized interfaces," *Journal of Physics: Condensed Matter*, vol. 16, no. 28, p. R881, 2004.

[7] G. M. Whitesides and B. Grzybowski, "Self-Assembly at All Scales," *Science*, vol. 295, no. 5564, pp. 2418–2421, 2002.

[8] B. D. Gates, Q. Xu, M. Stewart, D. Ryan, C. G. Willson, and G. M. Whitesides, "New approaches to nanofabrication: molding, printing, and other techniques," *Chemical Reviews*, vol. 105, no. 4, pp. 1171–1196, 2005. PMID: 15826012.

[9] A. P. Alivisatos, P. F. Barbara, A. W. Castleman, J. Chang, D. A. Dixon, M. L. Klein, G. L. McLendon, J. S. Miller, M. A. Ratner, P. J. Rossky, S. I. Stupp, and M. E. Thompson, "From molecules to materials: Current trends and future directions," *Advanced Materials*, vol. 10, no. 16, pp. 1297–1336, 1998.

[10] A. Aviram and M. Ratner, *Molecular Electronics: Science and Technology*. New York: N.Y. Acad. Sci., 1998.

[11] D. G. Kurth, P. Lehmann, D. Volkmer, A. Mller, and D. Schwahn, "Biologically inspired polyoxometalate-surfactant composite materials. investigations on the structures of discrete, surfactantencapsulated clusters, monolayers, and langmuir-blodgett films of (doda)," *Journal of the Chemical Society, Dalton Transactions*, no. 21, pp. 3989–3998, 2000.

[12] J. Pflaum, G. Bracco, F. Schreiber, R. Colorado Jr., O. E. Shmakova, T. R. Lee, G. Scoles, and A. Kahn, "Structure and electronic properties of alkanethiol monolayers on au(1 1 1): A scanning tunneling microscopy, surface x-ray and helium scattering study," *Surface Science*, vol. 498, no. 1-2, pp. 89–104, 2002.

[13] C. D. Bain, E. B. Troughton, Y. . Tao, J. Evall, G. M. Whitesides, and R. G. Nuzzo, "Formation of monolayer films by the spontaneous assembly of organic thiols from solution onto gold," *Journal of the American Chemical Society*, vol. 111, no. 1, pp. 321–335, 1989.

[14] D. I. Gittins, D. Bethell, D. J. Schiffrin, and R. J. Nichols, "A nanometre-scale electronic switch consisting of a metal cluster and redox-addressable groups," *Nature*, vol. 408, no. 6808, pp. 67–69, 2000.

[15] A. Lio, D. H. Charych, and M. Salmeron, "Comparative atomic force microscopy study of the chain length dependence of frictional properties of alkanethiols on gold and alkylsilanes on mica," *Journal of Physical Chemistry B*, vol. 101, no. 19, pp. 3800–3805, 1997.

[16] P. L. Schilardi, P. Dip, P. C. Dos Santos Claro, G. A. Benitez, M. H. Fonticelli, O. Azzaroni, and R. C. Salvarezza, "Electrochemical deposition onto self-assembled monolayers: New insights into micro- and nanofabrication," *Chemistry A European Journal*, vol. 12, no. 1, pp. 38–49, 2000.

[17] O. Azzaroni, M. Cipollone, M. E. Vela, and R. C. Salvarezza, "Protective properties of dodecanethiol layers on copper surfaces: The effect of chloride anions in aqueous environments," *Langmuir*, vol. 17, no. 5, pp. 1483–1487, 2001. Cited By (since 1996): 29.

[18] G. Brunoro, A. Frignani, A. Colledan, and C. Chiavari, "Organic films for protection of copper and bronze against acid rain corrosion," *Corrosion Science*, vol. 45, no. 10, pp. 2219–2231, 2003. Cited By (since 1996): 17.

[19] F. Zucchi, V. Grassi, A. Frignani, and G. Trabanelli, "Inhibition of copper corrosion by silane coatings," *Corrosion Science*, vol. 46, no. 11, pp. 2853–2865, 2004. Cited By (since 1996): 26.

[20] S. Trasatti, "Principles of electrocatalisys," in *Advances in Electrochemistry and Electrochemical Engineering* (H. Gerisher and C. Tobias, eds.), vol. 2, pp. 1–85, New York: VCH, 1990.

[21] E. Guerrini and S. Trasatti, "Recent developments in understanding factors of electrocatalysis," *Russian Journal of electrochemistry*, vol. 42, no. 10, pp. 1017–1025, 2006.

[22] G. Binnig, H. Rohrer, C. Gerber, and E. Weibel, "Surface studies by scanning tunneling microscopy," *Phys. Rev. Lett.*, vol. 49, pp. 57–61, Jul 1982.

[23] G. Binnig and H. Rohrer, "In touch with atoms," *Rev. Mod. Phys.*, vol. 71, pp. S324–S330, Mar 1999.

[24] B. Warren, *Modern Aspects of Electrochemistry*. New York: Dover Publications Inc., 1990.

[25] A. Guinier, *Modern Aspects of Electrochemistry*. New York: Dover Publications Inc., 1994.

[26] I. Robinson and D. Tweet, "Surface x-ray diffraction," *Reports on Progress in Physics*, vol. 55, p. 599, 1992.

[27] R. Feidenhans'l, "Surface structure determination by x-ray diffraction," *Surface Science Reports*, vol. 10, p. 105, 1989.

[28] M. L. Foresti, A. Pozzi, M. Innocenti, G. Pezzatini, F. Loglio, E. Salvietti, A. Giusti, F. D'Anca, R. Felici, and F. Borgatti, "In situ x-ray

analysis under controlled potential conditions: An innovative setup and its application to the investigation of ultrathin films electrodeposited on ag(111)," *Electrochimica Acta*, vol. 51, no. 25, pp. 5532 – 5539, 2006.

[29] M. L. Foresti, F. Capolupo, M. Innocenti, and F. Loglio, "Visual detection of crystallographic orientations of face-centered cubic single crystals," *Crystal Growth and Design*, vol. 2, no. 1, pp. 73–77, 2002.

[30] A. Hamelin, "Modern aspects of electrochemistry," in *Advances in Electrochemistry and Electrochemical Engineering* (R. W. B.E. Conway and J. Bockris, eds.), vol. 16, p. 1, New York: Plenum Press, 1985.

[31] T. Kurasawa, "Patent japan 35:5619," 1960.

[32] T. Cecconi, A. Atrei, U. Bardi, F. Forni, M. Innocenti, F. Loglio, M. L. Foresti, and G. Rovida, "X-ray photoelectron diffraction (xpd) study of the atomic structure of the ultrathin cds phase deposited on ag(111) by electrochemical atomic layer epitaxy (ecale)," *Journal of Electron Spectroscopy and Related Phenomena*, vol. 114-116, pp. 563–568, 2001.

[33] M. Innocenti, S. Cattarin, M. Cavallini, F. Loglio, and M. L. Foresti, "Characterisation of thin films of cds deposited on ag(111) by ecale. a morphological and photoelectrochemical investigation," *Journal of Electroanalytical Chemistry*, vol. 532, no. 1-2, pp. 219–225, 2002.

[34] G. D. Aloisi, M. Cavallini, M. Innocenti, M. L. Foresti, G. Pezzatini, and R. Guidelli, "In situ stm and electrochemical investigation of sulfur oxidative underpotential deposition on ag(111)," *The Journal of Physical Chemistry B*, vol. 101, no. 24, pp. 4774–4780, 1997.

[35] G. Rovida and F. Pratesi, "Sulfur overlayers on the low-index faces of silver," *Surface Science*, vol. 104, no. 2-3, pp. 609 – 624, 1981.

[36] M. Yu, D. P. Woodruff, C. J. Satterley, R. G. Jones, and V. R. Dhanak, "Structural investigation of the interaction of molecular sulfur with ag(111)," *The Journal of Physical Chemistry C*, vol. 111, no. 7, pp. 3152–3162, 2007.

[37] M. Cavallini, M. Bracali, G. Aloisi, and R. Guidelli, "Electrochemical stm investigation of 1,8-octanedithiol self-assembled monolayers on

ag(111) in aqueous solution," *Langmuir*, vol. 15, no. 8, pp. 3003–3006, 1999.

[38] L.-J. Wan, S. Shundo, J. Inukai, and K. Itaya, "Ordered adlayers of organic molecules on sulfur-modified au(111): in situ scanning tunneling microscopy study," *Langmuir*, vol. 16, no. 5, pp. 2164–2168, 2000.

[39] D. W. Hatchett and H. S. White, "Electrochemistry of sulfur adlayers on the low-index faces of silver," *The Journal of Physical Chemistry*, vol. 100, no. 23, pp. 9854–9859, 1996.

[40] D. W. Hatchett, X. Gao, S. W. Catron, and H. S. White, "Electrochemistry of sulfur adlayers on ag(111). evidence for a concentration- and potential-dependent surface-phase transition," *The Journal of Physical Chemistry*, vol. 100, no. 1, pp. 331–338, 1996.

[41] M. Schweizer and D. M. Kolb, "First observation of an ordered sulfate adlayer on ag single crystal electrodes," *Surface Science*, vol. 544, no. 1, pp. 93 – 102, 2003.

[42] M. Schweizer and D. M. Kolb, "Electrochemical and structure studies of ethanethiol self-assembled monolayers on ag single crystal electrodes," *Journal of Electroanalytical Chemistry*, vol. 564, pp. 85 – 91, 2004. Special issue in honour of Rolando Guidelli on the occasion of his 65th birthday.

[43] M. D. Lay, K. Varazo, and J. L. Stickney, "Formation of sulfur atomic layers on gold from aqueous solutions of sulfide and thiosulfate: studies using ec-stm, uhv-ec, and tlec," *Langmuir*, vol. 19, no. 20, pp. 8416–8427, 2003.

[44] C. Schlaup, D. Friebel, P. Broekmann, and K. Wandelt, "Potential dependent adlayer structures of a sulfur-covered au(111) electrode in alkaline solution: An in situ stm study," *Surface Science*, vol. 602, no. 4, pp. 864 – 870, 2008.

[45] A. Spnig, P. Broekmann, and K. Wandelt, "Atomic structure of adsorbed sulfide on cu(111) in acidic solution: In situ stm studies," *Electrochimica Acta*, vol. 50, no. 21, pp. 4289 – 4296, 2005. Electrified Interfaces - Selection of Papers from The 10th International Conference (ICEI 2004) 11-16 July 2004, Spa, Belguim.

[46] A. Spaenig, P. Broekmann, and K. Wandelt, "Structure of electrochemically deposited sulfide layers on cu(100)," *Zeitschrift fur Physikalische Chemie*, vol. 217, no. 5, pp. 459–477, 2003. Cited By (since 1996): 6.

[47] U. Demir and C. Shannon, "Reconstruction of cadmium sulfide monolayers on au(100)," *Langmuir*, vol. 12, no. 2, pp. 594–596, 1996.

[48] O. M. Magnussen, "Ordered anion adlayers on metal electrode surfaces," *Chemical Reviews*, vol. 102, no. 3, pp. 679–726, 2002.

[49] M. Innocenti, M. L. Foresti, A. Fernandez, F. Forni, and R. Guidelli, "Kinetics of two-dimensional phase transitions of sulfide and halide ions on ag(111)," *The Journal of Physical Chemistry B*, vol. 102, no. 48, pp. 9667–9676, 1998.

[50] M. L. Foresti, M. Innocenti, F. Forni, and R. Guidelli, "Electrosorption valency and partial charge transfer in halide and sulfide adsorption on ag(111)," *Langmuir*, vol. 14, no. 24, pp. 7008–7016, 1998.

[51] M. Innocenti, G. Pezzatini, F. Forni, and M. L. Foresti, "Cds and zns deposition on ag(111) by electrochemical atomic layer epitaxy," *Journal of the Electrochemical Society*, vol. 148, no. 5, pp. 357–362, 2001.

[52] G. Valette, "Inner-layer capacity at the pzc for perfect (111), (100) and (100) faces of silver : Surface area and capacitance contributions of superficial defects for real electrodes," *Journal of Electroanalytical Chemistry*, vol. 224, no. 1-2, pp. 285 – 294, 1987.

[53] M. S. Maestre, R. Rodrguez-Amaro, E. Muoz, J. J. Ruiz, and L. Camacho, "Use of cyclic voltammetry for studying two-dimensional phase transitions: Behaviour at low scan rates," *Journal of Electroanalytical Chemistry*, vol. 373, no. 1-2, pp. 31 – 37, 1994.

[54] M. L. Foresti, G. Pezzatini, M. Cavallini, G. Aloisi, M. Innocenti, and R. Guidelli, "Electrochemical atomic layer epitaxy deposition of cds on ag(111): An electrochemical and stm investigation," *Journal of Physical Chemistry B*, vol. 102, no. 38, pp. 7413–7420, 1998.

[55] E. Lastraioli, F. Loglio, M. Cavallini, F. Simeone, M. Innocenti, F. Carla, and M. L. Foresti, "In situ scanning tunneling microscopy

investigation of sulfur oxidative underpotential deposition on ag(100) and ag(110)," *Langmuir*, vol. 26, no. 22, pp. 17679–17685, 2010.

[56] C. D. Bain and G. M. Whitesides, "Molecular-level control over surface order in self-assembled monolayer films of thiols on gold," *Science*, vol. 240, no. 4848, pp. 62–63, 1988.

[57] P. E. Laibinis, R. G. Nuzzo, and G. M. Whitesides, "Structure of monolayers formed by coadsorption of two n-alkanethiols of different chain lengths on gold and its relation to wetting," *Journal of Physical Chemistry*, vol. 96, no. 12, pp. 5097–5105, 1992.

[58] C. D. Bain, J. Evall, and G. M. Whitesides, "Formation of monolayers by the coadsorption of thiols on gold: Variation in the head group, tail group, and solvent," *Journal of the American Chemical Society*, vol. 111, no. 18, pp. 7155–7164, 1989.

[59] C. D. Bain and G. M. Whitesides, "Formation of monolayers by the coadsorption of thiols on gold: Variation in the length of the alkyl chain," *Journal of the American Chemical Society*, vol. 111, no. 18, pp. 7164–7175, 1989.

[60] L. Bertilsson and B. Liedberg, "Infrared study of thiol monolayer assemblies on gold: Preparation, characterization, and functionalization of mixed monolayers," *Langmuir*, vol. 9, no. 1, pp. 141–149, 1993.

[61] J. P. Folkers, P. E. Laibinis, G. M. Whitesides, and J. Deutch, "Phase behavior of two-component self-assembled monolayers of alkanethiolates on gold," *Journal of Physical Chemistry*, vol. 98, no. 2, pp. 563–571, 1994.

[62] D. Hobara, M. Ota, S. . Imabayashi, K. Niki, and T. Kakiuchi, "Phase separation of binary self-assembled thiol monolayers composed of 1-hexadecanethiol and 3-mercaptopropionic acid on au(111) studied by scanning tunneling microscopy and cyclic voltammetry," *Journal of Electroanalytical Chemistry*, vol. 444, no. 1, pp. 113–119, 1998.

[63] S. J. Stranick, A. N. Parikh, Y. . Tao, D. L. Allara, and P. S. Weiss, "Phase separation of mixed-composition self-assembled monolayers into nanometer scale molecular domains," *Journal of Physical Chemistry*, vol. 98, no. 31, pp. 7636–7646, 1994.

[64] K. Tamada, M. Hara, H. Sasabe, and W. Knoll, "Surface phase behavior of n-alkanethiol self-assembled monolayers adsorbed on au(111): An atomic force microscope study," *Langmuir*, vol. 13, no. 6, pp. 1558–1566, 1997.

[65] W. Mizutani, T. Ishida, S. . Yamamoto, H. Tokumoto, H. Hokari, H. Azehara, and M. Fujihira, "Phase separation of a self-assembledmonolayer made from hydrocarbon-fluorocarbon disulfide," *Applied Physics A: Materials Science and Processing*, vol. 66, no. SUPPL. 1, 1998.

[66] H. Munakata, S. Kuwabata, Y. Ohko, and H. Yoneyama, "Spatial distribution of domains in binary self-assembled monolayers of thiols having different lengths," *Journal of Electroanalytical Chemistry*, vol. 496, no. 1-2, pp. 29 – 36, 2001.

[67] K. Aoki, "Theory of phase separation of binary self-assembled films," *Journal of Electroanalytical Chemistry*, vol. 513, no. 1, pp. 1 – 7, 2001.

[68] C. Miller, P. Cuendet, and M. Grätzel, "Adsorbed ω-hydroxy thiol monolayers on gold electrodes: Evidence for electron tunneling to redox species in solution," *Journal of Physical Chemistry*, vol. 95, no. 2, pp. 877–886, 1991.

[69] H. O. Finklea, S. Avery, M. Lynch, and T. Furtsch, "Blocking oriented monolayers of alkyl mercaptans on gold electrodes," *Langmuir*, vol. 3, no. 3, pp. 409–413, 1987.

[70] C. Amatore, J. M. Savant, and D. Tessier, "Charge transfer at partially blocked surfaces. a model for the case of microscopic active and inactive sites," *Journal of Electroanalytical Chemistry*, vol. 147, no. 1-2, pp. 39–51, 1983.

[71] P. E. Laibinis, M. A. Fox, J. P. Folkers, and G. M. Whitesides, "Comparisons of self-assembled monolayers on silver and gold: Mixed monolayers derived from $HS(CH_2)_{21}X$ and $HS(CH_2)_{10}$ (X,Y=CH_3, CH_2OH) have similar properties," *Langmuir*, vol. 7, no. 12, pp. 3167–3173, 1991.

[72] M. Cavallini, M. Facchini, C. Albonetti, F. Biscarini, M. Innocenti, F. Loglio, E. Salvietti, G. Pezzatini, and M. L. Foresti, "Two-dimensional self-organization of cds ultra thin films by confined elec-

trochemical atomic layer epitaxy growth," *Journal of Physical Chemistry C*, vol. 111, no. 3, pp. 1061–1064, 2007.

[73] E. Salvietti, F. Loglio, M. Innocenti, M. Cavallini, M. Facchini, G. Pezzatini, R. Raiteri, and M. L. Foresti, "Patterned growth of cds by combined electrochemical atomic layer epitaxy and microcontact printing techniques," *Electrochimica Acta*, vol. 52, no. 19, pp. 6034–6040, 2007.

[74] H. Bode, K. Dehmelt, and J. Witte, "Zur kenntnis der nickelhydroxidelektrode-i. ber das nickel (ii)-hydroxidhydrat," *Electrochimica Acta*, vol. 11, no. 8, pp. 1079–1087, 1966. Cited By (since 1996): 253.

[75] J. Mcbreen, "The nickel oxide electrode," in *Modern Aspects of Electrochemistry* (J. O. B. E. Ralph, J. White and B. Conway, eds.), vol. 23, pp. 29–63, New York: Plenum Press, 1990.

[76] R. Barnard, C. F. Randell, and F. L. Tye, "Studies concerning charged nickel hydroxide electrodes i. measurement of reversible potentials," *Journal of Applied Electrochemistry*, vol. 10, no. 1, pp. 109–125, 1980. Cited By (since 1996): 113.

[77] B. Beverskog and I. Puigdomenech, "Revised pourbaix diagrams for nickel at 25-300 c," *Corrosion Science*, vol. 39, no. 5, pp. 969 – 980, 1997.

[78] O. M. Magnussen, J. Scherer, B. M. Ocko, and R. J. Behm, "In situ x-ray scattering study of the passive film on ni(111) in sulfuric acid solution," *Journal of Physical Chemistry B*, vol. 104, no. 6, pp. 1222–1226, 2000.

[79] J. Scherer, B. M. Ocko, and O. M. Magnussen, "Structure, dissolution, and passivation of ni(111) electrodes in sulfuric acid solution: An in situ stm, x-ray scattering, and electrochemical study," *Electrochimica Acta*, vol. 48, no. 9 SPEC., pp. 1169–1191, 2003. Cited By (since 1996): 40.

[80] D. Zuili, V. Maurice, and P. Marcus, "Surface structure of nickel in acid solution studied by in situ scanning tunneling microscopy," *Journal of the Electrochemical Society*, vol. 147, no. 4, pp. 1393–1400, 2000.

[81] S. Medway, C. Lucas, A. Kowal, R. Nichols, and D. Johnson, "In situ studies of the oxidation of nickel electrodes in alkaline solution,"

Journal of Electroanalytical Chemistry, vol. 587, no. 1, pp. 172 – 181, 2006.

[82] A. Dmochowska, Malgorzata; Czerwiski, "Behavior of a nickel electrode in the presence of carbon monoxide," *Journal of Solid State Electrochemistry*, vol. 2, pp. 16–23, 1998.

[83] S. . Yau, F. . F. Fan, T. P. Moffat, and A. J. Bard, "In situ scanning tunneling microscopy of ni(100) in 1 m naoh," *Journal of Physical Chemistry*, vol. 98, no. 21, pp. 5493–5499, 1994.

[84] B. Beden and A. Bewick, "The anodic layer on nickel in alkaline solution: an investigation using in situ ir spectroscopy," *Electrochimica Acta*, vol. 33, no. 11, pp. 1695–1698, 1988.

[85] F. Hahn, B. Beden, M. J. Croissant, and C. Lamy, "In situ uv visible reflectance spectroscopic investigation of the nickel electrode-alkaline solution interface," *Electrochimica Acta*, vol. 31, no. 3, pp. 335–342, 1986.

[86] J. L. Weininger and M. W. Breiter, "Effect of crystal structure on the anodic oxidation of nickel," *Journal of The Electrochemical Society*, vol. 110, no. 6, pp. 484–490, 1963.

[87] C. A. Melendres, W. Paden, B. Tani, and W. Walczak, "On the structure of the higher oxide forms of nickel.," *Journal of the Electrochemical Society*, vol. 134, no. 3, pp. 762–763, 1987. Cited By (since 1996): 11.

[88] Q. S. Song, G. K. Aravindaraj, H. Sultana, and S. L. I. Chan, "Performance improvement of pasted nickel electrodes with multi-wall carbon nanotubes for rechargeable nickel batteries," *Electrochimica Acta*, vol. 53, no. 4, pp. 1890–1896, 2007. Cited By (since 1996): 14.

[89] W. Taucher-Mautner and K. Kordesch, "Studies of pasted nickel electrodes to improve cylindrical nickel-zinc cells," *Journal of Power Sources*, vol. 132, no. 1-2, pp. 275–281, 2004. Cited By (since 1996): 9.

[90] D. Yan and W. Cui, "Preparation and properties of no-binder electrode ni/mh battery," *Journal of Alloys and Compounds*, vol. 293, pp. 780–783, 1999. Cited By (since 1996): 10.

[91] A. Yuan, S. Cheng, J. Zhang, and C. Cao, "Effects of metallic cobalt addition on the performance of pasted nickel electrodes," *Journal of Power Sources*, vol. 77, no. 2, pp. 178–182, 1999. Cited By (since 1996): 37.

[92] F. Bidault, D. Brett, P. Middleton, N. Abson, and N. Brandon, "A new application for nickel foam in alkaline fuel cells," *International Journal of Hydrogen Energy*, vol. 34, no. 16, pp. 6799 – 6808, 2009. 4th Dubrovnik Conference, 4th Dubrovnik Conference.

[93] W. Yang, S. Yang, W. Sun, G. Sun, and Q. Xin, "Nanostructured silver catalyzed nickel foam cathode for an aluminum-hydrogen peroxide fuel cell," *Journal of Power Sources*, vol. 160, no. 2, pp. 1420 – 1424, 2006. Special issue including selected papers presented at the International Workshop on Molten Carbonate Fuel Cells and Related Science and Technology 2005 together with regular papers.

[94] W. Yang, S. Yang, W. Sun, G. Sun, and Q. Xin, "Nanostructured palladium-silver coated nickel foam cathode for magnesium-hydrogen peroxide fuel cells," *Electrochimica Acta*, vol. 52, no. 1, pp. 9 – 14, 2006.

[95] S. M. Kane, D. R. Huntley, and J. L. Gland, "Toluene formation from coadsorbed methanethiol and benzenethiol on nickel surfaces," *The Journal of Physical Chemistry B*, vol. 105, no. 39, pp. 9548–9556, 2001.

[96] S. M. Kane, D. R. Huntley, and J. L. Gland, "Toluene formation from coadsorbed methanethiol and benzenethiol on the ni(111) surface," *Journal of the American Chemical Society*, vol. 118, no. 15, pp. 3781–3782, 1996.

[97] S. M. Kane and J. L. Gland, "Cyclohexanethiol adsorption and reaction on the ni(111) surface," *The Journal of Physical Chemistry B*, vol. 102, no. 27, pp. 5322–5328, 1998.

[98] D. R. Huntley, "The mechanism of the desulfurization of benzenethiol by nickel (110)," *The Journal of Physical Chemistry*, vol. 96, no. 11, pp. 4550–4558, 1992.

[99] Z. Mekhalif, J. Riga, J. Pireaux, and J. Delhalle, "Self-assembled monolayers of n-dodecanethiol on electrochemically modified polycrystalline nickel surfaces," *Langmuir*, vol. 13, no. 8, pp. 2285–2290, 1997.

[100] Z. Mekhalif, F. Laffineur, N. Couturier, and J. Delhalle, "Elaboration of self-assembled monolayers of n-alkanethiols on nickel polycrystalline substrates: Time, concentration, and solvent effects," *Langmuir*, vol. 19, no. 3, pp. 637–645, 2003.

[101] S. Noel, F. Houze, L. Boyer, Z. Mekhalif, J. Delhalle, and R. Caudano, "Self-assembled monolayers of alkanethiols on nickel surfaces for low level electrical contact applications," *IEEE Trans. Compon. Packag. Technol.*, vol. 22, p. 79, 1999.

[102] L. Tortech, Z. Mekhalif, J. Delhalle, F. Guittard, and S. Gribaldi, "Self-assembled monolayers of semifluorinated thiols on electrochemically modified polycrystalline nickel surfaces," *Thin Solid Films*, vol. 491, no. 1-2, pp. 253 – 259, 2005.

[103] L. Y. Y. Lee, G. M. Morales, "Self-assembled monolayers of isocyanides on nickel electrodes," *Thin Solid Films*, vol. 44, no. 27, pp. 4228–4231, 2005.

[104] S. Bengió, M. Fonticelli, G. Benítez, A. H. Creus, P. Carro, H. Ascolani, G. Zampieri, B. Blum, and R. C. Salvarezza, "Electrochemical self-assembly of alkanethiolate molecules on ni(111) and polycrystalline ni surfaces," *The Journal of Physical Chemistry B*, vol. 109, no. 49, pp. 23450–23460, 2005.

[105] K. Izutsu, *Electrochemistry in nonaqueous solutions*. Wiley-VCH, 2002.

[106] P. Marcus and E. Protopopoff, "Potential ph diagrams for sulfur and oxygen adsorbed on nickel in water," *Journal of the Electrochemical Society*, vol. 140, no. 6, pp. 1571–1575, 1993.

[107] I. Paseka, "Sorption of hydrogen and kinetics of hydrogen evolution on amorphous ni-$s_{\boldsymbol{x}}$ electrodes," *Electrochimica Acta*, vol. 38, no. 16, pp. 2449–2454, 1993.

[108] G. P. Power, "The electrochemistry of the nickel sulfides," *Electrochimica Acta*, vol. 27, no. 3, pp. 359–364, 1982.

[109] B. Zhang, X. Ye, W. Dai, W. Hou, and Y. Xie, "Biomolecule-assisted synthesis and electrochemical hydrogen storage of porous spongelike $ni_{\mathbf{3}}s_{\mathbf{2}}$ nonanostructures grown directly on nickel foils," *Chemistry European Journal*, vol. 12, pp. 2337–2342, 2006.

[110] V. Bambagioni, C. Bianchini, J. Filippi, W. Oberhauser, A. Marchionni, F. Vizza, R. Psaro, L. Sordelli, M. L. Foresti, and M. Innocenti, "Ethanol oxidation on electrocatalysts obtained by spontaneous deposition of palladium onto nickel-zinc materials," *ChemSusChem*, vol. 2, pp. 99–112, 2009.

[111] Z. Liang, T. Zhao, J. Xu, and L. Zhu, "Mechanism study of the ethanol oxidation reaction on palladium in alkaline media," *Electrochimica Acta*, vol. 54, no. 8, pp. 2203 – 2208, 2009.

[112] S. Shen, T. Zhao, J. Xu, and Y. Li, "Synthesis of pdni catalysts for the oxidation of ethanol in alkaline direct ethanol fuel cells," *Journal of Power Sources*, vol. 195, no. 4, pp. 1001 – 1006, 2010.

[113] H. Wang, C. Xu, F. Cheng, and S. Jiang, "Pd nanowire arrays as electrocatalysts for ethanol electrooxidation," *Electrochemistry Communications*, vol. 9, no. 5, pp. 1212 – 1216, 2007.

[114] F. Cheng, H. Wang, Z. Sun, M. Ning, Z. Cai, and M. Zhang, "Electrodeposited fabrication of highly ordered pd nanowire arrays for alcohol electrooxidation," *Electrochemistry Communications*, vol. 10, no. 5, pp. 798 – 801, 2008.

[115] Y. Y. S. Uhm and J. Lee, "Electrocatalytic activity of pdceo$_2$ nanobundle in an alkaline ethanol oxidation," *Catalysis Letters*, vol. 138, no. 1-2, pp. 46–49, 2010.

[116] H. Birnbaum, *Encyclopedia of Material Science and Engineering*, ch. Hydrogen Embrittlement. New York: Pergamon, 2000.

[117] J. Abys and C. Dullaghan, *Modern Electroplating*, ch. Electrodeposition of Palladium and Palladium Alloys. New York: Wiley, 1986.

[118] M. Grden, M. Lukaszewski, G. Jerkiewicz, and A. Czerwinski, "Electrochemical behaviour of palladium electrode: Oxidation, electrodissolution and ionic adsorption," *Electrochimica Acta*, vol. 53, no. 26, pp. 7583–7598, 2008.

[119] T. Kakiuchi, H. Usui, D. Hobara, and M. Yamamoto, "Voltammetric properties of the reductive desorption of alkanethiol self-assembled monolayers from a metal surface," *Langmuir*, vol. 18, no. 13, pp. 5231–5238, 2002.

[120] O. Azzaroni, M. E. Vela, G. Andreasen, P. Carro, and R. C. Salvarezza, "Electrodesorption potentials of self-assembled alkanethiolate monolayers on ag(111) and au(111). an electrochemical, scanning tunneling microscopy and density functional theory study," *The Journal of Physical Chemistry B*, vol. 106, no. 47, pp. 12267–12273, 2002.

[121] M. Schneeweiss, H. Hagenstrom, M. Esplandiu, and D. Kolb, "Electrolytic metal deposition onto chemically modified electrodes," *Applied Physics A: Materials Science & Processing*, vol. 67, pp. 537–551, 1999.

[122] "Software reflectivity tool parrat 32, hmi, berlin,," 1999.

[123] L.G.Parratt, "Surface studies of solids by total reflection of x-rays," *Phys. Rev.*, vol. 95, pp. 359–369, 1954.

[124] P. L.Nevot, "Caractérisation des surfaces par réflexion rasante de rayons x. application à l'´etude du polissage de quelques verres silicates," *Revue Phys.Appl.*, vol. 15, p. 761, 19808.